Spaceborne Doppler Radars in Convection: Performance of EarthCARE and Beyond

Thesis submitted for the degree of

Doctor of Philosophy

at the University of Leicester

by

Tomasz Augustynek MSc

Department of Physics and Astronomy

University of Leicester

October, 2013

Abstract

The thesis concerns the assessment of the performance of the upcoming Earth Cloud Aerosols Radiation Explorer (EarthCARE) Doppler cloud profiling radar in convection. Spaceborne Doppler radar data are simulated starting from high-resolution CRM model data, through forward Monte Carlo simulation from which the voltage signals as sampled by specific radar configuration are generated. Until the launch of EarthCARE in 2016, simulations are the only means of assessing the impact of EarthCAREs configuration on the accuracy of the Doppler products (reflectivity and mean Doppler velocity).

Two of the main contributors to EC-CPR total error budget are the multiple scattering and non-uniform beam filling effect errors, which can be mitigated using methods described in the thesis. However, for EarthCARE radar using the conventional pulse pair technique, the scientific requirement for accuracy of 1 m/s at 1 km integration of Doppler velocity can not be met for deep convective systems, even if the correction methods are applied.

The thesis then focuses on six polarization diversity radar systems, three for W-band (94 GHz) and three for Ka-band (35 GHz). After the correction methods are applied for MS and NUBF effects, the accuracy of 1 m/s for 500 m integration is possible for all W-band configurations assessed. This includes relatively small antennas of 2.5 m currently being implemented in space.

Consequently, two key results for measurements in deep convection can be drawn for future radar concept design. Firstly, the large antenna will help to minimize the effects of non-uniform beam filling and multiple scattering. Secondly, the polarization diversity can solve the problem of aliasing of velocities.

I would like to dedicate this thesis to my parents.

Acknowledgements

I would like to express my deep appreciation to my supervisor Dr Alessandro Battaglia for his invaluable contribution, tens of hours of discussions and for always being there for help and his guidance and patience. I would also like to thank Prof. John Remedios for his support, supervision and encouragement. Also Dr Hartmut Boesch for inspiration to undertake a PhD and help when needed.

And I would like to acknowledge Gerry Heymsfield from NASA/GSFC who kindly provided airborne radar data from NASA ER-2 aircraft from CRYSTAL-FACE campaign. Pavlos Kollias from McGill University and Simone Tanelli from NASA/JPL for valuable input into instrument model. I am also grateful for a research studentship from the University of Leicester, UK.

Special thanks go to my Parents and family - without their enormous continuous support the task would be impossible to succeed.

I would like to say thank you for my housemates: Alessio for many voyages and Limey for endless discussions, both for being great guys to live with. For friends which made my stay in Leicester comfortable: Daniel, Anna, Michal, James, Alex, Ed, Tim, all Earth Observation Science people. For all my friends back at home who always made me feel welcome - especially: Mateo, Agata, Krzysiek, Magda, Bartek, Gaga and last but not least Dana.

Declaration

I hereby declare that no part of this thesis has been previously submitted to this or any other University as part of the requirement for a higher degree. The work described herein was conducted by the undersigned except for contribution from colleagues as acknowledged in the text.

Tomasz Augustynek
October, 2013

Contents

List of Figures

LIST OF ABBREVIATIONS

ACE	Aerosol-Cloud-Ecosystem
CAPE	Convective Available Potential Energy
CDF	Cumulative Distribution Function
CFAD	Cumulative Frequency Altitude Display
CLDY	Climate Dynamics Mission
CPR	Cloud Profiling Radar
CRS	Cloud Radar System Airborne Doppler Radar
EC	EarthCARE
EDOP	Airborne Doppler Radar onboard ER-2
ESA	European Space Agency
ETS	Equitable Threat Score
GCMs	General Circulation Models
GPM	Global Precipitation Measurement
IDFT	Inverse Discrete Fourier Transform
IFOV	Instantaneous Field of View
INF	Infinite PRF (High PRF) Spectrum
ISS	International Space Station
KF	Kain-Fritsch Convective parameterization scheme
LDR	Linear Depolarization Ratio
LEO	Low Earth Orbit
MC	Monte Carlo scheme
MDS	Minimum Detectable Signal
MS	Multiple Scattering
NUBF	Non-Uniform Beam Filling
NWP	Numerical Weather Prediction
PDF	Probability Distribution Function
PDPP	Polarization Diversity Pulse-Pair
PP	Pulse-Pair

PR	Precipitation Radar
PRF	Pulse Repetition Frequency
RH	Relative Humidity
SNR	Signal-to-Noise Ratio
SP	Signal Processing
SS	Single Scattering
TOA	Top of Atmosphere
TRMM	Tropical Rainfall Measuring Mission
WRF	Weather Research and Forecasting model

Chapter 1

Introduction

Convective vertical air motion is a key atmospheric parameter that affects cloud microphysics, radiation and lifetime of convection (Phillips and Donner [2006]). Despite its importance no measurements of vertical air motion are available globally, especially over the tropical oceans. Spaceborne Doppler radars have the potential to provide key missing global distribution of the vertical motions in clouds and precipitation (Battaglia et al. [2013]). Spaceborne millimeter-wave radars are able to penetrate optically thick cloud layers of high water content, while the attenuation occurs low in the atmosphere where most of the liquid precipitation and vapour resides, causing the spaceborne radars to be less affected than the same frequency ground-based ones (Stephens and Wood [2007]). One important limitation when elucidating the complex interactions between storm dynamics, thermodynamics, and microphysics of deep convection is the practical hazard associated with obtaining

direct measurements from within intense convective environments. Given known aircraft restrictions for flying directly into deep convective clouds, there is a need to advance remote sensing solutions that encourage longer-term cumulative convective characterization (Giangrande et al. [2013]). This makes spaceborne Doppler radars ideal candidates for studying convective clouds. It is envisaged that radar measurements will provide a better understanding of precipitation processes and dynamics on a global scale (e.g. by measuring vertical profiles of latent heat fluxes) and improve the characterization of convection (vertical profiling and temporal evolution) and as well as improve General Circulation Models (GCMs) skills by assimilating vertical velocity. As a result, this can improve our understanding of the role of tropical convection in vertical energy transport and its interaction with the environment.

Several millimeter wavelength Doppler spaceborne radar concepts have been proposed, while ground-based Doppler radars are operational since the 1990s. The first spaceborne precipitation 13.8 GHz radar (PR) on the Tropical Rainfall Measuring Mission (TRMM) satellite was launched in November of 2007. It has played a very significant role in the characterization of clouds and precipitation particles aloft and has provided valuable information on the structure of storms as well as rainfall structure (Kummerow et al. [1998]). The CloudSat 94 GHz radar, which was launched in 2006, has been investigating the vertical structure of clouds since then (Stephens et al. [2002]). The TRMM follow-up mission - Global Precipitation Measurement (GPM) was launched in 2014. In 2007 NASA Earth Science Decadal Survey Studies

recommended ACE mission with dual frequency Doppler cloud radar onboard for launch within the next decade (ACE-Science-Group [2010]). This shows the international effort and interest in spaceborne radar systems as a key instrument for scientific research. The EarthCARE Cloud Profiling Radar (CPR), which is due to be launched in 2016, will be the first cloud radar in space with Doppler capability enabling measurements of vertical velocity of hydrometeors. In fact, future spaceborne radars are envisaged to operate with the Doppler capability that provides a new dimension in measurements from space offering an invaluable opportunity to measure hydrometeor motions.

1.1 Scope of the Project

The primary objective of the thesis is the assessment of the accuracy of the upcoming EarthCARE spaceborne radar mission for measurements in deep convection. The accuracy of the velocity products has been examined by employing an end-to-end radar simulator. Until the launch of EarthCARE in 2016, simulations are the only means of assessing the impact of EarthCARE's configuration on the accuracy of the Doppler products (reflectivity and mean Doppler velocity) and to estimate the total error budget. The investigation of the relative effect of the different error sources for typical convective scenarios is presented, by identifying the most relevant ones and by evaluating the impact of different correction techniques onto the error reduction. The radar simulation framework is exploited to disentangle the effect of each of these

errors, first important step towards quality-controlled Doppler products.

As the achievement of scientifically required high accuracy in convection by the EarthCARE-CPR will be challenging, the envisaged and hypothetical future space-borne radar concepts with larger antennas and different signal processing techniques are evaluated. The analysis of the main drivers of error budget for such concepts in then presented.

1.2 Significance of Clouds and Convection

Clouds are a key element in the global hydrological cycle, and they have a significant role in the earth's energy budget through its influence on radiation budgets. Climate model simulations have demonstrated the importance of clouds in moderating and forcing the global energy budget (Houghton et al. [1995], Stephens et al. [1990]). Correct representation of cumulus convection in global models and accounting for the interactions that are involved with convection has been a long-standing difficulty to the modeling community (Arakawa [2004]).

The Intergovernmental Panel on Climate Change (IPCC) warns that the climate variability over different spatial and temporal scales are of enormous social and economic value. The Third Assessment Report (IPCC, 2001) concludes that "there are particular uncertainties associated with clouds and their interactions with radiation and aerosols" and that "there has been no apparent narrowing of uncertainty associated with cloud feedbacks in current climate models". The situation improved

in many areas of climate change studies since then, however the IPCC [2013] states that cloud feedbacks continue to be the largest uncertainty in climate sensitivity studies. The representation of deep cumulus convection is recognised as one of the key issues. Large part of uncertainty in climate models arises from shortcomings in the treatment of cloud and aerosol processes and the lack of observations to validate cloud and aerosol parameterisation schemes. Cloud parameterisations (see Sect. 1.2.2) as well as indirect aerosol effects on cloud radiative forcing are today the largest sources of uncertainty in climate prediction. That is, the critical cloud radiation feedback cannot be modelled without accurate cloud and aerosol parameterisations. There are still very few observations to evaluate if representation of typically used variables in climate and forecasting models (like cloud cover, ice and liquid water content, cloud overlap) is correct.

Clouds (along with aerosols) are responsible for most of the uncertainty of changes of geographical distribution of precipitation as well as for projections for future climate change and global warming. The response of climate models is very sensitive to correct cloud description. However, an appropriate representation in General Circulation Models (GCMs) utilized for weather and climate predictions is hard to implement because clouds enclose a broad spectrum of scales, from microphysical processes to planetary scales describing cloud occurrence in large systems (frontal bands, convergence zone). The largest uncertainty in intermodel differences of the transient temperature change is associated with clouds as shown in Fig. 1.1.

However, there are very few vertically resolved cloud data to validate current models. This is where the EarthCARE radar is believed to provide significant impact as one of the goals of the EarthCARE satellite is to provide such data and validate the representation of clouds and aerosols in current climate models.

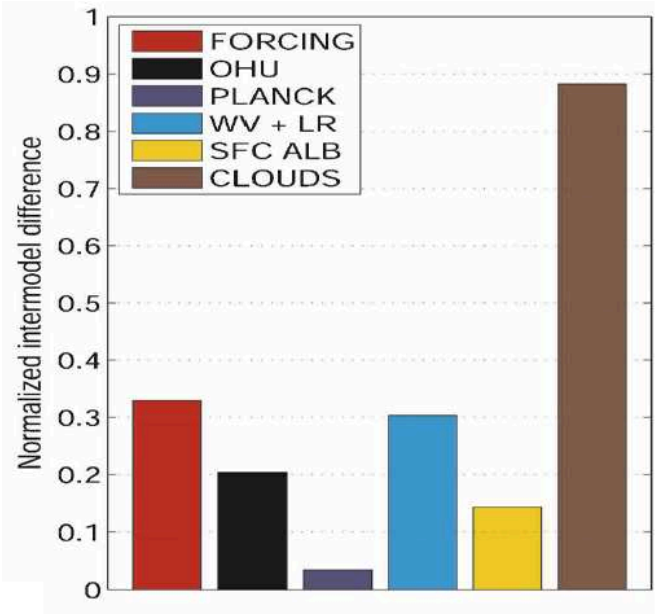

Figure 1.1: Normalized intermodel standard deviation of the transient temperature change estimates associated with intermodel differences in radiative forcing, Planck response, ocean heat uptake and the various feedbacks, with the clouds contribution marked in brown (Dufresne and Bony [2008]).

1.2.1 Convection

Convection is thermally driven turbulent mixing of the atmosphere and is a critical element in the Earth's climate. Deeper, more vigorous convection is often observed in cold air masses flowing over a warmer surface. Under certain conditions, buoyant plumes originating near the earth′s surface can break through the weak temperature

inversion that usually caps the mixed layer, giving rise to towering clouds that extend all the way to the tropopause, referred to as deep convection. Cloud formation associated with convection plays an important role in the radiation budget (Zhang [1993]). In general, convection produces characteristic types of clouds as well as distributes heat and moisture in the vertical and produces rainfall. However this phenomenon is very difficult to parameterise in weather prediction models as well its impact on climate change is not fully understood. This is mainly because convection is widely varying in shape, size and duration. Convection can be isolated, organized into groups of cells, weak or intense and deep or shallow. Convection is also responsible for rainfall and snowfall, clouds and changes in vertical stability. It has also its negative face producing devastating floods, ice storms and blizzards or damaging winds, hail, lightning, tornadoes and hurricanes. During the lifetime of convective cells the vertical velocity and precipitation are not always in phase. Updraughts tend to be the strongest during early to mature periods of cell development while precipitation and radar reflectivities are the strongest during the mature and dissipating stages. Zipser et al. [2006] concluded that intense convection often peaks in the afternoon over land with no peak activity over ocean. Correctly predicting convection is often the most difficult forecast aspect (Stensrud [2012]).

Deep convection plays a key role in the exchange between the upper troposphere and the lower stratosphere with important consequences for the energy and heat budget (Kuang and Bretherton [2004]; Tian and Ramanathan [2002]) and mois-

ture distribution (e.g., Sohn and Schmetz [2004]). However, the deep convective updraught properties in the higher-altitude regions have not been measured extensively and the documentation in literature is sparse. Heymsfield et al. [2010] collected several airborne datasets from different locations, including convection in summer and winter and provided thorough analysis on measured radar reflectivities and velocities. They also divided deep convection into further four classes: land, oceanic, sea-breeze and tropical cyclone. The findings include that land based convective cores are wider than the oceanic and tropical cyclone categories (approx 4-5 km versus 1.8 km). The land and sea-breeze cases have slightly higher peak vertical velocities. Strong updraughts often exceed 15 m/s and were higher than previously recorded in literature. This was mostly due to the fact that previous airborne campaigns were flown on lower altitudes, while Heymsfield et al. [2010] concluded that updraught maxima are often above 10-km or even 12-km altitude, near the top of the observations. Some of their cases are the strongest ever recorded, such as updraughts exceeding 30 m/s, downdraught of 19 m/s and cloud tops approaching 17-km altitude. The study tried to relate the convection intensity (maximum updraught strength) with the height of reflectivity contours (levels of 30, 40 dBZ reflectivity) with the correlation coefficient of 0.5 (0.6) showing some correlation. However, the case studies were collected in different life cycle stages and environmental conditions. The strongest updraught often occurs during early development of convection and the highest reflectivities and the strongest downdraught are often

recorded during mature to dissipation stages.

The majority of the Earth's rainfall results from convection, especially for the heavier precipitation, which results in flash floods and loss of life (ESA Mission Experts Division [2004]). Yet convective precipitation is extraordinarily hard to represent within numerical models because it occurs on a scale which is much smaller than the model grid box, and is essentially a statistical and noisy phenomenon.

From the climatological perspective important precipitating systems to measure are those covering large areas such as frontal systems, cyclones and tropical squall lines. In these systems deep convection plays an important role with respect to the total amount of rain produced and to the vertical fluxes of momentum and energy transported. However, the proportion of area covered by the deep convection is typically not larger than 10 - 20 % with the rest corresponding to stratiform precipitation (Amayenc et al. [1993]). In this case, the Doppler radar can help to distinguish those two types of systems, which already brings important information to climatological models.

An example use of CloudSat spaceborne radar is the view of developing thunderstorm as shown in Fig. 1.2. The top panel shows an overpass of CloudSat (blue line) over cloud systems mapped by a MODIS visible image. The CloudSat vertical slice through part of the storm separates the bubbly cloud tops from those with strong updraughts and heavy precipitation. Three systems have been classified as deep convection by the CloudSat cloud classification product during the overpass. As can

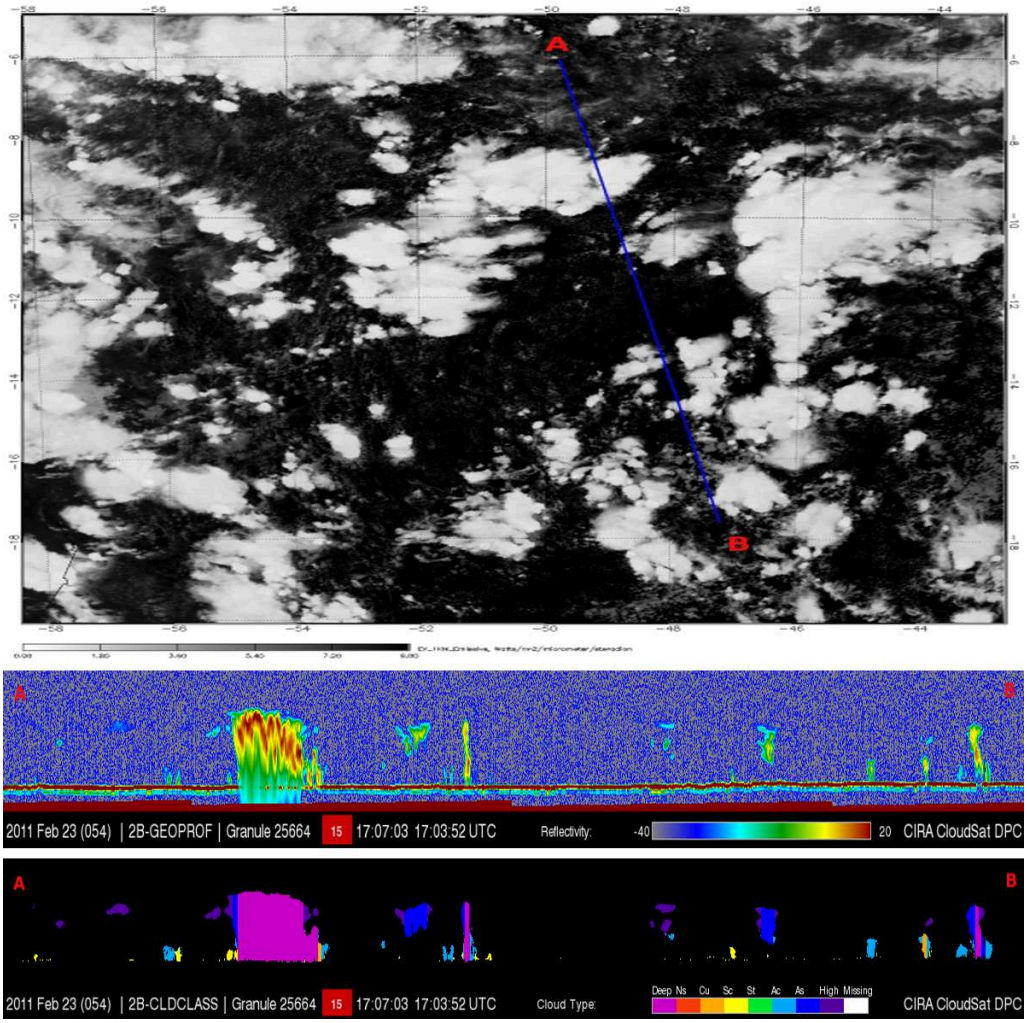

Figure 1.2: Top: an overpass by the CloudSat spaceborne radar on 23/03/2011 (granule 25664) over convective systems, superimposed on MODIS IR imagery. Center panel: image of CloudSat radar reflectivity including deep convective systems. Bottom: cloud classification for the radar overpass (i.e. deep convection marked in pink colour).

be seen the CloudSat signal is fairly attenuated due the heavy rainfall formation in this particular cell.

1.2.2 Parameterisation in Climate and Forecasting Models

The microphysical processes that form, evolve and dissipate clouds or are responsible for convection occur on scales much smaller than the size of a typical model grid box. Although convection can transport material through the whole troposphere, convective clouds have a small horizontal length scale. In order to represent clouds or convection in large-scale models of the atmosphere, on which the convection is below the resolution used, parameterisation is needed. This is partly due to limitation by processing power of current computers. In order to include all the necessary processes and run the current general circulation models (GCM) or numerical weather prediction models (NWP) in a reasonable time their resolution is limited and the effects of clouds must be parameterised. However, to develop accurate parameterisation schemes an accurate knowledge of the physical processes behind clouds and convective motions is needed. The complexity of model parameterisation is always increasing with time. However, the new parameterisation should lead to improved accuracy and increased confidence that the behaviour of predicted processes is closer to observed properties and eventually reducing the uncertainty in a future predictions of the global climate.

Since the 1990s most models use a prognostic cloud water content (often separated into different phases i.e. liquid, ice, and mixed phase). In addition it is common to include cloud ice content and cloud fraction. Smith [1990] gives an

equation for the rate of change of liquid cloud water mixing ratio (q_l) as follows:

$$\frac{dq_l}{dt} = \left(\frac{dq_l}{dt}\right)_{ADV} + \left(\frac{dq_l}{dt}\right)_{DIFF} + \left(\frac{dq_l}{dt}\right)_{TM} + \left(\frac{dq_l}{dt}\right)_{ST} + \left(\frac{dq_l}{dt}\right)_{P} + \left(\frac{dq_l}{dt}\right)_{CV} \quad (1.1)$$

which depends of various source and sink terms: ADV refers to advection; $DIFF$ to horizontal diffusion; TM refers to vertical turbulent mixing from the boundary layer; ST refers to stratiform cloud formation (thanks to condensation) or dissipation (due to evaporation); P refers to the loss by formation of precipitation and finally CV refers to the source of cloud water by detrainment from cumulus convection. In this simplest case there is no distinction between liquid water mixing ratio and cloud ice mixing ratio (q_i); in other words (q_l) incorporates both phases.

As the different cloud phases produce different radiative effects the separation of cloud water content into phases was later introduced (i.e. for Met Office United Model - (Wilson and Ballard [1999])) to allow different phases of vapour (q), ice water content (q_i) and liquid water cloud (q_l). However, due to time constrains of model run, in Wilson and Ballard [1999] implementation all ice was classified in one variable, there was no distinction between hail, graupel, snow or ice. At present most climate models and operational forecast models use also cloud fraction, often diagnosed from relative humidity (RH) with defined critical relative humidity (RH_{crit}) at which cloud begins to form. In addition, most models make assumptions about how clouds are overlapped between vertical grid boxes. Three most common overlap assumptions are maximum overlap, random overlap and maximum-random

overlap (Geleyn and Hollingsworth [1979]; Morcrette and Fourquart [1986]).

The parameterisation schemes in NWP or GCMs are defined in terms of properties, such as the ice water content within a model grid box. However, the radar instruments do not measure this quantity directly. As the typical radar has narrow beamwidth when compared to the model grid size - a spaceborne or vertically pointing radar is not capable of providing such information over entire model grid box. They measure the backscattered intensity of the electromagnetic radiation returned from targets, which has to be converted to for example ice water content using either theoretical particle size distributions (Sassen [1987]) or aircraft-measured (Liu and Illingworth [2000]) to derive this quantity.

Special place is taken by the convective parameterization schemes, sometimes called cumulus or moist convective parameterization. Arakawa [2004] provided a thorough review article on the subject, pinpointing past, present and possible future ideas on how to parameterize cumulus convection. However, quite common approach is to use Kain-Fritsch (KF) convective parameterization and modifications of it (Kain [2004]; Kain and Fritsch [1990]). The source codes of the KF scheme have been originally developed for the Weather Research and Forecast (WRF) modelling. The KF scheme assumes that the convection consumes the convective available potential energy (CAPE, a useful measure of the maximum possible intensity of convection) in a certain time scale. This is usually within 1800 to 3600 seconds. To identify source layers for convective clouds, the KF scheme utilizes a trigger function based

on the temperature at the lifting condensation level (LCL) and the grid-scale vertical velocity (Kain [2004]).

Previously, convection in climate models was treated based on deterministic mass flux which caused processes like diurnal cycle of convection to be badly represented. The new schemes favor statistical approach, where the convection process is treated as a probability distribution function (PDF). Convection is indeed a statistical phenomenon and these PDF approaches capture this aspect. However, different schemes lead to different PDFs of mass flux and vertical velocities, both in magnitude, cross-sectional area and vertical profiles, as well as sensitivity to initialization schemes. Global observations are needed to evaluate these schemes and quantify the amount of moisture introduced into the stratosphere by these processes (ESA Mission Experts Division [2004]).

Currently, the development of improved parameterisation of convection is still the topic of ongoing scientific discussion, which allows for several approaches in the parameterisation schemes. The UK NAME model uses mass-flux approach to characterize vertical transport of particles due to convection (Meneguz and Thomson [2013]). Meteorological data are provided to NAME by the Met Office's operational NWP model, the Unified Model (UM). The UM is run for global prediction with horizontal size of 25 km so the convection must be parameterised as it is a subscale to the model resolution. The UM quantifies, for each grid box, the amount of mass transported in updraughts and downdraughts, in entrainment of environmental air

and in detrainment of cloudy air. Current convection scheme of NAME model uses the UM diagnostics: height of cloud top, height of cloud base and cloud fraction. The recently proposed convective transport scheme is more physically based making use of the balance equation of fluxes. In particular, upward mass fluxes are calculated with empirical formulas derived from CRM and using the NWP convective precipitation diagnostic as closure (Gregory and Rowntree [1990]). In the recent version the vertical column is divided into a number of non-equally spaced vertical pressure levels (i.e. up to 30km). Once the particles are in the cloud they can either move upward, entrain or detrain into the environment - the type of motion is governed in a probabilistic way via a set of probabilities.

Narita and Ohmori [2007] from the Japan Meteorological Agency used for their mesoscale model simultaneous KF parameterization scheme with a bulk parameterization scheme of cloud microphysics. In their cloud microphysics scheme, water substance is expressed by its mixing ratio and categorized into six forms: water vapor, cloud water, rain, cloud ice, snow and graupel. The pre-operational forecast tests with only cloud microphysics showed some weaknesses. In spite of this, the Kain-Fritsch scheme was adopted to represent the effects of subgrid-scale convection. The incorporation of the KF scheme improved the forecast scores in their model. Recent study by Lange et al. [2014] for regional climate model sensitivities over South America found out that the modeled climate is found to be highly sensitive to the parametrizations, particularly in tropical latitudes. They compared the per-

formance of the model with four different setups, which differ in the parametrizations of convection and subgrid-scale clouds. They concluded that the parameterization of convection is one of the two major contributors to model performance, the other being the sensitivity of modeled precipitation to the parametrization of subgridscale clouds.

1.2.3 Tropical Convective Clouds Overshooting Tropopause

One of the most important unanswered questions is the water vapour transport process from the troposphere to the stratosphere, especially because the analysis of recent decadal records shows that water vapour in the stratosphere is increasing. As water vapour is a greenhouse gas, and long-lived stratospheric water vapour can affect the global energy budget and it has been shown that increasing water vapour in the stratosphere cools the stratosphere but heats the troposphere (Forster and Shine [1999], Smith et al. [2001]). However, the role played by deep cloud intrusions through the tropopause still presents a major difficulty as convective clouds can cause both hydration (Corti et al. [2008]) and dehydration (Sherwood and Dessler [2001]) of the stratosphere. The effect depends on the characteristic size of ice particles which determine the sedimentation rates. Chae et al. [2011] stated that clouds hydrate the environment below 16 km, where the air after mixing between cloud and the environmental air does not reach saturation. On the other hand clouds dehydrate the environment above 16 km, due to the supersaturation because

of the larger temperature drop and the high initial relative humidity. The deep convection is one of the two main hypotheses on the manner in which water vapour is transported from the troposphere to the stratosphere and it can be explained due to the effects of deep overshooting convection (Sherwood and Dessler [2001]), therefore more global observations are need.

1.3 Research Community User Requirements for Radar Mission

The nadir-looking radar mission can contribute to various types of research, bonding interest of several research groups, mainly cloud modelling community as well as NWP, data assimilation community and hurricane research community. Each of those communities has separate needs, with the most important summarized below for nadir-pointing radar.

Sensitivity The data already collected by spaceborne radars (e.g., CloudSat) and ground-based networks (e.g., ARM and CloudNet) suggest that a minimum reflectivity of -35 dBZ is required for adequate detection of cloud systems (EarthCARE Mission Advisory Group [2006]).

Doppler accuracy The aim of EarthCARE CPR is to have Doppler velocity accuracy of 1 ms^{-1} for 1 km along-track integration which is stated as sufficient by EarthCARE Science Team (EarthCARE Mission Advisory Group [2006]). However,

for quantitative hydrometeor retrievals (mass, size) and ice sedimentation rates, a Doppler velocity accuracy of 0.2 ms^{-1} is required (Joe et al. [2010]).

Sampling Requirements Diurnal sampling is preferred as mesoscale convective systems and other convective storms are diurnally forced, with the major errors in precipitation forecasts from global models associated with the diurnal cycle and the timing of the peak precipitation intensity (Battaglia et al. [2012]; Nesbitt S. and Zipser [2003])

Resolution Vertical resolution of 250 m or better is required to resolve the internal structure of clouds, convective systems and precipitation and for detecting shallow clouds and precipitation (Tanelli et al. [2010]). Those requirements need to be considered for the EC-mission as well as future radar systems.

1.4 Significance of Doppler Velocity Measurements

Amayenc et al. [1993] stated that determination of the mean wind velocity at a scale comparable with the grid resolution of large scale circulation models would be of great interest for climatology and global meteorology. Vertical velocity within deep convective cores is a quantity of known interest as a constraint to the connections between humidity, entrainment, and microphysical treatments of storm-resolving models (Giangrande et al. [2013]).

Global observations of mass flux and vertical velocity profiles, which can be derived from the observations of spaceborne radars, are needed to evaluate proposed

schemes for parameterising convective mass flux in cloud resolving models, precipitation and clouds. Apart from the occasional case studies, there are currently no direct observations of velocities and fluxes.

Moreover, the accurate representation of particles sedimentation rates is another critical parameter, which the Doppler measurements may help with. In particular, ice sedimentation rates have been shown to be the second most influential GCMs parameter in climate sensitivity experiments.

The inclusion of Doppler velocity will allow measurement of particle motions in clouds, provide better classification of cloud type, direct measure of vertical mass transport and of convective intensity, the estimation of particle size, air motion, and of latent heat release with higher accuracy than non-Doppler estimates.

Doppler measurements from space can help to characterise convective processes classification on global scale. Vertical velocity is the most suitable variable for characterizing the intensity of precipitation and for classifying precipitating clouds to convective and/or large-scale (stratiform) precipitation. Simultaneous measurements of the vertical motion and hydrometeor properties are key for quantifying the important cloud and precipitation processes and the effects of these processes on clouds and storm systems.

It has been shown (Delanoë et al. [2007]) that combining fall speed velocity with radar reflectivity improves quantitative estimates of hydrometeors properties such as mass and size - than the standard characterization with reflectivity alone. This

is crucial for non-spherical particles such as snow.

Doppler measurements will give insight on the mesoscale organization and dynamics in convective and large-scale cloud systems. Doppler radar observations have the potential to characterise the scales and organization of the observed cloud systems, in particular convective systems, and thus assist in their qualitative classification. This can improve: i) the retrieval of microphysical and dynamical properties at nadir and ii) Doppler measurements of the horizontal wind component with resolution 10 km or less can be used to infer the dynamical organization at the mesoscale (50-150 km) (Battaglia et al. [2012]).

The significance of Doppler measurements is confirmed by the fact that the future proposed radar mission concepts have a Doppler capability as a key requirement, especially for the profiling (nadir) systems.

1.5 Challenges Associated with Spaceborne Doppler Radars

Imminent launch of the first spaceborne Doppler radar caused detailed research which identified several obstacles to measuring Doppler velocities from space platforms. The first obvious challenge arises from high relative speed of a spaceborne satellite on Low Earth Orbit (LEO) ($V_{sat} \sim 7.7\ kms^{-1}$) which introduces significant broadening of the Doppler spectrum, even if the radar is pointing perfectly

perpendicular to its motion (Amayenc et al. [1993]). Due to cloud inhomogeneity in radar footprint large velocity biases are likely to happen (Non-Uniform Beam Filling - NUBF: Schutgens [2008]; Tanelli et al. [2002a] and references therein). In optically thick media the presence of Multiple Scattering (MS) can overwhelm the Single Scattering (SS) contribution to the signal, making its interpretation extremely complex (Battaglia et al. [2011]). On top of that velocity folding induced by a low Nyquist velocity in connection with large vertical velocities and extreme wind shear (Heymsfield et al. [2010]; Sy et al. [2013]) pose major problems for EC-type radar systems, which is particularly detrimental in convective areas. Additional sources of uncertainty are associated with the specific signal processing (Kobayashi et al. [2002]; Pazmany et al. [1999]), mis-pointing uncertainty of the satellite (Tanelli et al. [2005]) and averaging error due to long along-track integration in convective systems.

These effects pose a significant challenge for EarthCARE (EC) Cloud Profiling Radar (CPR) performance. Their impact on EarthCARE-like radar and possible methods to mitigate the above mentioned errors are discussed in the thesis.

1.6 Thesis Overview

Following this introduction the thesis is divided into seven chapters: Chapter 2 gives a brief introduction to the radar theory with focus on EarthCARE Cloud Profiling Radar attributes (Pulse Repetition Frequency - PRF, coherency time, etc.). Chapter 3 provides an overview of the EarthCARE mission, instruments onboard and

characteristics. It also briefly introduces other Doppler radar concepts mentioned or assessed in the thesis. In chapter 4 the airborne radar data are utilized to extract information of Doppler velocities and reflectivity occurring naturally in convection. This information is then used to compare with simulated data as well to estimate magnitude of reflectivity gradients which affect Doppler accuracy. Chapter 5 addresses end-to-end radar simulator used in the following chapters and describes its three main modules: forward Monte Carlo modelling, instrument model and corrections module. Drawing on chapter 5 chapter 6 provides complete assessment of the expected EarthCARE-CPR performance in deep convection. An objective methodology for the identification of multiple-scattering-contaminated range bins based purely on reflectivity profile-derived variables is proposed with operational Non Uniform Beam Filling (NUBF) correction coefficients. In chapter 7 the Polarization Diversity Pulse Pair (PDPP) method is discussed that enables a new approach in spaceborne radar systems and better accuracy of velocity measurements while overcoming the main source of uncertainty in EarthCARE-CPR.

Chapter 2

Millimeter Doppler Radars

2.1 Background

A radar sensor, is a system that is capable of transmitting an electromagnetic signal in a form of waveform of known shape and measuring the power backscattered by targets (clouds, hydrometeors, birds, aircraft) and various obstacles (mountain ranges - ground clutter) (Chevalier [2002]) as a function of distance from the radar. Radar is an acronym of "radio detection and ranging". Nowadays radars have become an indispensable part of modern life. Radar systems are used by civilians and military, can be found in aircraft, ships, on motorways, sport fields, weather stations and constitute a major research tool for numerous scientific applications (Rinehart [2004]).

Over the years a lot of effort has been directed towards exploring the scientific

potential of radars in remote sensing of clouds and precipitation. Initially ground-based radars were implemented especially for measuring rain, vertical winds, for investigating cloud structures, forecasting or a severe weather warning indication. From these measurements rain rates can be retrieved from radar reflectivities, which agree well with gauge measurements at ranges close to radar. As the rainfall rate and radar reflectivity are correlated using an empirical coefficient there are hundreds published relations for different rainfall types or regions, with most notable Marshall-Palmer (1948) relation (Alfieri et al. [2010]; Fournier [1999]). However, the increased underestimation can occur at longer ranges from radar. Joss and Lee [1995] examined an extreme case of such underestimation, for radar in Switzerland, where at radar range of 100 km only 35 percent of the actual rain gauge amount is measured due to beam blockage combined with the decrease of reflectivity with height of the sampling volume. Even in less mountainous countries the shortcomings of using radars in hydrology or precipitation measurements stem from the inability to measure precipitation close enough to the ground. This can be avoided using spaceborne nadir pointing radars. One of the main advantages of spaceborne radars is the capability of measuring weather readings (i.e. dynamics of precipitating systems, large scale motion fields) over inaccessible areas such as seas, oceans or forests.

Millimeter-wavelength cloud radars complement the centimeter-wavelength precipitation radars with the ability to detect non-precipitating clouds and smaller hydrometeors. Clouds with hydrometeors composed of diameters from several to

tens of micrometers have very small reflectivity values and present a challenge for cm-wavelength radars which would require the use of high-power transmitters and large antennas to achieve satisfactory sensitivity. Because of the short wavelength cloud radars have better sensitivity to small droplets and ice crystals and their compact size makes their use feasible on platforms such as aircraft, ships or satellite platforms. Kollias et al. [2007] described the history of the millimeter-wavelength radar system development for atmospheric research, from which most notable was implementation of the dual polarization capability, Doppler measurements and dual frequency - first as ground based then track-mounted and airborne systems. This led to the development of the Atmospheric Radiation Measurement (ARM) (Moran et al. [1998]) program with ground radars continuously operating in climatologically distinct locations. Deployment of millimeter-wavelength radars such as CloudSat in space (Stephens et al. [2002]) marked the second stage of applications of radars in atmospheric research.

The choice of the wavelength suitable for radar observations of the atmosphere is limited by atmospheric gas attenuation to the spectral regions in which the absorption of the radar signal by atmospheric gases has a minimum. This restricts the use of a cloud radar around the frequencies of 35, 94, 140 GHz (Lhermitte [1990]). Atmospheric transmissivity versus wavelength for different water vapour amounts is displayed in Fig. 2.1. The loss of transmissivity for the 0 g m^{-3} curve illustrates the drop in transmission resulting from molecular oxygen absorption.

Since in convective systems most of the liquid precipitation causing attenuation and vapour occurs low in the atmosphere the spaceborne nadir-pointing radars are much less affected by the attenuation than the zenith-pointing surface-based radars. It has been reported that attenuation caused by heavy precipitation to the surface millimeter wavelength radars leads to misclassification of deeper precipitation modes into the shallow modes of precipitation (Stephens and Wood [2007]). The extent of this effect cannot be fully quantified yet.

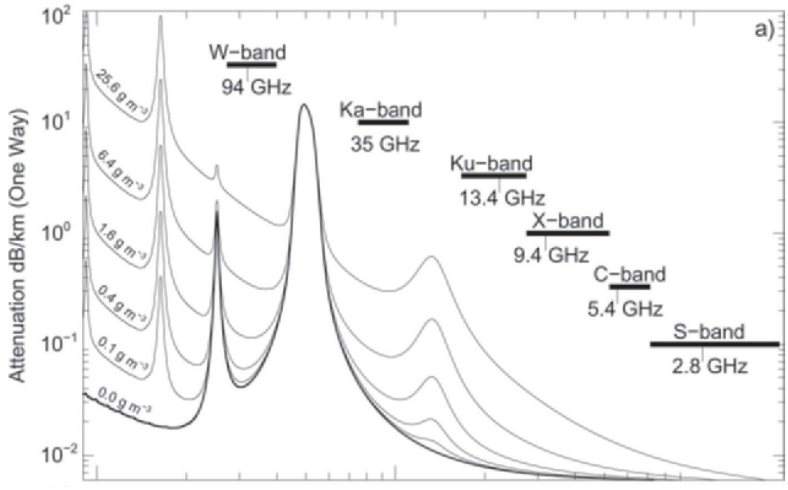

Figure 2.1: Atmospheric transmissivity versus wavelength for a 1 km horizontal path for different water vapour amounts. Transmissivity for the 0 g m^{-3} curve illustrate the drop in transmission resulting from molecular oxygen absorption. Image from [Kollias et al., 2007].

The power scattered back to the radar from distributed targets is strictly related to the area of the target and for calculating it the term backscattering cross sectional area (usually denoted σ_b) has been coined. It is a function of size, shape and composition of the target but also of the radar wavelength. The calculation of backscattering cross section can be complicated for complex targets, although often

the spherical approximation is good enough to describe the backscattering properties of meteorological targets.

When the particle is much smaller than the wavelength λ of the impinging radiation, the phase shift across the particle is negligible and the back scattering cross section can be estimated using Rayleigh theory and is given by:

$$\sigma_b = \frac{\pi^5 |K|^2 D^6}{\lambda^4} \tag{2.1}$$

where D is target diameter and K is the complex dielectric factor of water. "Small" compared by the wavelength usually means D / $\lambda < 0.1$. In Rayleigh region the backscattering cross section of a particle is proportional to the sixth power of the particle diameter D. For the ensemble of particles contained in the backscattering radar volume V_c, the average radar backscatter cross-section is defined as:

$$\overline{\sigma_b} = \sum_j \sigma_j = \frac{\pi^5 |K|^2}{\lambda^4} \sum_j D_j^6 \tag{2.2}$$

From this the radar reflectivity can be defined as (where subscript j refers to an individual target within the unit volume):

$$\overline{\eta} = \frac{\sum_j \sigma_j}{V_c} = \frac{\pi^5 |K|^2}{\lambda^4} \frac{\sum_j D_j^6}{V_c} \tag{2.3}$$

A parameter of high importance in radar meteorology, from which most of the information is derived, is designated with the symbol Z and called the radar reflec-

tivity factor:

$$Z = \frac{\sum_j D_j^6}{V_c} = \int_0^\infty N(D) D^6 dD \tag{2.4}$$

where $N(D)$ is the particle size distribution. The reflectivity factor Z is normally expressed in logarithmic units of dBZ relative to 1 $mm^6 m^{-3}$. The radar reflectivity factor is derived from processing of the power of the received radar echo and provides microphysics information about the clouds and precipitation. In this work, as the "real" reflectivity is not used, the reflectivity factor which is configuration (radar frequency) dependent is referred to as reflectivity for short.

For larger hydrometeors (compared to the wavelength) the radar backscattering has to be calculated using Mie theory. This involves computations of scattering properties using Bessel functions while the scattering properties being expressed in terms of series depending on the size parameter $x = \pi m_m D/\lambda$. In the so called resonance region, where backscattering cross section can actually decrease as the size increases. For a 94 GHz radar a large portion of hydrometeors falls into this region.

When the hydrometeor is even larger, usually meaning D / $\lambda > 10$, the backscattering cross section of the target is equal to the geometric area, as given by:

$$\sigma_b = \frac{\pi D^2}{4} \tag{2.5}$$

The normalized backscattering cross sections of spherical targets as a function of the relative size of the target for mentioned three regions are shown in Fig. 2.2.

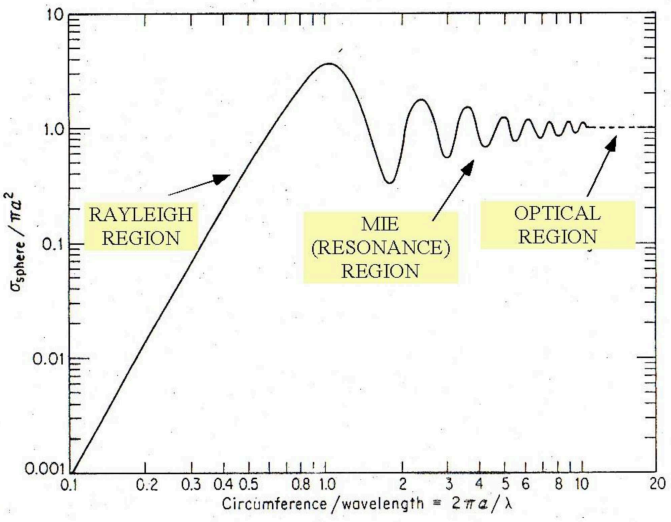

Figure 2.2: Normalized backscattering cross section for a sphere as a function of circumference, normalized by a radar wavelength λ, showing three types of scattering regions. The symbol a is scatterer radius. Image from [Skolnik, 2001].

The Radar Equation describes the relationship between transmitted power of the radar and the expected returned power. Given this equation, it is possible to design radar characteristics to obtain particular levels of sensitivity. The radar equation is given by

$$E[P_r] = \frac{P_t g^2 \lambda^2 \eta c \tau \pi \theta_1^2}{(4\pi)^3 r^2 l^2 16 \ln 2} \tag{2.6}$$

where P_t, g, η, τ, θ_1 and l are the transmit power, antenna gain, reflectivity, pulse length, beamwidth, and the loss factor, respectively.

2.1.1 Operation of Pulsed Doppler Radar

The operation of a pulse radar is shortly described here with the help of a simple block diagram displayed in Fig. 2.3. The source of the electromagnetic radiation radiated by a radar is the transmitter. Due to their high average power and good performance, klystrons transmitters are typically used in spaceborne radar systems. The transmitter is turned on and off (modulated) to generate series of high-power pulses with specified duration. The device used to control the whole system is a master clock (timer) and determines how often the radar will transmit a signal into space. It also can control other subsystems such as the signal processor or displays. The duplexer or RF switch is added to the radar system to protect the receiver from high power of the transmitter because of the tremendous difference in power levels between the transmitting and receiving chain. The duplexer allows a single antenna to be used on a time-shared basis for both transmitting and receiving. The signal is delivered to the antenna by a waveguide and is radiated into space. The type of the antenna (parabolic reflector, planar arrays or phased arrays) is responsible for shaping the radar beam. For a given radar frequency the bigger the antenna, the smaller the antenna beam pattern and the better the angular resolution of the radar.

Energy from the transmit pulses propagate through space until they interact with reflectors, such as water or ice particles or insects, etc. This interaction causes some of the transmitted energy to be reflected back to the radar antenna, along with

phase modulation caused by their motion.

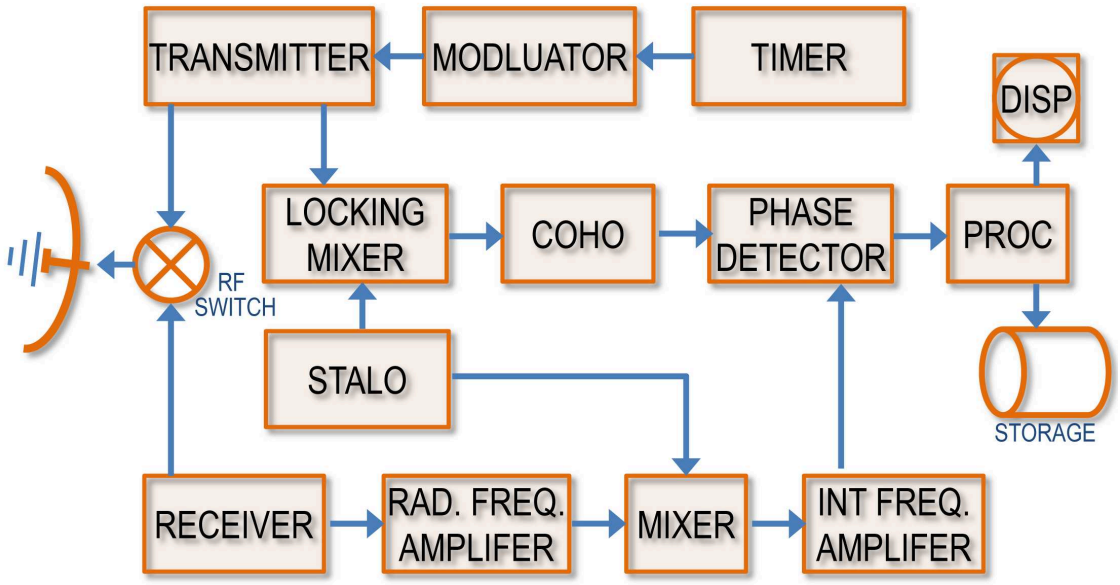

Figure 2.3: Block diagram of a simple Doppler radar. Transmitting path consist of transmitter, modulator and master clock (timer), while receiving subsystem from receiver, amplifiers, mixers. The following abbreviations apply: STALO = stable local oscillator; COHO = coherent oscillator; Proc = processing unit; Disp = display.

The ability of Doppler radar to detect slight phase shifts (motion) depends critically upon the system being able to maintain constant transmitter frequency and phase relationship from one pulse to the next. In order to do this Doppler radars contain a stable local oscillator (STALO) which maintains very stable frequency. The signal from STALO is mixed with the frequency of the transmitter in the locking mixer. The signal is then sent through a coherent oscillator which amplifies the signal while maintaining the phase relationship with the initially transmitted signal.

Then the signal is compared with the signal coming from the receiver path in the phase detector.

The signal intercepted by the antenna goes trough the receiver circuit. The function of the receiver is to detect even weak signals received by the antenna. The received signal is shifted by a Doppler effect by an amount $\pm f_d$. The plus sign applies when the target is closing to the radar (i.e. the distance between the radar and the target is decreasing). This signal is then amplified by the radio frequency amplifier. Most of the radar receivers are of the superheterodyne type, i.e. the received signal is mixed with the reference signal at a frequency which is lower and different from the transmitting frequency (Rinehart [2004]). This mixing of received signal (in mixer) with the reference frequency f from STALO converts the signal to a lower frequency of $f \pm f_d$ which in turn is more easily processed. The phase of the transmitted pulse is preserved and the lower frequency signal is then further amplified in the intermediate frequency amplifier. The received signal and a sample of transmitted signals are sent to a phase detector, which determines how much the received signal has been shifted relative to the transmitted one. Then the signal is sent to various processing units and Doppler filters. The Doppler filter allows the difference frequency to pass and cancels the higher frequencies (matched filter). A lower frequency cutoff removes the transmitter signal and clutter echoes, the upper frequency cutoff is determined by the maximum radial velocity expected from the targets. Then the signal is sent to signal processing unit which converts the analog

(voltage) signal to digital producing I and Q time series. Finally the data are analysed by the signal processor to estimate radar products (reflectivity, Doppler velocity, spectrum width) and can be displayed on screens, stored or sent to ground station in case of spaceborne radars. The signal bears the range-phase information for each burst of microwaves and is sampled at a specified point in time relative to the onset of the transmission pulse. The time of sampling defines the range of the phenomenon i.e. the distance the radar wave travels to the target and back to the antenna.

2.1.2 Doppler Frequency Shift

A pulse radar exploits the doppler shift for detecting moving targets or wind shear. Doppler effect changes the frequency of the electromagnetic signal which propagates from the radar transmitter to a moving target and then back to the radar antenna. If the range to the target is R then the total number of wavelengths λ in the two-way path from the radar to the target and return is $2R/\lambda$ (Skolnik [2001]). In realistic Doppler radar systems the measurement of the Doppler shift in a single backscattered pulse is not practical. Instead the change of the echo's phase angle from one transmitted pulse to the next is measured. Phase angle is proportional to the scatterer's range and equals twice the number of wavelengths between the radar and the scatterer. In such case each wavelength corresponds to a phase change of 2π radians. The total phase change in the two-way propagation path is then given

as:

$$\phi = 2\pi \frac{2R}{\lambda} = 4\pi R/\lambda \tag{2.7}$$

If the target is moving then R is changing and so will the phase. Differentiating Eq. 2.7 with respect to time results in the rate of change of phase, which is defined as angular frequency ω_d:

$$\omega_d = \frac{d\phi}{dt} = \frac{4\pi}{\lambda}\frac{dR}{dt} = \frac{4\pi v_r}{\lambda} = 2\pi f_d \tag{2.8}$$

where $v_r = dR/dt$ is the radial velocity (m/s) or in other words the rate of change of the target range with time. The rate of change of ϕ with time is the angular frequency $\omega_d = 2\pi f_d$, where f_d is the Doppler frequency shift. This results in:

$$f_d = \frac{2v_r}{\lambda} = \frac{2fv_r}{c} \tag{2.9}$$

where $f = c/\lambda$ is radar frequency and c $[m/s]$ is the propagation speed of light.

2.1.3 Doppler Spectrum

For atmospheric radars the target is typically represented by a large number of distributed targets (such as raindrops, hail, graupel, snow flakes, ice pellets etc.) of different shapes and sizes and moving at different speeds due to the turbulent motions within the volume, wind shear and due to their fall speeds. The velocity field is therefore represented by a spectrum of velocities. Doviak and Zrnic [1984]

showed that radar signal received from meteorological targets is well represented by a narrowband gaussian process. There is few factors to support this claim. The number of scatterers in the investigated volume is large; the pulse volume contains multiple point scattering sources which causes the spread of the phases from 0 to 2π to be returned; the volume is large compared to the transmitted wavelength and the hydrometeors are in motion due to wind shear, turbulence and varying fall speeds. This gives rise to a signal with a gaussian probability density function whose phase is uniformly distributed between 0 - 2π. The intensity of such signal is exponentially distributed (Zrnic' [1975]). Because all particles are moving with some mean radial velocity there is a mean frequency of the Doppler spectrum that is shifted from the transmitted frequency. Moreover as the hydrometeors are in motion with respect of each other there is also Doppler spread, often referred as the width of the Doppler spectrum.

2.2 Technical Constrains to Develop Doppler Capability in Space

2.2.1 Coherency Time and Doppler Spectral Width

In order to achieve good accuracy of Doppler velocity estimates coherent measurements of phase changes between successive radar returns are required (Amayenc et al. [1993]). This means that the period (IPP = 1/PRF, Intra Pulse Period)

between the pulses should be significantly shorter than the decorrelation time of atmospheric targets.

In case of spaceborne radar, decorrelation of radar signals occurs for three reasons (Schutgens [2008]). First, there is the variation of the line-of-sight velocities within IFOV. Second, there is the variation in the contribution of the same atmospheric volume to the receiver voltage as the antenna gain pattern moves over the atmosphere. Third, there is the variation in the line-of-sight velocities of the same atmospheric volume as it is viewed from different angles by the moving radar. Schutgens [2008] concluded that the first time-scale is significantly smaller than the other two for EarthCARE-like configuration, thus is the key factor for the decorrelation of the receiver voltages. The resulting timescale is given by:

$$T_{dec} = \frac{\lambda}{2\sqrt{2}\pi\sigma_D} \tag{2.10}$$

where σ_D is total Doppler velocity spectral width. For spaceborne profiling radars σ_D can be expressed as the sum of independent sources of spread (of the Doppler spectrum (Kobayashi et al. [2002])):

$$\sigma_D^2 = \sigma_{PSD}^2 + \sigma_{WS}^2 + \sigma_T^2 + \sigma_{SM}^2 \tag{2.11}$$

σ_{PSD} is spread due to the particle fall velocities - this is somewhat equivalent to the fact that the greater the range of particle sizes the greater the spread of the

Doppler spectrum, σ_{WS}: spread due to the wind shear within the radar sampling volume and proportional to vertical resolution of radar and σ_T: broadening due to turbulent motions at scales smaller than the radar sampling volume. Small raindrops and ice particles respond rapidly to changes in air velocity and will exhibit the turbulent motions. On contrary the large raindrops and hail will not respond instantaneously to small scale turbulence (Battan [1973]). The σ_{PSD} ranges from few cm/s for cloud droplets and ice crystals to 1-2.5 m/s for raindrop size distributions, thus it is not negligible in heavy rainfall. Apart from extreme turbulence and wind shear conditions, the second and third term have negligible impact.

The biggest contribution in Eq. (2.11) is provided by the σ_{SM} term, which is the spread caused by the coupling between the satellite motion and the vertical wind shears of the horizontal winds (Kobayashi et al. [2002]):

$$\sigma_{SM} = \frac{\theta_{3dB}}{4\sqrt{log(2)}}[(-V_{sat} + \kappa_{zx}H_{sat})^2 + (\kappa_{zy}H_{sat})^2] \tag{2.12}$$

where θ_{3dB} is the 3-dB beamwidth of the antenna, V_{sat} and H_{sat} are the component of the satellite velocity orthogonal to the line of sight and the altitude of the satellite, respectively. κ_{zx} and κ_{zy} are the horizontal shears of the vertical wind. The altitude of the satellite determines the satellite motion while θ_{3dB} depends on the antenna size (θ_{3dB} equal to $1.22\lambda/D_A$ for spherical antennas, where λ is the radar wavelength and D_A is the antenna diameter).

For a Gaussian circular antenna pattern and in case of very weak vertical wind

shears Eq. (2.12) reduces to (Tanelli et al. [2002a]):

$$\sigma_{SM} = \frac{\theta_{3dB} V_{sat}}{4\sqrt{\log(2)}}. \tag{2.13}$$

Recalling the meaning of the coherency time, and assuming for simplicity that the σ_{SM} is a dominant factor for radars at LEO ($\sigma_D \approx \sigma_{SM}$), the acquisition of coherent samples will depend on the selection of the sufficiently large PRF. As given in Doviak and Zrnić [1993] the condition would be fulfilled for:

$$PRF \geq \frac{4\pi\sigma_D}{\lambda} \tag{2.14}$$

which for LEO radar with narrow beamwidth is transformed to:

$$PRF \geq \frac{1.2\pi V_{sat}\theta_{3dB}}{\lambda} \tag{2.15}$$

For typical parameters for EC radar ($\theta_{3dB} = 0.095°$, 94 GHz and $V_{sat} = 7.6km/s$) and for 35 GHz CLDY radar ($\theta_{3dB} = 0.095°$) and for quite considerate $\sigma_{SM} = 3.8m/s$ the PRF values should be:

PRF $\geq$ 14900 Hz for 94 GHz

PRF $\geq$ 5500 Hz for 35 GHz

The corresponding decorrelation time T_{dec} (coherence time) is approximately 93 μs for EC. The operational range of PRF for EC radar is between 6.1 - 7.5 kHz, which

have significant impact on Doppler estimates, explained further in the thesis. The upper bound is set up by the constraint to observe the entire troposphere.

For deep convection the Eq. (2.12) has to be retained as the wind shears cannot be neglected (Battaglia et al. [2013]).

The equations given so far hold true for uniform beam filling conditions. For nonuniform beam filling (NUBF), which are likely to occur in convective clouds and for typical radar footprint sizes the overall effect on σ_{SM} where the contribution of the satellite velocity to the Eq. (2.12) can be significantly different. This depends if the current footprint of the radar consist of two or more highly reflective cells, much smaller than the radar footprint, on opposite sides along the satellite movement or there is a single highly reflective cell present in the radar footprint and any variation of those two cases when the effect is not balanced. This effect can be only assessed using full 3D simulator and will be discussed in Sect. 6.5

2.2.2 PRF vs Range

The maximum unambiguous range r_{max} and maximum unambiguous velocity u_{max} of a conventional pulsed Doppler radar are related by (Doviak and Zrnic [1984], Miller and Rochwarger [1972])

$$r_{max}|u_{max}| = \frac{c\lambda}{8} \tag{2.16}$$

where c is the speed of light and λ is the radar wavelength. While this ambiguity

relation applies to all weather radars, millimeter-wavelength radars face a particularly stringent limit due to the increase in Doppler frequency shift with increasing operating frequency. This high Doppler shift often forces the operation of millimeter-wave radars to sacrifice range and accept multiple folding in the velocity data, even for moderate winds. For example, at 3 mm (95 GHz) wavelength the product of the maximum velocity and range is so small that for a u_{max} of $\pm 8 m s^{-1}$, r_{max} is reduced to 14 km. These limitations may be acceptable during zenith observations of some clouds and precipitation; longer-range capability is often necessary during horizontal measurements, however, for weather phenomena such as convective clouds and storms require the ability to measure much higher wind speeds.

Chapter 3

EarthCARE Mission and Future Radar Concepts

3.1 EarthCARE Mission

The EarthCARE mission is a space mission planned by the European and Japanese space agencies (ESA and JAXA). The project is part of ESA's Living Planet Programme. Its acronym stands for Earth Clouds, Aerosols and Radiation Explorer. The EarthCARE mission aims at improving the understanding of cloud-aerosol interactions and the radiation effects of clouds and aerosols with the goal to include them reliably in climate and numerical weather prediction models (Hlire et al. [2007]). The mission will employ high-performance lidar and radar technology that has never been flown in space before (ESA Earthnet Online [2013]). EarthCARE is

scheduled for launch in 2016 on a sun-synchronous orbit and local time 14:00 with the mean altitude of an spacecraft expected to be 393 km and a repeat cycle of 9 days.

The EC mission is of primary interest for the purpose of the thesis. The Earth-CARE Doppler radar parameters have been used to study the possibility to obtain valuable data from deep convective systems.

3.1.1 Payload

The EarthCARE satellite will accommodate four instruments:

I –> Cloud Profiling Radar (EC-CPR)

II –> Atmospheric Lidar (ATLID)

III –> Multi Spectral Imager (MSI)

IV –> Broad Band Radiometer (BBR)

The radar and lidar are active whilst MSI imager and BBR radiometer are passive instruments. The observation geometry of EarthCARE instruments is shown in Fig. 3.1. This instrument suit has been optimized to provide co-located samples of the state of the atmosphere along the flight track, complemented by across-track information from the MSI and from BBR. The centres of the instrument footprints will be located as close together as possible to ensure a good co-registration. The

synergy of those four instruments will be utilized to provide reliable measurements of clouds and aerosols and their interactions with radiation.

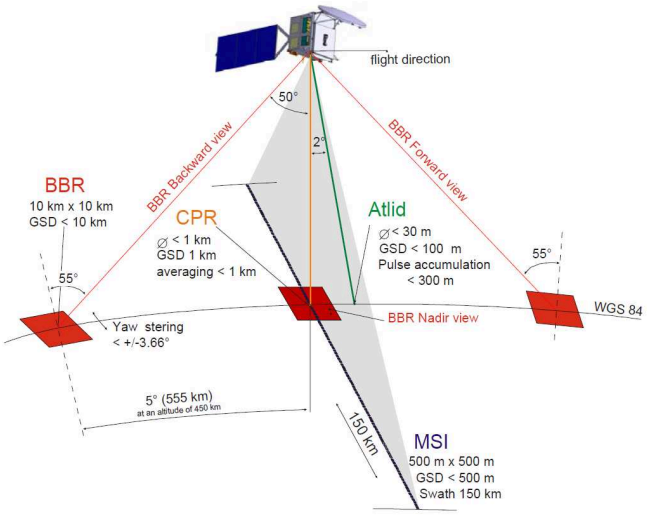

Figure 3.1: EarthCARE satellite observation geometry, showing the four instruments' field of view. After: Hlire et al. [2007]

A single wavelength (355nm) lidar will provide vertical profiles of aerosols and thin clouds and will be used to derive cloud top heights and aerosol optical depths. Small footprint (<30m) of the instrument will be used to reduce effect of multiple scattering (Hlire et al. [2007]).

The MSI is a seven channel, 150 km swath imager and will provide across-track information on the horizontal structure of clouds and aerosols with channels in visible, near infrared, shortwave and thermal infrared. It will provide complimentary data on cloud type, texture, top temperature and cloud phase.

The BBR will provide an estimate of the short-wave reflected and the long-wave emitted fluxes at the top-of-the-atmosphere. The instrument is a two-channel

radiometer, receiving the short-wave and the total radiation. The long-wave channel is obtained by subtracting the short-wave component from the channel covering the complete spectral range. It has three fixed viewing directions pointing in nadir, forward and aft-directions. The size of the footprints will be 10 km by 10 km.

The EarthCARE Cloud Profiling Radar is described in detail in Sect. 3.2.

Having these four instruments onboard one platform has significant benefits over the concept of constellation flying. Not only this enables more accurate cooperation of instruments but also counteracts situation which occurred to the A-Train constellation CloudSat's radar on 17 April 2010. A battery malfunction caused the CloudSat spacecraft to lose formation with the A-Train. While CloudSat data collection resumed on 27 October 2011, CloudSat returned to the A-Train constellation on 15 May 2012. However a maneuver to achieve footprint overlap with CALIPSO satellite was performed only on 18 July 2012. Until that date the CloudSat products requiring the MODIS and CALIPSO data were not produced (CloudSat Online [2013]) which caused significant loss of valuable data.

3.1.2 EarthCARE Contribution

The difficulty of representing clouds and aerosols and their interactions with radiation, constitutes a major source of uncertainty in prediction of climate change using numerical models of atmospheric circulation. Accurate representation of cloud processes is also essential for the improvement of numerical weather predictions. To

achieve this goal one needs to verify if the models are correctly representing clouds and aerosols in the present time. However there are no global datasets which would provide simultaneously the vertical profiles of cloud and aerosol characteristics together along with vertical temperature and humidity profiles and TOA radiance. This is needed to validate the model parameterizations of cloud processes with respect to both water and energy fluxes. The vertical profiles of the atmosphere are important in controlling the radiative transfer processes, which in turn affect the heating profiles responsible for the dynamics. Large part of uncertainty in modelled global climate change arises from limited knowledge in interactions of clouds and aerosols with radiation.

Since clouds act on both the short-wave and the long-wave radiative fluxes, partial compensation of opposite effects makes even the sign of net cloud radiative feedback uncertain. We also don't know the size of today's anthropogenic aerosol short wave forcing over many regions of the globe. The knowledge of aerosols and cloud properties is inadequate for reliable calculation of the likely evolution of indirect aerosol forcing in climate models. Improved understanding of cloud-aerosols-radiation interactions is needed for reliable projections of climate change.

Reliable prediction of future climate change requires a significant reduction of the uncertainty of clouds feedback for the estimation of both temperature and precipitation trends. This can be validated by correct representation of cloud-water-ice processes, which are not yet available.

The EarthCARE satellite has been designed to provide global distribution of vertical profiles of cloud and aerosol field characteristics to provide essential input data for numerical modelling and global studies. The main focus is in divergence of radiative energy, aerosol-cloud-radiation interaction, the vertical distribution of water and ice and their transport by clouds, the vertical cloud field overlap and cloud-precipitation interactions.

3.2 EarthCARE CPR

The objective of the Cloud Profiling Radar (CPR) is to provide vertical profiles of cloud structures along the sub-satellite track. The EC-CPR has two major new features: higher sensitivity than any spaceborne cloud radar, enabling detection of almost all radiatively significant ice clouds (Baptista [2004]); Doppler shift measurement capability to detect the vertical motion of cloud and rain particles overlaid on vertical wind to identify cloud types, drizzle and cloud droplet fall speed. The CPR features also a unique capability of penetrating deep into lower cloud layers, which cannot be viewed by the MSI or ATLID.

3.2.1 CPR Characteristics

The EC-CPR cloud radar will operate at 94 GHz frequency to maximize sensitivity and provide a narrow beamwidth even with a small antenna. The EC-CPR has a 2.5 m antenna which is particularly important for the performance in Doppler

Table 3.1: EarthCARE radar characteristics table

Radar parameters (unit)	EC value
Transmitter Frequency [GHz]	94
Transmitted Pulse Duration [μs] (Length [m])	3.3 (500)
Antenna Beamwidth [degrees, along track]	0.095
Antenna Beamwidth [degrees, cross track]	0.095
Pulse Repetition Frequency (PRF)[kHz]	6.1-7.5
Along-track Integration [km]	0.5 (Z); 1 (V_D)
Noise-per-single-pulse [dBZ]	-21.5
Sensitivity at TOA (10 km integration) [dBZ]	-36
Projected on ground spacecraft velocity [km/s]	7.2
Number of active pulses in 1 burst	22
Number of silent pulses in 1 burst	2

measurements. The radar specifics, describing the main technical features of EC-CPR, are shown in Table 3.1.

The EarthCARE CPR sampling scheme states that radar will send 22 pulses followed by 2 'empty' pulses to measure background noise. Then the level of background noise will be subtracted from the received signal.

3.2.2 Requirements for CPR Accuracy

To obtain high performance in Doppler measurement, a high pulse repetition frequency (PRF) is required. The EarthCARE CPR features a variable PRF scheme to accommodate changes in satellite altitude in orbit (Baptista [2004]). The PRF range will span from 6100 Hz to 7500 Hz. Specially, a higher PRF is used in the high latitude regions by reducing the top of the observation range window to 12 km. This corresponds to the measurement range from -0.5 km to +12 km (-0.5 km

to +20 km in tropics). The unfavorable choice of the PRF for convective regions connected to unambiguous range is explained in Sect. 2.2.2.

EarthCARE Mission Advisory Group [2006] publication sets the accuracy requirements for mean Doppler velocity estimates from EarthCARE CPR. The goal requirement is to achieve 1 m/s at 1 km horizontal resolution (at -14 dBZ for any PRF) and 0.2 m/s at 10 km horizontal resolution (to be achieved at -14 dBZ reflectivity and highest PRF). Threshold requirement is set to 1 m/s at 10 km horizontal resolution (to be achieved at -19 dBZ for any PRF).

According to Baptista [2004] at high latitudes, velocities can be measured to better than 0.2 m/s for 10 km horizontal integration provided Z is > -18 dBZ, which, from the airborne analysis, includes 96% of the ice mass flux in cirrus. Convective motions in the tropics can be estimated to 1 m/s with 1 km horizontal resolution for Z > -17 dBZ, which should detect 95% of the tropical cirrus ice mass. These requirements will be further discussed in Chapter 6.

3.2.3 EarthCARE CPR Compared to Current Radar Missions

EarthCARE capitalizes on the experience gained from previous radar missions. The Tropical Rainfall Measuring Mission (TRMM) was the first spaceborne radar for rainfall observation. However the satellite footprint size of 4.3 km is larger than the typical size of rain cells or convection systems. As it was found by Goldhirsh

and Musiani [1986b] the median convective cell size for convective storms off the Virginia coast is only 1.9 km. Such a large footprint cause non uniform spread when observing convection within radar footprint and thus may cause nonuniform beam filling (NUBF) effects which introduce biases in radar measurements. EarthCARE will decrease this effect by having a radar footprint of 665 m.

Zipser et al. [2006] studied the most intense thunderstorms within the coverage of TRMM (35 deg S to 35 deg N latitude) and defined the general characteristics of tropical convection, focusing on four parameters of intense convective storms: radar reflectivity, lightning occurrence, passive microwave brightness temperatures, and visible/infrared channels. As the Doppler velocity is not available on TRMM, Zipser et al. [2006], Cecil et al. [2005], and others used proxies to relate the storm intensity with 1) increasing height of reflectivity echo above 10-km altitude 2) decreasing brightness temperatures at 37 and 85 GHz and 3) greater lightning flash rates. The common property governing all of these proxies is the strength of the vertical motions (Heymsfield et al. [2010]); thus, there is a need to better understand the relationship between microphysical and kinematic processes in deep convection.

The TRMM follow-on mission: the Global Precipitation Measurement (GPM) Core mission is scheduled to launch in February 2014. The GPM Core mission will have an additional 35 GHz radar to complement the single 14 GHz radar deployed on the current TRMM satellite. The main focus of the mission is to provide more accurate precipitation estimates. While simultaneous measurements by the overlap-

ping Ka/Ku-bands of the radar can provide new information on particle drop size distributions over moderate precipitation intensities, the 14 and 35 GHz radars will detect only dense (e.g. precipitating) clouds. As the radar sensitivity is about 40 dB lower than the EarthCARE CPR it will not be able to detect most of the occurring clouds (Baptista and Leibrandt [2001]).

The CloudSat Cloud Profiling Radar (CPR) is a 94-GHz nadir-looking cloud radar which was launched in 2006. It flies in formation with the A-TRAIN satellites on a 705 km orbit enabling the most detailed study of clouds to date. It is among the first few satellites to study clouds on a global scale, providing statistics on the vertical structure of clouds, rainfall patterns and cloud-aerosol interactions. The CloudSat mission has already exceeded its planned 3 year lifetime and keeps delivering data. The EarthCARE can be seen as a follow on mission which will assure a continuous dataset of radar data on a global scale. It uses same frequency, shares some technical achievements and philosophy; however EC-CPR will have Doppler capability and will be more sensitive by 6.5 dB. Because the small size of the liquid droplets in certain clouds the sensitivity is very important. As has been stated in Baptista and Leibrandt [2001] the EC will be able to detect 40 % of stratocumulus clouds as opposed to CloudSat's 20 %. To accurately derive cloud microphysical parameters the lidar-radar measurements have to be combined. This will be also fulfilled by EC satellite, where data from lidar and radar will be collocated.

The EarthCARE mission 94-GHz Doppler radar will offer an excellent opportu-

nity for systematic measurements of sedimentation rates of hydrometeors on a global scale. Despite the challenges associated with the quality of the Doppler estimates from the EarthCARE-CPR due to limitation in hardware and operational parameters the weather and climate research community are preparing to use the CPR observations for evaluating the representation of cloud-scale processes in numerical models.

3.2.4 EC-CPR Products

EC-CPR is expected to provide radar reflectivity and mean Doppler velocity measured at nadir. The reflectivity will be provided at 500 along-track resolution. The mean Doppler velocity will be averaged for 1 km along-track distance to improve accuracy and outputted as joint standard grid product along with reflectivity integrated for 1 km. Further integration of 10 km is envisaged for stratiform regions for the investigation of ice sedimentation rates.

The Doppler radar is expected to provide:

I –> vertical motion

II –> feature mask

III –> hydrometeor target classification

IV –> ice water content and effective radius

V –> liquid water content and effective radius

VI –> precipitation / snow classification

VII –> melting layer identification

3.3 Dual Wavelength Systems Targeting Convection

Apart from EarthCARE CPR three other radar concepts targeting convection has been considered in the thesis. This includes the proposed mission for the International Space Station (ISS) - CLDY, the NASA ACE mission and future mission with similar to EC parameters however with significantly bigger antenna. Each of the radar concepts use both 94 GHz and 35 GHz frequency. The addition of 35 GHz channel is expected to penetrate a larger portion of deep convective systems, which in turn comes at the cost of a larger beam-width (approx 2.7 times larger than the W-band for the same antenna size). Even though the names of the missions are used in the thesis and simulations were performed according to their technical radar specifications however the satellites' orbits have been changed to 400 km for better comparison with EarthCARE mission. The reasoning behind this is that the ISS station's orbit varies with time but oscillates around EC orbit of 400 km. It was significantly risen after space shuttle's retirement but is also connected to solar cycle activity and radiation factors on the crew onboard. The ACE orbit is still under discussion and prone to change, with the 450 km orbit preferred by the use of the active instruments and the 705 km preferred for international and interagency contributions via formation flying in NASA's A-Train. The formation flying with

EarthCARE is also under consideration, augmenting EC observations. Due to this facts it has been assumed for simulation purposes that orbit height for all three concepts are the same as the EarthCARE in the thesis. It is also assumed that all concepts will use novel signal processing method described in Chapter 7.

3.3.1 ISS Climate Dynamics Mission (CLDY)

The CLDY (Climate Dynamics Mission) is a proposed mission designed to improve the understanding of critical convective cloud and precipitation processes that determine the structure, scale, intensity and longevity of the major storm systems of the planet (CLDY-Proposal [2011]). The 94 GHz radar onboard ESA-ISS mission proposed for CLDY will use Dual Polarization mode. The payload on CLDY is a nadir pointing, dual frequency (35/94-GHz), high vertical resolution and high sensitivity radar that will allow the characterization of light to heavy precipitation events from shallow to deep convective systems. The radar will provide copolar and cross-polar moments to provide estimates of depolarization ratio. A cross-polarimetric measurements will be used to improve the quality of the data, discriminate between different hydrometeor types, for identification of the melting layer and to identify multiple scattering events. Existing and near-future planned spaceborne cloud and precipitation radar missions lack the polarization diversity mode, thus the CLDY can be the first spaceborne mission with such capability.

Cloud microphysics can be more accurately characterised using both reflectivity

and terminal fall speed which is particularly true for non-spherical particles. The ISS-CLDY mission is strongly supported by International Working Group on Spaceborne Snowfall Measurements for advancing snowfall measurements, which right now largely depends on the CloudSat reflectivity measurements (Bennartz et al. [2011]).

3.3.2 NASA ACE

NASA's Aerosol-Cloud-Ecosystems (ACE) Mission will be a mission consisting of four instruments (dual frequency Doppler cloud radar, lidar multi-spectral imaging polarimeter and multi-channel spectrometer). ACE mission has been recommended in 2007 by NASA Earth Science Decadal Survey Studies for launch within next the decade.

The ACE mission has been designed to achieve several goals:

I –> narrow down the uncertainty in aerosol-cloud-precipitation interaction and quantify the role of aerosols in climate change.

II –> providing profiles of cloud properties and precipitation.

III –> distinguishing cloud droplets and raindrops, and ice crystals and snow, including particle size and cloud optical properties

IV –> provide more comprehensive knowledge of cloud processes, especially advancing knowledge of the ice phase and the partition of liquid-phase and ice phase.

V –> help climate modelers make more precise predictions of climate change.

VI –> measure the ocean ecosystem changes and precisely quantify ocean carbon uptake.

VII –> improve air quality forecasting by determining the height and type of aerosols being transported long distances.

Achievement of these goals will result in enhanced capabilities to observe and predict changes to the Earth's hydrological cycle and energy balance in response to climate forcings. The properties and behaviors of cloud hydrometeors are known to change in the presence of aerosol while clouds are also known to significantly process and alter the aerosols population.

3.3.3 Large Antenna Mission

The "large antenna" mission is an EarthCARE-like mission however with 10 m antenna, twice larger (four times) than ACE (EC) mission. For short, this concept is nicknamed "10 m" antenna while the previously mentioned two radar concepts have already been proposed (ACE and CLDY), this one is used as reference concept. It uses large antenna which is not technologically available to launch by current launch vehicles. However it showcases how an increase in the radar antenna impacts the Doppler products from spaceborne radar systems and the differences in the achieved accuracy. It is believed that antennas of this size will be available in near future.

Table 3.2: Parameters of spaceborne Doppler radars used for simulations and discussion in the thesis.

Configuration	Frequency	Altitude	Beamwidth	Pulse duration	PRF range	Antenna
EarthCARE	94.0 GHz	400 km	0.095°	3.3 μs	6.1÷7.5 kHz	2.4 m
CLDY-35	35.0 GHz	400 km	0.255°	1.2 μs	5÷14 kHz	2.4 m
ACE-35	35.0 GHz	400 km	0.128° × 0.215°	1.67 μs	5÷7.5 kHz	2.5 × 5 m
ACE-94	94.0 GHz	400 km	0.048° × 0.079°	1.67 μs	5÷7.5 kHz	2.5 × 5 m
10m-35	35.0 GHz	400 km	0.064°	1.67 μs	5÷7.5 kHz	10 m
10m-94	94.0 GHz	400 km	0.024°	1.67 μs	5÷7.5 kHz	10 m

All radar configurations that were used for simulations in the thesis are listed in the Table. 3.2.

Chapter 4

Airborne Doppler Radar Observations

A comprehensive view of clouds that includes their physical dimensions, vertical and horizontal spatial distribution, detailed microphysical properties and the dynamical processes producing them are ideally required to improve understanding of the radiative impact of clouds on the climate system. In order to study the EarthCARE radar performance it is very useful to have a good representation of relevant cloud parameters. While there is no satellite Doppler velocity measurements yet available there are a few datasets of airborne measurements obtainable in W, K_a and X bands. The nadir airborne radar data can give insight on what to expect from satellite radar measurements, which aside from the high velocity of the satellite, can provide an analogous view to the spaceborne instrument and challenges related to it. Specifi-

cally for this study, aircraft data can shed light on the magnitude of mean Doppler velocity as well as the magnitude of reflectivity gradients. This is particularly important for a W-band observations of convection where ground based measurements are fully attenuated before reaching cloud tops and the fact that airborne data have high spatial resolution compared to expected spaceborne resolution. One of few such datasets was acquired in 2002 during NASA's CRYSTAL-FACE campaign.

4.1 Observation During CRYSTAL-FACE Campaign

4.1.1 Description of the field campaign

The Cirrus Regional Study of Tropical Anvils and Cirrus Layers - Florida Area Cirrus Experiment (CRYSTAL-FACE) was an international field experiment focused on various aspects of the life cycle of upper-tropospheric clouds, cirrus cloud formation including improving our understanding of the evolution of tropical anvil clouds generated by deep convective systems (Jensen et al. [2004], Rickenbach et al. [2008]). This is important since anvil clouds reflect incoming solar radiation while trapping longwave radiation, and they are the key regulator of the global radiation balance, especially in the tropics (Fu et al. [1995]). One of the aims of the campaign was to determine the role of thunderstorm intensity (i.e. updraught strength) on the characteristics of thunderstorm generated cirrus (altitude, location, longevity). During

the campaign up to five aircraft were flying including the NASA high-altitude (flying over 20 km) ER-2 aircraft, which flew above the convection. The inaugural flight of the 94 GHz Cloud Radar System (CRS) took place during the CRYSTAL-FACE campaign. This was also the first time a millimeter wavelength radar system was flown on a high altitude aircraft platform capable of overflying tropical convection (Stephens and Wood [2007]). The instruments onboard the ER-2 aircraft obtained comprehensive active and passive remote sensing measurements of cirrus and the convection that generates the cirrus. In particular, during this campaign there was a rare occasion to inter-compare data from X and W band airborne radars.

The experiments were carried out in July 2002 over South Florida. The dataset acquired (courtesy of Gerry Heymsfield, NASA-Goddard) consisted of 2 days of measurements (from 23 and 27 July); with 738 vertical data points in each profile and with 2476 vertical profiles of the atmosphere for 23rd July and 1500 profiles for 27th July. The horizontal (vertical) resolution of the data was 37 m (100 m). The first of the overpasses of the ER-2 aircraft from 23rd July is shown in Fig. 4.1 as the thick gray dashed line in system C and G boxes. The black solid and dashed line in system C is the overpass of WB-57F aircraft measuring microphysical properties of the clouds. The first overpasses of the aircraft are over-plotted on the figure of reflectivity obtained from ground-based radar in NEXRAD net. Fig. 4.1 a) displays the radar reflectivity recorded at 2 km height showing the location of active convective cells and Fig. 4.1 b) at 8 km height showing occurrence of thick anvil clouds.

As can be seen from boxes C and D (at 2 km) the systems are in the decaying stage with extensive expanding anvil clouds tops (at 8 km). The reflectivity structure in systems G and H suggest intensification of deep convection with maximum reflectivity values of 50 dBZ at 2 km height and nearly 40 dBZ at 8 km. Heymsfield et al. [2010] suggested that deep convection can be defined by two criterions: 1) a strong updraught (>10 m/s) over at least a kilometer along the flight track; 2) a strong reflectivity echo extending up to 12-km altitude or greater. The rationale behind that is that convection often evolves where updraughts are the strongest and reflectivities the weakest (early to mature stage) or where reflectivities and downdraughts are the strongest (mature and dissipating periods) which makes it difficult to use just one parameter (reflectivity or velocity) to fully characterise the convection stage.

4.1.2 Specifications of the ER-2 Radars

The ER-2 aircraft remote sensing instruments included two nadir viewing airborne radars - the 9.6 GHz ER-2 Doppler Radar (EDOP) and the 94 GHz Cloud Radar System (CRS) (Heymsfield et al. [2003]). The key parameters of ER-2 radars are listed in Table 4.1. Processed reflectivities and Doppler velocities are obtained every 0.5 s, which corresponds to approximately 100 m of aircraft translation (aircraft ground speed is 200 - 210 ms^{-1}). The footprint of the nadir beam is 1.1 km (0.55 km) at the surface (10-km altitude), so the effective resolution is approximately a few hundred meters at 10-km altitude and 0.5 km near the surface.

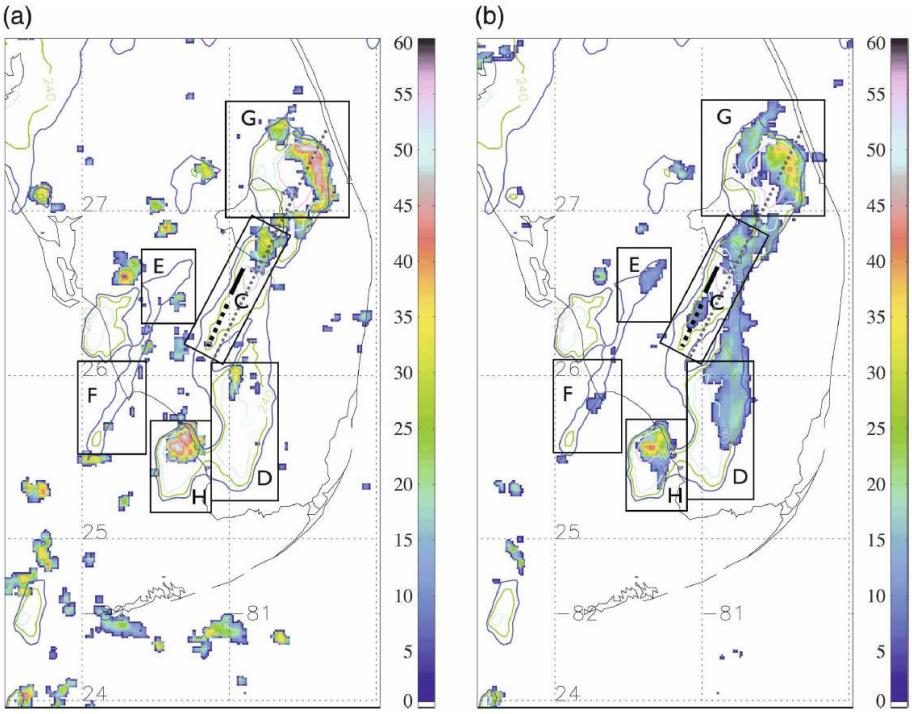

Figure 4.1: NEXRAD composite radar reflectivity image at 2000UTC for a) 2 and b) 8 km height. The colour scale is radar reflectivity (0-60 dBZ). Thick black solid and dashed lines in system C are the WB-57F flight tracks at 13.7 altitude. The thick gray dashed line in system C and G boxes is the ER-2 flight path.

Table 4.1: ER-2 EDOP and CRS airborne radar parameters.

	EDOP	CRS
Frequency [GHz]	9.6	94
Antenna aperture [m]	0.76	0.3
PRF [kHz]	4.4	0.5 - 42
Beamwidth [deg]	2.9	0.6 x 0.8
Pulse width [us]	0.25, 0.5, 1.0	0.25 - 3.0

The Doppler velocities with aircraft motion removed are vertical hydrometeor motions (v_h) from which the vertical air motion $w = v_h + v_t$ can be obtained with a hydrometeor fall speed (v_f) assumption based on the reflectivity.

To obtain reliable data from airborne radars careful calibration must be performed and aircraft motion must be subtracted from the data along with corrections of the antenna tilt angle. Both radars have been previously carefully calibrated (Li et al. [2004]). The CRS radar has been calibrated using a corner reflector mounted on a zenith-pointing pole tower and then intercompared with the University of Massachusetts CPRS 95-GHz cloud radar (Sekelsky and McIntosh [1996]). The EDOP has been calibrated from intercomparisons with the TRMM precipitation radar and analysis of the ocean surface return (Heymsfield et al. [1996]).

Noise averaging and noise substraction is necessary to detect weak cloud signals. The minimum detectable signal (MDS) at 10 km range during CRYSTAL-FACE was -29 dBZ (150-m range resolution, 1-s time average) for CRS. The MDS for EDOP radar was reported as -5 dBZ at 10 km range. Based on this information the MDS function was calculated. To avoid a leakage of noise features causing fake

large reflectivity gradients the threshold value MDS increased by 3 dB is applied to the data. This is further explained in Fig. 4.2 showing the frequency distribution of the CRS radar reflectivity as a function of height - CFAD (Cumulative Frequency Altitude Display). The CFAD is a convenient way to present the probability distribution of a large set of profiles of reflectivity. The red line plotted over CFAD figure is the calculated MDS and the green line is the applied threshold (i.e. MDS increased by 3 dB).

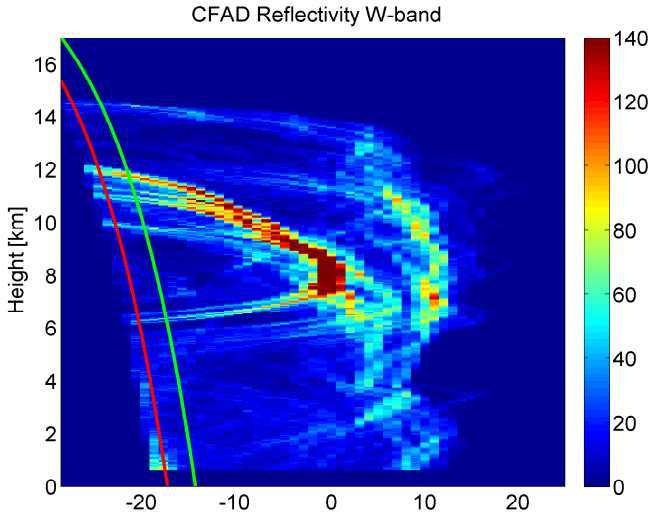

Figure 4.2: ER-2 W-band radar reflectivity CFAD (Cumulative Frequency Altitude Display) with minimum detectable signal (MDS) curve (red) and MDS+3 dBZ threshold (green curve). The MDS + 3dBZ threshold removes all not physical fields of high gradients, caused by continuity issues with the data (i.e. on edges of the scenario). Colourbar represents increase in frequency of occurrence.

4.1.3 Recorded Reflectivity During ER-2 Aircraft Flights

The ER-2 Radars provide reflectivity and mean Doppler velocities at X and W-band. From Fig. 4.3, showing the time-height reflectivity structure, it is evident

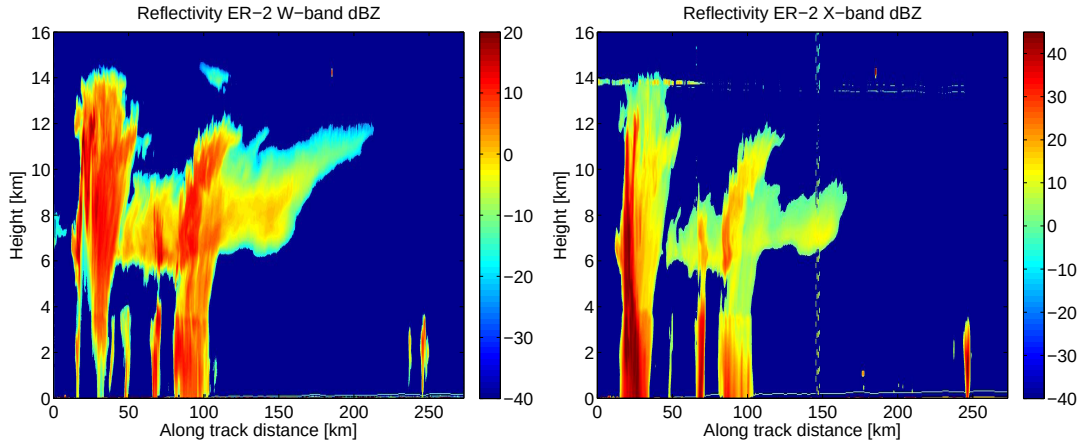

(a) ER-2 reflectivity for W-band

(b) ER-2 reflectivity for X-band

Figure 4.3: Radar reflectivity plots for the ER-2 aircraft radars, colourbar shows the amplitude of reflectivity in dBZ.

that both radars detect the thunderstorm cores (tall convective towers) and anvil. The figures depict the convective region and the extended cirrus anvil trailing off from these convective cells, consistent with upper-level winds. The CRS W-band is more sensitive than EDOP X-band for cirrus, detects the elevated thin cirrus layers above the anvil (i.e. the cirrus cloud at 110 km distance) as well as clouds at 200 km distance. The X-band, on the other hand is considerably less attenuated in convective regions. This is evident in the first core visible at 25 km distance in Fig. 4.3 where the 94 GHz radar is fully attenuated close to the surface. The signal becomes highly attenuated in convection as a result of a mixed phase and because of the likely presence of large and dense ice particles. This results in significantly lower reflectivities at CRS's 94 GHz as compared to EDOP's 9.6 GHz measurements.

4.1.4 Mean Doppler Velocity for July 23rd Case

Both CRS and EDOP Doppler velocity measurements are presented in Fig. 4.4. Several interesting features can be noted. Two convective cells are visible, one in a decaying stage (located at 90 km) and one active convective cell (located at 20 km). As noted in Rickenbach et al. [2008] strong updraughts were ejecting condensate into upper-level sheared flow that fed the growth of anvil clouds over the next few hours. The updraught velocities in the cells exceeded 10 m/s and extended up to 14 km altitude. Both radars show comparable hydrometeor fall velocities for anvil clouds of about 1 m/s and similar rain drop fall velocities of about 5 m/s. While both radar wavelengths can penetrate the decaying system down to the surface, only EDOP can fully probe the active convective cell. The 94 GHz radar is fully attenuated there, so much that even the strong surface return is not present. It is also clear that 94 GHz radar can detect reliably only the upper part of the convective tower. This is further illustrated in Fig. 4.5 which displays a zoom of the area of the active convective cell. Only approximately the first 3 km are properly probed for the strongest convective profiles by the W-band radar and the bottom part of the convective cell is corrupted by combined effects of attenuation and multiple scattering. Below the surface the X-band mirror image can be seen, described in detail in Battaglia et al. [2010] and one of the classic examples of multiple scattering effects. Nevertheless the general structure of the systems has been well depicted by both radars. The EDOP radar missed the light rain event at 37 km. Also the cirrus clouds at 120 km distance and

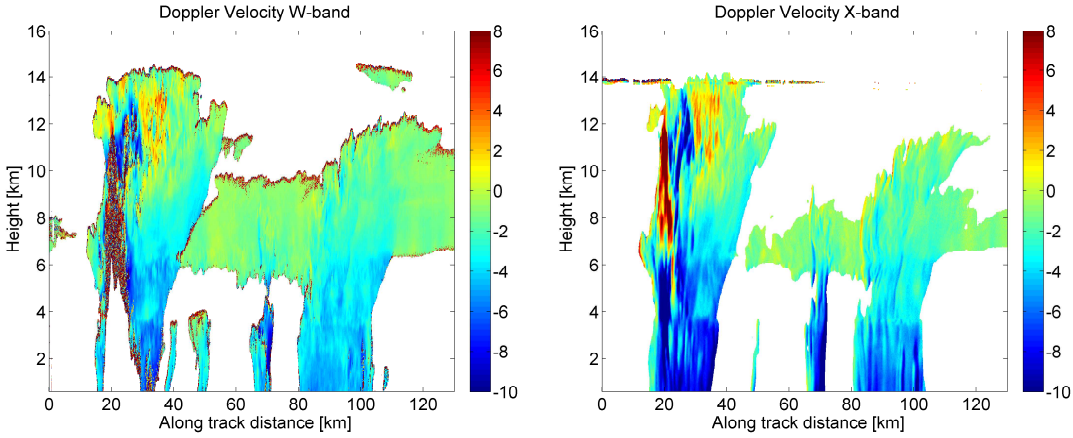

(a) W-band (b) X-band

Figure 4.4: ER-2 aircraft mean Doppler velocity for both radars. One active convective core and one core in decaying stage can be seen on both plots.

the anvil clouds seem better represented in the W-band data.

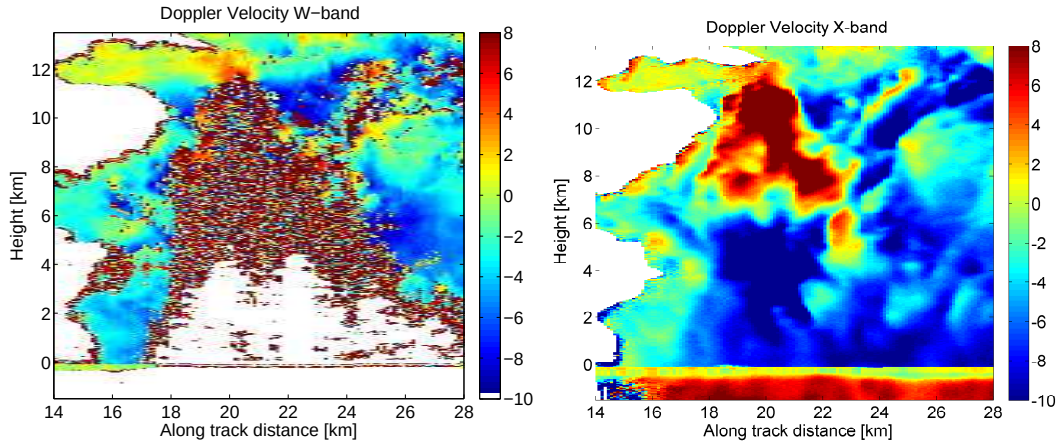

Figure 4.5: Zoomed region of the active convective core from ER-2 aircraft mean Doppler Velocity for W-band (left panel) and X-band (right panel).

4.1.5 Gradients of Reflectivity and Velocity

One of the most important aims of the airborne data study was to determine what values of along-track and vertical gradients can be expected for both reflectivity and

Doppler velocity and how they vary from 9.6 to 94 GHz radars.

The gradients calculated for the W-band reflectivity and for the discussed zoomed area for the X-band including the active convective cell are shown in Fig. 4.6. The gradients larger than 20 dB/km are recorded by both radars. Occasionally, these high gradients can pose a significant difficulty for the Non-Uniform Beam Filling (NUBF) corrections for a spaceborne Doppler radar, where the linear relation between reflectivity gradients is used to correct velocity biases (see Chapter 6).

A normalised probability density function (PDF) has been calculated for along-track reflectivity gradients for the dataset recorded on 23rd July and is displayed in Fig. 4.7*a*). The results reveal that the normalised PDF of the radar along-track reflectivities agree very well with both frequencies, and most data occur in a [-8 to 8] dBZ/km interval with some sections where gradients exceed 20 dB/km. PDFs of Doppler velocity is depicted in Fig. 4.7*b*) and indicates fairly good agreement between both radars with more pixels having large negative values recorded by X-band radar.

A similar pattern is shown by horizonal and vertical velocity gradients. For most data points of along-track (horizontal) velocity gradients (Fig. 4.7*c*)) fit into -7 to 7 m/s/km interval, with the X-band data having a wider PDF (most data fits into -10 to 10 m/s/km). Note, that the most common value for the W-band horizontal velocity gradient (blue curve) has approximately 10000 occurrences. The PDFs of vertical gradients of Doppler velocities display even stronger gradients than in hor-

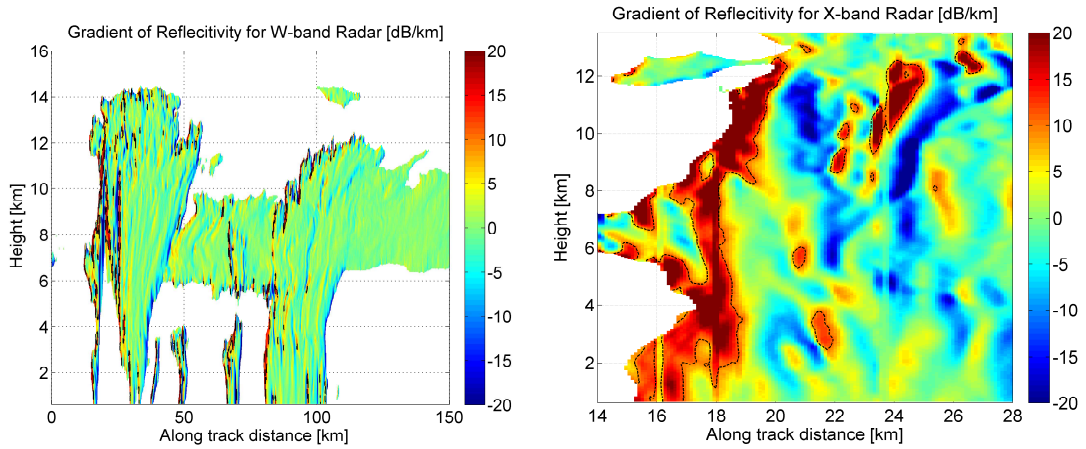

Figure 4.6: Reflectivity gradients for the W-band (left panel) and zoomed area of active convective core for the X-band.

izontal, as well as skewness towards positive gradients. Most data appear in the -11 to 14 m/s/km interval for X-band vertical velocity gradients. Such large gradients in the vertical direction prevent the use of near-neighbour de-aliasing (NNDA) technique as there is too much variability and we cannot expect continuity in either vertical or horizontal directions (Sy et al. [2013]).

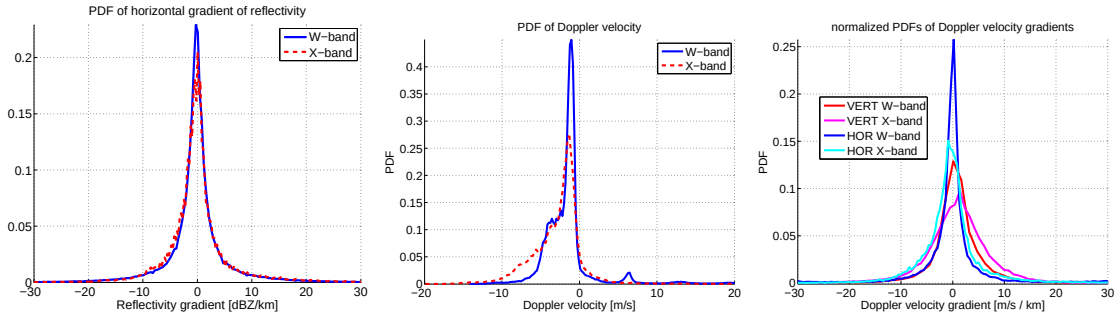

Figure 4.7: Left: plots of probability density function (PDF) for horizontal gradients of reflectivity. The both products are marked with different colours, shown in the legend. Middle panel: PDF of Doppler velocity. Right: PDFs of along-track and horizontal Doppler velocity gradients for the X-band and the W-band.

As the aliasing of Doppler velocities in spaceborne Doppler radar configurations

is believed to be a significant detrimental effect for the overall accuracy, a method to properly de-alias velocity fields has been searched for. One of the possible techniques could be to find a method that would correlate velocity fields to any other available radar products, such as reflectivities or their gradients. If such relation existed this could lay the foundation for a de-aliasing technique. However, no such clear correlation has been found in airborne data when comparing various configurations of reflectivity, Doppler velocity and its horizontal or vertical gradients in both X and W-band. An example of scatterplot of reflectivity and Doppler velocity fields is shown on the left panel of Fig. 4.8. The right panel of Fig. 4.8 displays the scatterplot of along-track gradients of reflectivity and Doppler velocities.

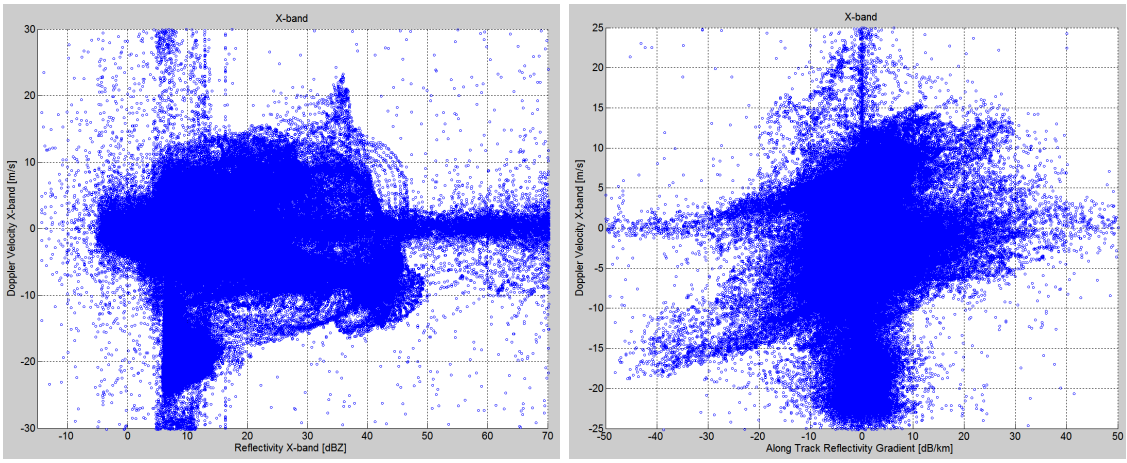

Figure 4.8: Left panel: an example scatterplot between radar reflectivity and mean Doppler velocity for X-band radar, showing no evidence of correlation between those two products. Right: Scatterplot between along-track gradients of reflectivity and mean Doppler velocity for X-band radar.

4.2 Characterization of Reflectivity and Doppler Velocity Gradients in Convection

4.2.1 Cumulative Distribution Functions

The cumulative distribution function (CDF) has been calculated for profiles classified as convective (Fig. 4.9). Profiles which contained regions of absolute velocities larger than 1.5 m/s above the freezing level (which was about 3.6 km altitude) were classified as convective. Note, that the x-axis units are different for various CDFs. The CDF function reveals that about 5% of the pixels exceed a mean Doppler velocity of 10 m/s recorded by both EDOP and CRS radars. It is also evident that there are significant mean Doppler velocity gradients in the convective regions. It is shown for the X-band radar as the data were not as much affected by attenuation effects in the most interesting part and it reveals that 4% of all cases of horizontal and vertical velocity gradients exceed values of 15 m s^{-1} km^{-1} with values as high as 25 m s^{-1} km^{-1}. The largest values are likely to be a significant problem for spaceborne Doppler radars with relatively small antennas. Another important result (used to assess spaceborne configuration) revealed by CDF is that 13% cases exceed along-track reflectivity gradients of 10 dBZ/km and about 3 % are as high as 20 dBZ/km with some pixels even exceeding 30 dBZ/km. The along-track reflectivity gradients correlate very well with both radar frequencies.

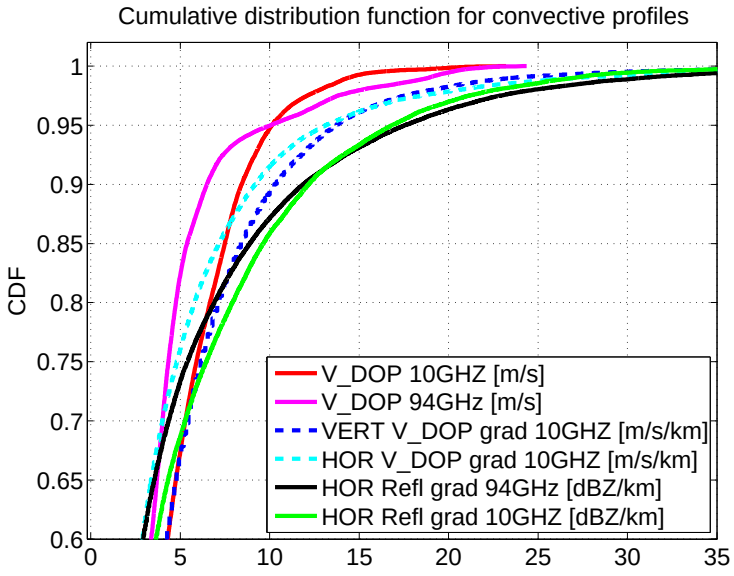

Figure 4.9: Cumulative distribution function (CDF) plots for convective profiles. The red curve depicts the CDF of mean Doppler velocity of the X-band radar, while the pink of the W-band. The CDF of vertical gradients of mean Doppler velocity for the X-band is marked in the blue, while the horizontal gradients are marked in the cyan. The horizontal reflectivity gradients for the W-band radar are marked in the black, while for the X-band in the green, respectively.

4.3 Conclusions

Aircraft play a crucial role to characterise cloud systems. They enable in situ measurements which provide valuable insights into the physical processes occurring in the clouds and are vital to validate remote retrieval techniques. From the limited dataset discussed in this chapter several conclusions can be drawn. While most updraughts and downdraughts occur in [-15 to 15] m/s interval (more than 90%) velocities of up to 25 m/s can be encountered in convective systems. Tall convective systems reaching 14 km altitude are commonly seen.

Both airborne Doppler radars (CRS - 94 GHz and EDOP 9.6 GHz) were able

to penetrate through a thick cloud and a light rain layer to detect the surface. The EDOP precipitation radar can penetrate the most intense thunderstorms without being completely attenuated down to the surface but is generally not as sensitive to clouds as 94 GHz CRS radar. However, the 94 GHz radar is strongly attenuated with Doppler profiling capabilities limited only to the upper part of active deep convection cores.

The airborne data indicate that there are very large along-track gradients of the reflectivity. Gradients larger than 25 dBZ/km are seen in convective areas, though they constitute less than 3% of cases for both radar frequencies. This can be a challenge for the NUBF correction (see Sect. 6.5.1) which is based on along-track reflectivity gradients. Especially in regions where high amplitude gradients of the opposite sign are next to each other, as sometimes happens for low SNR regions (i.e. edges of clouds). A proper choice of SNR threshold is essential. Another finding is that the along-track gradients are comparable for 94 GHz and 9.6 GHz radars, even if the scattering and attenuation at these frequencies is governed by different processes.

Advancing the discussion of possible de-aliasing techniques for velocity folding from Chapter 6 it has been concluded that no clear correlation can be found between Doppler velocity fields (or its gradients) and reflectivity fields or its vertical and horizontal gradients for both radar frequencies.

The 94 GHz radar can detect most ice clouds and light rain through the tropo-

sphere and the lower stratosphere. For cirrus cloud detection, the airborne or space-borne 94 GHz radar has several unique advantages over the ground-based radars. One of them is its operation in a downward-looking mode from a high-altitude platform. Such measurements are less affected by the water vapour and oxygen absorption, most of which are present at low altitudes. As sensitivity decreases with increasing range from the radar, operating onboard aircraft enables high-altitude cirrus clouds measurements at a closer range than ground-based radars. A Radar such as CRS is able to use the ocean surface as a calibration reference to check system performance as well as to estimate the total path attenuation, valuable for understanding the physics of W-band measurements and for cloud microphysical properties and rain-rate retrievals. These considerations demonstrate that a W-band cloud radar can fill the gap between a lidar and precipitation radar, while the overlap between the measurements can potentially be useful in multi-wavelength microphysics retrievals.

Chapter 5

End to End Doppler Radar Simulator

5.1 Structure of the Simulator

Until the launch of EarthCARE in 2016, notional studies are the only means of assessing the impact on the accuracy of the Doppler products of EarthCARE's configuration. In the thesis the end-to-end Doppler radar simulator is used; the simulator consists of three main sections:

I –> Forward Monte Carlo Modelling,

II –> Radar Instrument Model,

III –> Corrections Module.

The forward model has been developed over the last decade under the leadership of Dr A. Battaglia with the core structure developed in 2005 (detailed description in Battaglia et al. [2006]; Battaglia and Mantovani [2005]) and then successively upgraded to account for multiple scattering within the ESA-DAME (Doppler Air Motion Estimate) project (Battaglia and Tanelli [2011]).

The Instrument Model (Signal Processing unit) has been developed based on a theory developed in the 70's (Benham et al. [1972]; Hildebrand and Sekhon [1974]; Sirmans and Bumgarner [1975]; Zrnic' [1975]) and tailored and upgraded for the EarthCARE radar concept. This work has been done at University of Leicester with valuable inputs from Prof. Pavlos Kollias from McGill University and Dr Simone Tanelli from Jet Propulsion Laboratory at NASA. The instrument model derives signal fluctuations as measured at the radar antenna port (i.e. the in-phase and quadrature sample time series) as in Tanelli et al. [2002b] from the idealized forward model output, including signal fluctuation and thermal noise. From these, the estimates of the Doppler moments via the autocorrelation pulse pair technique are derived. The model has also been upgraded to account for polarization diversity scheme and the polarization diversity pulse-pair method is implemented (Battaglia et al. [2013]).

The third part of the radar is the correction module which makes use of different available Doppler spectra as simulated by the forward modelling to separate a variety of errors affecting the spaceborne radar measurements with the goal of mitigating

some of these errors. Within the simulation framework all error sources can be isolated (e.g. by simulating spectra with no satellite motion, no multiple scattering, no aliasing,...). The schematic cartoon of the end-to-end Doppler radar simulator is displayed in Fig 5.1.

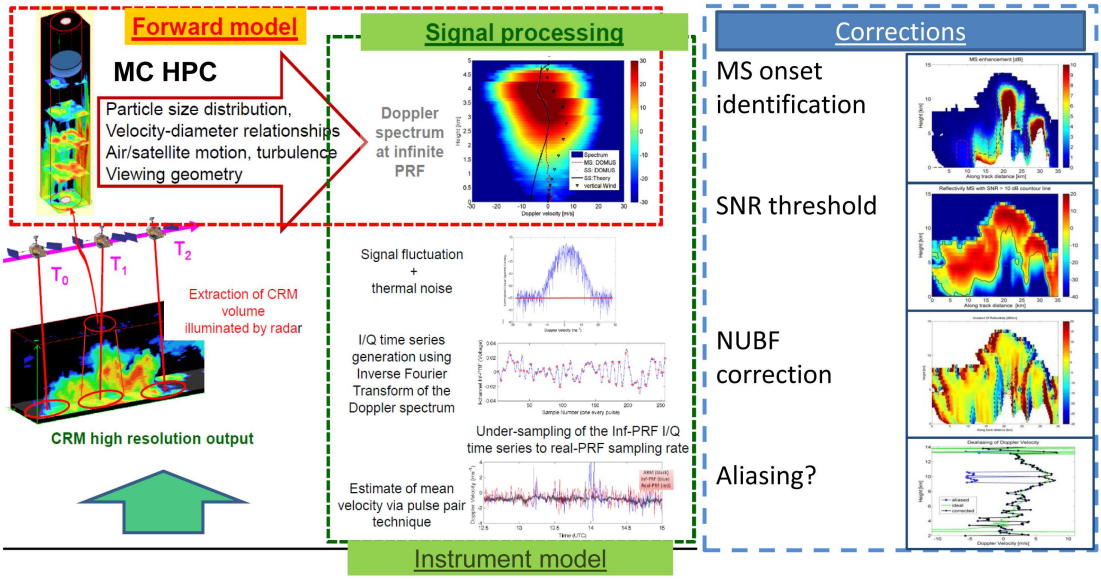

Figure 5.1: Radar simulator schematic cartoon showing a complete end-to-end radar simulator, including forward modelling, instrument model and corrections module. In each part of those three sections, typical operations performed there are depicted.

5.2 Forward Monte Carlo Computations

5.2.1 Weather Research and Forecasting Model Input

The Weather Research and Forecasting Model (WRF), a high-resolution Cloud Resolving Model, is used as an input to the end-to-end radar simulator. The WRF is a

numerical weather prediction system designed to serve both operational forecasting and atmospheric research needs (Skamarock et al. [2005]). To understand physical processes with a very strong relation to convection, the fine resolution is needed so that the simulated process is fully resolved. For example Goldhirsh and Musiani [1986a] found the median convective cell size for convective storms off Virginia coast is only 1.9 km. To resolve such fine-scale phenomenon high resolution modelling is required. Thus, the end-to-end simulator is applied to convective scenarios, produced by a 0.33 km horizontal resolution WRF simulation. The WRF model data were simulated based on the convective scenarios observed during the Tropical Composition, Cloud and Climate Coupling Experiment (TC4) performed in July 2007 in the East Pacific tropical ocean, 400 km from the coast of Costa Rica (Parodi and Tanelli [2010]). The choice of those CRM as a source of data input was based on several characteristics. During the TC4 campaign a large number of convective cells were triggered and evolved within a domain of manageable size (i.e., few hundred square km), numerous is situ and remote sensing observations were available from airborne and spaceborne instruments at the time of the campaign. This allowed to assess and compare the simulated CRM model outputs with the in situ measurements. Parodi and Tanelli [2010] used available TC4 data to simulate the convective scenarios in resolutions of 9, 3, 1 and 0.33 km. From these the finest horizontal resolution was chosen based on the recommendation of Craig and Dörnbrack [2008] for the numerical simulations in cumulus clouds. The end-to-end radar simulator

uses all hydrometeor profiles (rain water content, snow water content, graupel water content, cloud water content, cloud ice content in g/m^3) along with vertical profiles of temperature, humidity, atmospheric pressure, and wind vectors as input.

Possible overpasses of the radar are shown in Fig. 5.2. The 3D WRF model precipitating hydrometeors content in $[g/m^3]$ integrated for all vertical layers is used as the background. The radar tracks are marked as yellow rectangles with red border. The radar simulator calculates the scattering properties for a sufficient number of cross-track grid pixels around the overpass to account for a large footprint of radar configuration and a scattering volume of radiation undergoing multiple scattering, which is marked as the green-shaded area in Fig. 5.2.

5.2.2 Forward Monte Carlo Modeling

Within the preparatory studies related to the EarthCARE mission, a radar model capable of simulating the Doppler spectrum in the presence of multiple scattering has been developed. This model simulates the measurements of an active instrument onboard a satellite as an idealized spectrum without signal fluctuations; the forward model output is then coupled with the instrument model to estimate the Doppler moments for specific radar configurations.

The forward MC simulation has an advantage of a complete polarimetric treatment of radar variables; of including 3D effects and arbitrary antenna patterns. In fact to properly account for antenna pattern related effects (e.g. NUBF) it is manda-

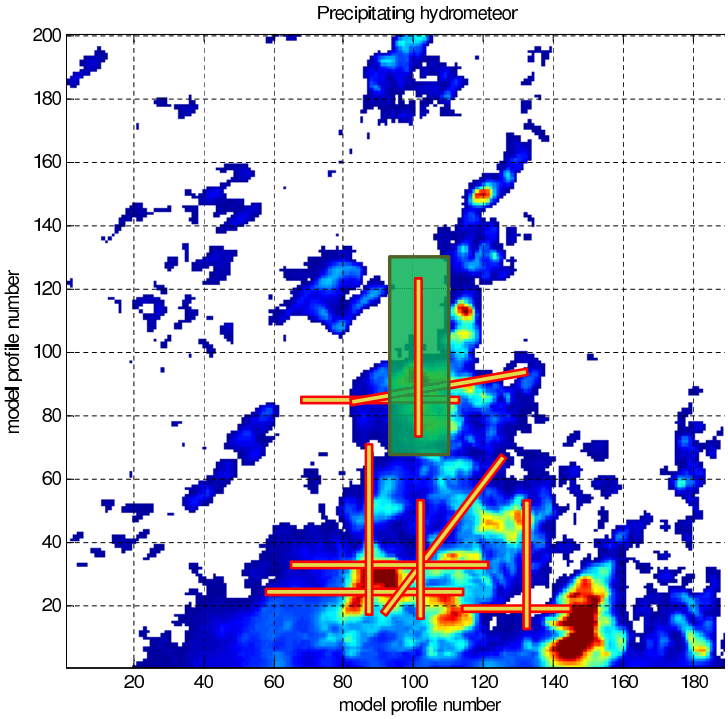

Figure 5.2: WRF model precipitating hydrometeors content in $[g/m^3]$ integrated for all vertical layers with a sample radar overpasses marked in orange. The WRF model has a resolution of 0.33 km and consists of roughly 200 profiles in each direction. The green-shaded area corresponds to the volume from which the scattering data are supplied to the radar simulator.

tory to use full 3D approach. One-dimensional simulators are often not capable of a proper simulation of Doppler radar spectra. As a result, it is not possible to simplify the problem to a 1D approximation.

On the other hand, the Monte Carlo scheme offers the opportunity of performing Doppler radar spectra simulations accounting for multiple scattering effects, polarization effects (e.g. computation of LDR) and detailed surface interaction (specifically including the mirror image and higher order of scattering terms). However,

it is much more computationally expensive than the SS models used by Schutgens [2008] and Tanelli et al. [2002a].

The simulator has been designed with a freedom of options. Circular and elliptical antenna patterns have been implemented. The transmitter can be set to emit signals in vertical, horizontal or circular polarization. For polarization diversity system the receiver can record co-polarized and cross-polarized radar returns from which the horizontally and vertically polarized signals are derived. The range resolution of the radar is simply characterised by the pulse duration.

The radar outgoing radiation is simulated by a number of radiation trajectories, whose number is high enough to represent the stochastic variability of all processes involved in radiation propagation and interactions when released from the transmitting radar antenna with an appropriate polarization state. All radiance field properties can be computed from statistical properties of the photon density.

Once the "photon" is emitted from the radar it undergoes scattering or absorbtion precesses as it travels through the atmosphere and is finally received back by the radar receiver. Each photon is traced as it travels through the medium and stochastic processes such as: distance to collision, probability of scattering, direction of scattered photons etc. are simulated. Biasing techniques are applied to prevent the photons from escaping from the medium and to avoid absorption events (section 5.2 in Battaglia and Mantovani [2005]).

The forward model computes the radar signal return including all scattering

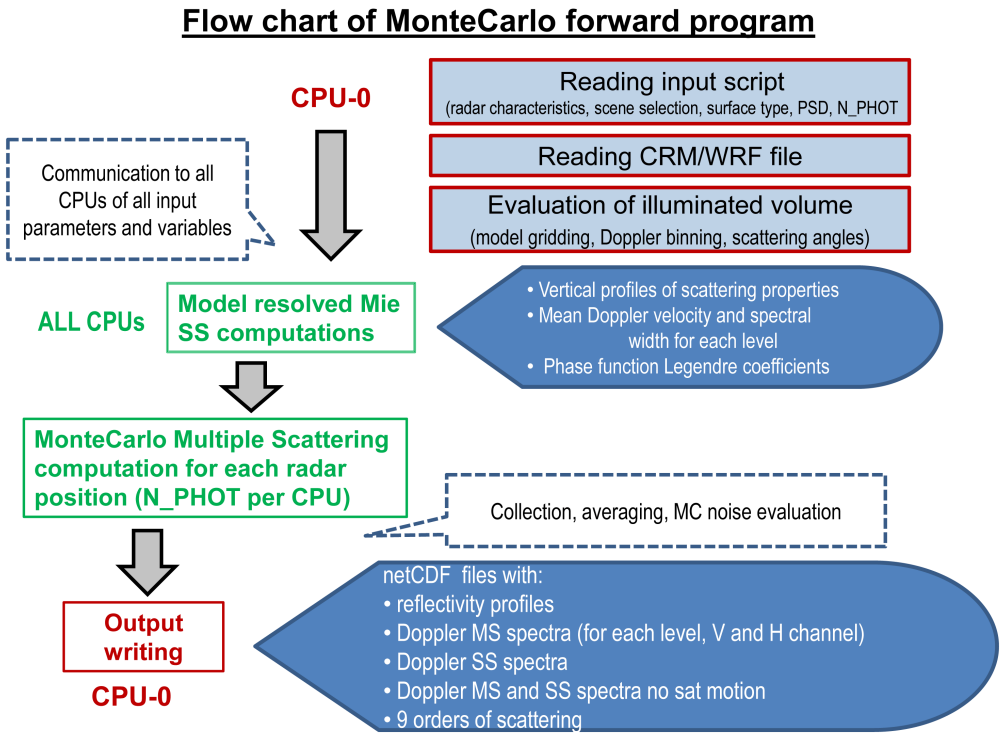

Figure 5.3: Flow chart of the forward Monte Carlo radar simulator, displaying the main stages of calculations.

order contributions - idealized radar Doppler spectra (sampled at very high PRF) as measured by a spaceborne radar flying over 3D highly resolved scenes. In this context, "ideal" means that no Doppler aliasing, receiver noise or second trip echoes are included.

In practice, due to a large number of generated photons to achieve satisfactory stochastic accuracy the forward model was run at University of Leicester High Performance Computing ALICE Cluster. The flow chart of the forward model is shown in Fig 5.3. To reduce time of simulation the model supports parallel calculations on cluster CPU nodes (parallel calculations shown in green) which are then collected,

averaged and outputted as netCDF files.

5.2.3 Forward Model Output

The primary radar forward model output is the Doppler spectrum, S_V, of the returned radar signal at the receiver antenna port which is provided for four dimensions (number of vertical profiles, number of range gates, polarization channel, number of points in the recorded Doppler spectrum). The output Doppler spectra result from the combined effect of the satellite velocity, the hydrometeor fall velocity and wind speeds in the volume under observation while accounting for the radar viewing geometry and the antenna pattern.

The spatial scales covered by the simulator are limited by the memory requirements on HPC cluster and the computing time necessary. Horizontal and vertical resolution of the input scenario can vary but the scene containing 200 over 200 profiles spaced 0.33 km apart were successfully used as input. The simulated radar track can contain up to 150 profiles spaced by 500 m with 100 m vertical sampling.

The velocity spectrum is provided at a sampling rate several times higher (e.g. factor U = 5) than the actual sampling rate (governed by PRF) of the spaceborne radar. This enables the creation of high PRF products not affected by the Nyquist velocity folding. To separate other sources of error the forward model allows to simulate spectra accounting for all orders of scattering (MS) or with the single scattering (SS) approximation, with or without satellite platform movement or spectra

without attenuation or ignoring velocity of hydrometeors, as detailed:

- Scattering approximation:
  - Multiple Scattering ${}^{MS}(S_V)$; Single Scattering ${}^{SS}(S_V)$
- Satellite velocity:
  - included $(S_V)^{mov.}$; no satellite velocity $(S_V)^{stat.}$
- Spectrum: no attenuation included; no hydrometeor velocity

Fig 5.4 displays example Doppler spectra for specific vertical profile and at 10 km height, computed by the forward model.

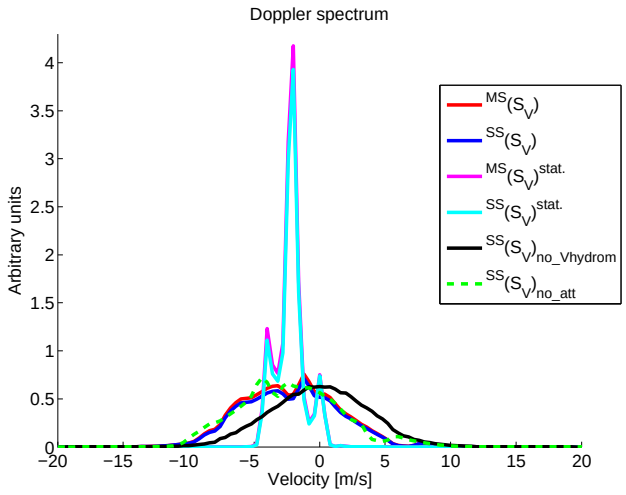

Figure 5.4: An example of Doppler spectra as computed by forward model, computed at 10 km height. The different radar spectra are summarised in the legend, specifically including or excluding multiple scattering, accounting for satellite motion, assuming no attenuation etc.

5.3 Instrument Model - Signal Processing

The generation of synthetic Doppler velocity measurements from forward model output is described in this section.

The signal processing model also known as the radar instrument model generates I and Q voltage time series from a series of Doppler spectra. I and Q are then used to produce the estimates of Doppler moments (radar received power, mean Doppler velocity and spectrum width). The generation of the Doppler spectra is based on the assumption of stationarity of the observed scene for very small along-track radar displacements (Kollias [2010]).

The need for two receiver channels (I and Q) arises from the need to measure Doppler information. A single coherent receiver can reveal the speed of a target but it cannot tell whether it is moving towards or away from the radar. A second receiving channel is employed to resolve the ambiguity by shifting a signal 90° in phase from the first channel (Kingsley and Quegan [1992]). These are known as I and Q channels which stand for In-phase and Quadrature.

The I and Q voltage time series are processed to estimate the first three moments of the power spectrum - namely the radar total received power (zeroth moment), the mean Doppler velocity (first moment) and the Doppler spectrum width (second moment). The most widely used methods to date are: 1) the autocovariance analysis by means of the pulse pair (PP) processing technique (Zrnic [1977]), and 2) the spectral analysis by means of the discrete Fourier transform (DFT) Zrnic' [1979].

The PP technique is the most computationally efficient, relatively robust in dealing with white noise, and it is almost optimal for narrow (small spectrum width) and symmetric spectra. The DFT technique, in general, has comparable estimation performance to PP, it is less sensitive to spectral broadening, and provides detailed information of the entire spectrum. However, it is more computationally intensive. For the estimation of power moments the EarthCARE CPR will use the pulse pair technique due to its simpler complexity of signal processing and because of the method′s higher potential than DFT for signals with SNR < 0 dB, often encountered when dealing with space observations (Kobayashi et al. [2003]).

The following instrument model is described using the EarthCARE Doppler Radar parameters. Input parameters for building the radar instrument model are provided by the radar characteristics table as primary source of information. Such table for EarthCARE is displayed in Table 3.1.

The output of the forward model needs to be interpolated from the simulated number of velocity samples to the number of samples that corresponds to the EarthCARE sampling points (a function of the PRF). According to the EarthCARE specifications the radar sends 22 pulses followed by 2 'empty' pulses to measure background noise. Then the level of background noise is subtracted from the received signal. This approach allows to measure signals even 15 dB below the noise floor, depending on the integration length.

In radar system aliasing of velocities, which is an effect causing different signals to

become indistinguishable when sampled, can occur. The sampling rate at which the signal is aliased is called Nyquist frequency $f_N = PRF/2$ which is half the sampling frequency (PRF) of a discrete signal processing system. It is sometimes known as the folding frequency of a sampling system. Using the radar wavelength (λ) the folding frequency can be converted into a Nyquist velocity (or folding velocity v_N = PRF / 4). The approach chosen here is to keep both an authentic EarthCARE signal (usually with underscript $_{EC}$) and the not aliased observables, sampled with much higher PRF. The output of the forward model is provided at a high sampling rate, which is then undersampled to achieve authentic EC sampling rate. This helps to quantify the effects of the aliasing and evaluate different radar parameter configurations. The high PRF observables are usually labeled with an underscript $_{INF}$ from infinite, as observables sampled with high enough PRF are not affected by aliasing effects.

5.3.1 Signals at Radar Antenna Port

Common gaussian model of the mean received power spectral density from a meteorological signal is depicted in Fig. 5.6 and can be interpreted as the integral under the curve (or zeroth moment) which is given by

$$\langle P \rangle = \int S(f)df = \int S(v)dv \tag{5.1}$$

where f and v are related by $f = (2v/\lambda)$. The mean velocity ($\langle V_D \rangle$) is given by the first moment of the spectrum:

$$\langle V_D \rangle = \frac{\int vS(v)dv}{\int S(v)dv} \tag{5.2}$$

The expression gives a mean Doppler velocity where each measured velocity is weighted according to the quantity of power backscattered by hydrometeors moving at that velocity. The spectrum width ($\langle \sigma_D \rangle$) is given by taking the square root of the second central moment:

$$\langle \sigma_D^2 \rangle = \frac{\int (v - \langle V_D \rangle)^2 S(v)dv}{\int S(v)dv} \tag{5.3}$$

These first three moments are usually labeled Z, V_D, and W_D.

5.3.2 Range Weighting Function

Due to the long pulse length of spaceborne radars (e.g. in EarthCARE CPR $\tau_p = 3.3$ μ s, thus the range resolution is $\sim$ 500 m) it is desirable to sample the return signal at a higher resolution than is determined by the instrument range resolution. This will help to better determine cloud boundaries and separate the surface contribution from the cloud contribution for low clouds and is known as over-sampling. Thus, Doppler spectra of consecutive range gates (spaced by 100 m in EC configuration) corresponding to the same CPR pulse are correlated. In order to reproduce such

a feature the corresponding radar returns are convoluted in range by weighting function W(r) so the outcome spectra are correlated in height. Convolution of the signal is made to account for the weighting due to the (square of) antenna pattern function. The power range weighting function is given by:

$$W^2(r) = \exp(\frac{-\pi^2(r-r_0)^2}{2\log(2)(c\tau_p/2)^2}) \tag{5.4}$$

where c is speed of light, r denotes range, τ_p is a transmitter pulse width. At this point the idealized forward model Doppler moments are calculated for different forward model spectra - and those Doppler products do not go through the next stages of instrument model. This first group of Doppler products - reflectivity and mean Doppler velocity assigned Z_{forw} and $(V_D)_{forw}$ is termed "idealized" (no aliasing, no radar receiver noise) and are used as reference products when MS and NUBF error sources are discussed.

5.3.3 I and Q Samples Generation

The weather echo and receiver noise have very similar statistical properties (Zrnic' [1975]). This allows to represent the ith sample in-phase I and quadrature phase Q at one range gate as:

$$I(i) = s(i)\cos\phi(i) + n(i)\cos\psi(i) \tag{5.5}$$

$$Q(i) = s(i)\sin\phi(i) + n(i)\sin\psi(i) \tag{5.6}$$

where s(i) is a signal and $\phi(i)$ is a uniformly distributed phase. Similarly n(i) and $\psi(i)$ are defined for radar noise.

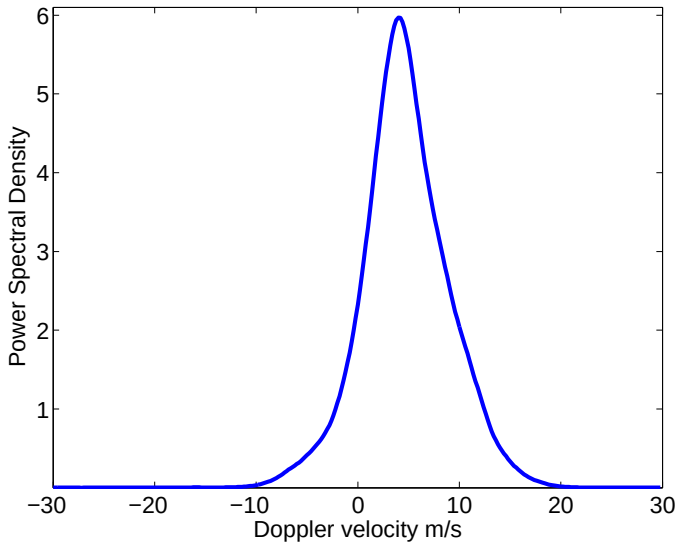

Figure 5.5: An example Doppler spectrum recorded at 10 km height from the output of the radar forward model. This sample spectrum is used to calculate other quantities in this chapter.

The total received power together with EC-CPR receiver noise power Z_N are used to add noise in the EC-CPR Doppler spectrum. Noise spectrum is assumed white, assuming homogeneous noise contributions, and the mean noise spectral density P_N is provided by:

$$P_N = \frac{Z_N}{n_{DFT} \cdot dV} \tag{5.7}$$

where dV is velocity resolution and n_{DFT} is the number of spectral densities.

Following the method described in Zrnic' [1975] the spectral power density of

the signal-plus-noise P_{S+N} is given by:

$$P_{S+N} = -(P_S + P_N) \cdot ln[X_k] \tag{5.8}$$

where X_k is a random number uniformly distributed between 0 and 1.

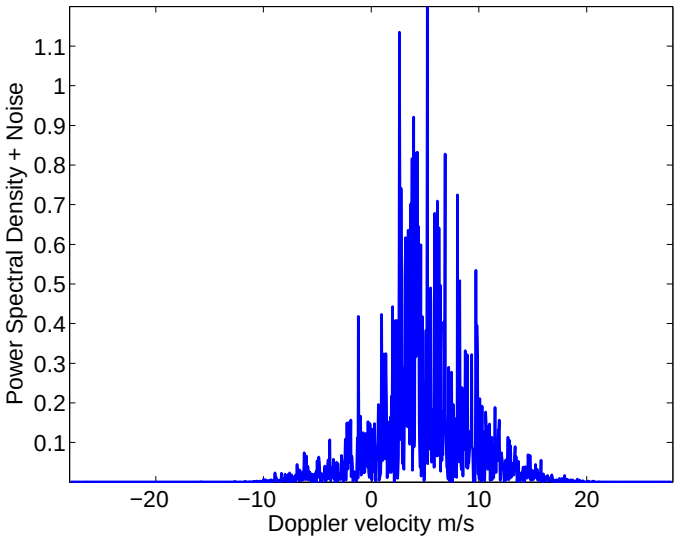

Figure 5.6: An example of Doppler spectrum with added noise, recorded at 10 km height

The CPR sampling volume is then shifted to the next range gate until the vertical stack of CPR Doppler spectra is generated. To generate I and Q voltage time series the Inverse Discrete Fourier Transform (IDFT) is used. An example of I and Q channel time series generated by IDFT are shown in Fig. 5.7.

The simulated Doppler spectrum is sampled by a high PRF rate (U = 5 times larger - INF spectrum). This is done by using very large pulse repetition frequency (thus having large Nyquist velocity). The complex I and Q time series are under-

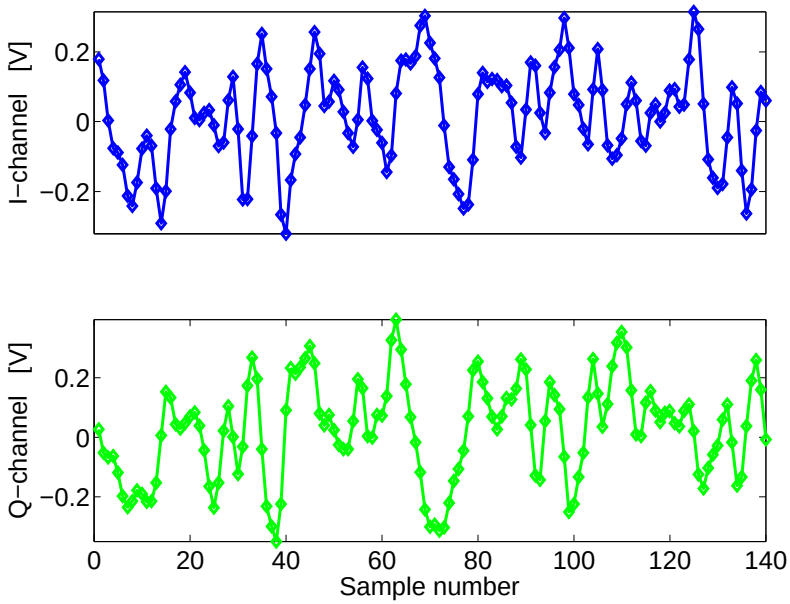

Figure 5.7: The generated I and Q radar time series (for high PRF). For clarity, only 140 first samples are plotted for both channels.

sampled to simulate the real EarthCARE PRF by a factor of U.

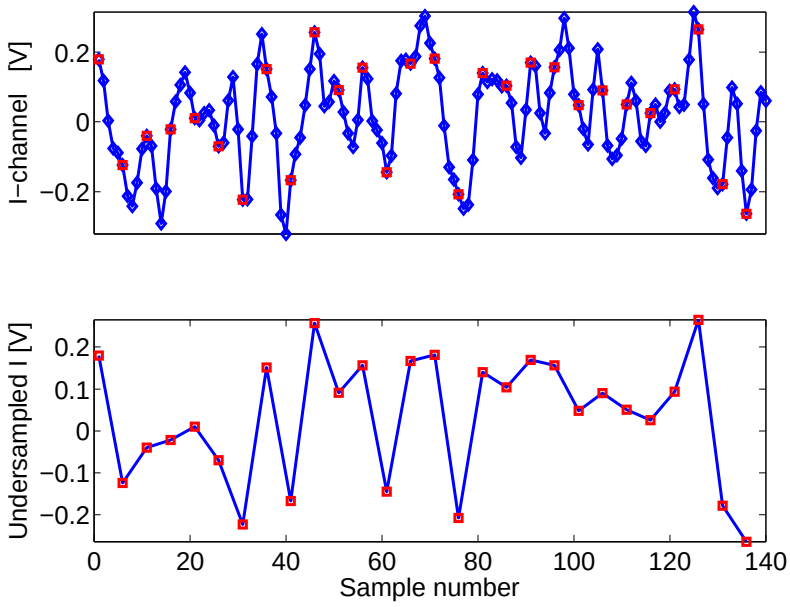

Figure 5.8: The time series in I-channel are shown in the top panel in blue (generated for the high PRF). The high PRF signal in then undersampled for correct PRF of a radar system. The points used for the undersampled signal are marked in red. The signal in I-channel after undersampling is shown in the bottom panel.

5.3.4 Pulse Pair Processing (PP)

Zrnic' [1975] describes a technique of producing synthetic digital weather radar signals from a parameterized doppler spectrum characterizing a specific pulse volume. The thermal noise entering the receiver has a zero-mean gaussian PDF. This is not adequate at the point where the radar moments are calculated, as at that point the noise (and any signal component) has passed through the receiver. Hence, the need to consider the noise and signal-plus-noise distribution at the output of the receiver.

For a general input distribution the calculation of the output PDF can be challenging, the situation for gaussian inputs are remarkably easier, and the inputs from weather signals can be treated as gaussian-like (Doviak and Zrnic [1984]). In fact, gaussian inputs give rise to gaussian outputs. It would be enough to calculate the mean value and standard deviation for output. However, to take into account the effects of filtering a more indirect approach is needed. It involves the examination of the relationship between values of the output separated in time. To achieve this the autocorrelation function is used. The function is assumed to depend only on the separation in time (T_s, also called lag) between the measurements (Kingsley and Quegan [1992]).

Each radar pulse produces a pair of I/Q samples at each range gate. Each I/Q sample includes a contribution from the atmosphere and the receiver noise. A cloud with radar reflectivity of -21.5 dBZ generates a radar return power that is approximately equal to the EC CPR receiver noise (SNR equals 0) for a single

pulse. The longer we dwell the signal, the longer the I/Q time series we record at each range gate.

The produced I/Q time series of the radar echo are then used as input to autocovariance analysis by means of pulse-pair (PP) processing technique for the estimation of the first three radar Doppler moments (radar reflectivity, mean Doppler velocity, Doppler spectrum width). The Pulse Pair technique (PP) uses the time-domain algorithm to estimate the autocovariance function $R(T_s)$ at lag-one, e.g. from pulse to pulse (pulse-pair, T_s = Pulse Repetition Time, 1/PRF) which is given by the equation:

$$\hat{R}(T_s) = \frac{1}{M-1} \sum_{i=1}^{M-1} conj(V(i)) \cdot V(i+1) \tag{5.9}$$

where the radar complex signal is defined as $V(r,t) = I(r,t) + jQ(r,t)$. As denoted in the previous equation, the echo voltage is a function of both range r and time t. Because pulses are transmitted every T_s, echoes from a stationary scatterer will periodically appear at $t = 2r/c + mT_s$, where $m = 1, 2, 3, etc.$ defines each echo pulse. Because the scatterer′s range is not known, a search for echoes is made by circuits that sample, at rates typically $> \tau_p^{-1}$, for echoes and the sampling process is reset every T_s. In this notation τ_p is transmitted pulse width. The T_s interval is defined as $range - time$ $\tau_s (0 \leq \tau_s \leq T_s)$ because the location of the echo within T_s defines the range r to the scatterer. If the scatterer moves, not only will the echo pulse change its location along τ_s but phase Ψ_e will also change due to the fact that $\Psi_e = -\frac{4\pi r}{\lambda} + \Psi$, where Ψ_e denotes echo phase and Ψ sum of the phase shifts within

the radar and the scatterer. Both echo position along τ_s and Ψ_e can in principle be used to measure the change in scatterer location, and thus indirectly its radial velocity. However, Ψ_e change is a more accurate measure of changes in scatterer location. For example, a change of r by $\lambda/4$ (e.g., 2.5 cm for typical weather radar) causes Ψ_e to change by 180°, a large angular change, whereas the change $\delta\tau_s$ along τ_s is $\delta\tau_s = \lambda/2c$ (e.g., 1.67x10^{-10}s) a tiny fraction of τ_p. Thus scatterer motion is measured by changes in Ψ_e. As a consequence, the pulsed-Doppler radar is an amplitude and phase sampling system. Range-time τ_s determines the range to the scatterer, and changes in Ψ_e for echoes sampled at τ_s are measured from pulse-to-pulse along $sample-time\ mT_s$. Because of this sampling process, the sampled echo voltage is written in the following form:

$$V(\tau_s, mT_s) = I(\tau_s, mT_s) + jQ(\tau_s, mT_s) \tag{5.10}$$

where τ_s and mTs determine the range $r = c\tau_s/2$ and sample-time, respectively. This sampled echo voltage can be represented as a vector on the Argand diagram, with $I(\tau_s, mT_s)$ and $Q(\tau_s, mT_s)$ as the coordinates. The carrier-shifted vector has the amplitude $|V(\tau_s, mT_s)|$ and echo phase Ψ_e (positive when measured ccw from the $I(\tau_s, mT_s)$ axis). An example of the $I(\tau_s, mT_s)$ and $Q(\tau_s, mT_s)$ components from a 10-cm wavelength radar illuminating both stationary and moving scatterers are shown in Fig. 5.9 as a function of τ_s for five successive transmitted pulses spaced T_s. Amplitudes can change from a positive maximum to a negative maximum if the

scatterer moves $\lambda/4$ in T_s.

From the autocorrelation function three radar moments can be calculated and are given by the following expressions:

$$\langle Z \rangle = \hat{R}(0) = \frac{1}{M} \sum_{i=1}^{M} |R(0)| = \frac{1}{M} \sum_{i=1}^{M} (I_i^2 + Q_i^2) \tag{5.11}$$

$$\langle V_D \rangle = \frac{\lambda}{4\pi T_s} \arg(\hat{R}(T_s)) \tag{5.12}$$

$$\langle \sigma_D \rangle = \frac{\lambda}{2\sqrt{2\pi T_s}} \left| \ln \frac{\hat{R}(0)}{\hat{R}(T_s)} \right| \tag{5.13}$$

Convenient measure of the spread of the Doppler spectrum is its variance σ_D^2. Typical precipitation distributions produce spectra which approach a Gaussian character, sometimes with deviations with more than one maximum. Nevertheless, the variance is a commonly used indicator of the spread of Doppler spectrum (Battan [1973]).

Over the years the variance of Doppler velocity spectrum $[m^2/s^2]$ has been measured by many researchers with the typical ranges for snow (0.04 - 0.25), melting snow (0.5), rain (0.7-1.0) and hail which is very sensitive to radar wavelength and wetness (8 - for dry, 19 - for wet hail of 2 cm in diameter for wavelength of 3.2 cm) as summarized in Battan [1973].

5.3.5 Doppler Products Available in Simulation Framework

The simulation framework offers a variety of forward model spectra. Among others the spectra can account for SS contributions only or can include all orders of scattering (MS). The satellite velocity can be either included in simulations or set to zero as the satellite was stationary. The list from Sect. 5.2.3 of available Doppler products can be categorised (using a Doppler velocity (V_D) as an example product) according to:

- Spectral assumption:
  - idealized (forward model): $(V_D)_{forw}$; real radar configuration (EC, ACE, CLDY): $(V_D)_{EC}$; high PRF (no aliasing): $(V_D)_{INF}$
- Scattering approximation:
  - Multiple Scattering: ${}^{MS}(V_D)$; Single Scattering: ${}^{SS}(V_D)$
- Satellite velocity assumption:
  - included: $(V_D)^{mov.}$; no satellite velocity: $(V_D)^{stat.}$
- Integration length assumption:
  - 500 m; 1 km; 2 km
- Signal processing type:
  - conventional pulse pair $(V_D)^{PP}$; polarization diversity pulse pair $(V_D)^{PDPP}$
- Corrections applied in signal processing:
  - NUBF correction: $(V_D)^{corr}_{NUBF}$

The products are computed for the first 3 Doppler moments (reflectivity Z, mean Doppler velocity V_D, spectrum width σ_D).

Verification of implemented Doppler moment estimators used in radar instrument model has been done in the past by many authors (Sirmans and Bumgarner [1975]; Zrnic [1977]; Zrnic' [1979]) for a wide range of radar signals conditions, while validation and verification of the radar simulator has been performed within the DAME project (Doppler Effect Modelling for Air Motion Estimates - Kollias [2010])

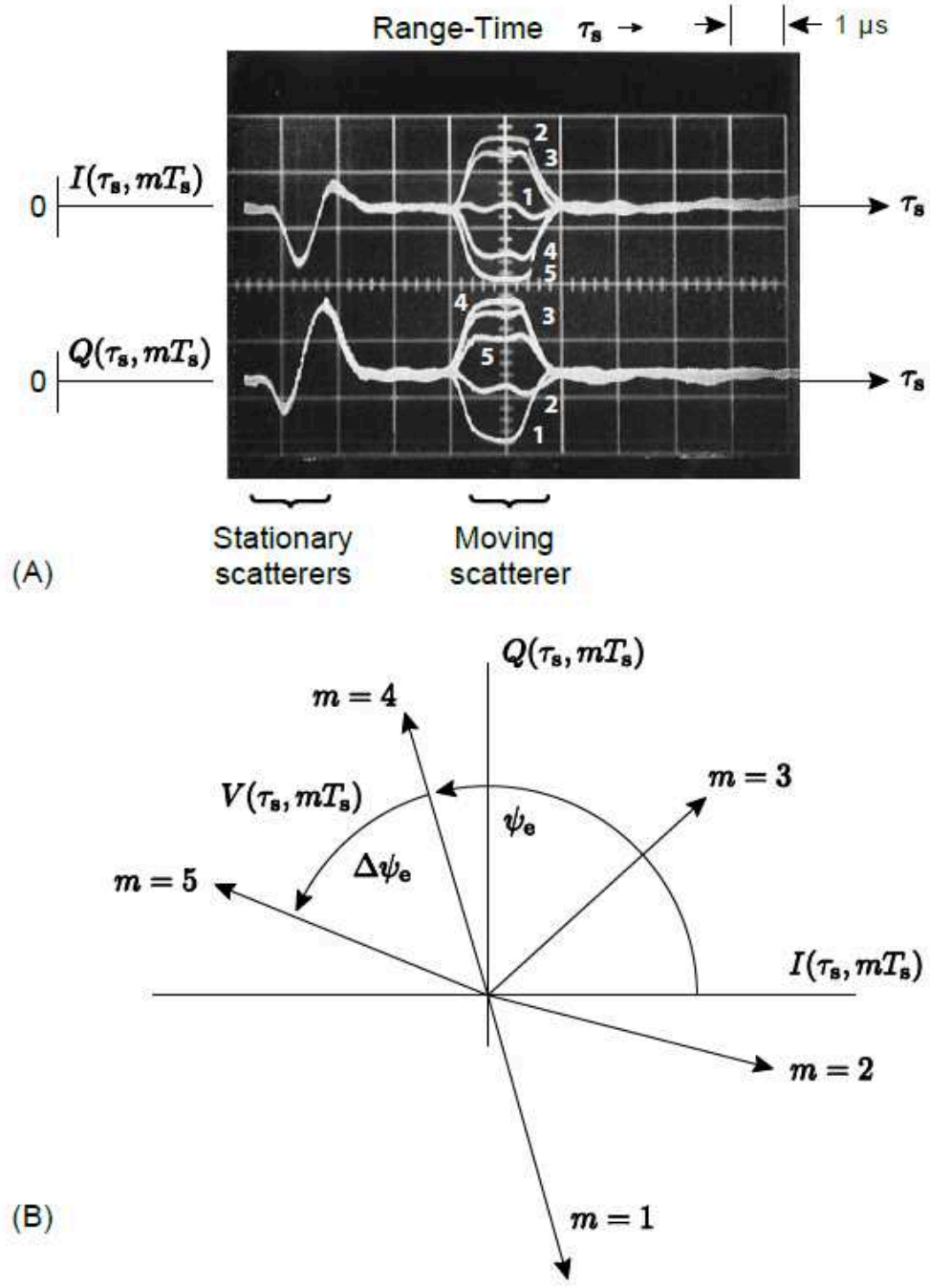

Figure 5.9: Panel (A): In-phase and quadrature signals as a function or range-time for five successive intervals, T_s, showing relative change for the stationary and moving targets. Panel (B): An Argand diagram of the five samples in the top panel at the five mT_s for the moving scatterer. Taken from North et al. [2015]

Chapter 6

EarthCARE Doppler Radar Performance Assessment for Convective Scenarios

6.1 Error Sources in Doppler Velocity Estimates

Doppler measurements from spaceborne millimeter wavelength radars are affected by a variety of errors, ranging from multiple scattering, non-uniform beam filling, aliasing, averaging error and mis-pointing induced errors to noise errors strictly related to the Doppler spectra estimators associated to the specific signal processing (e.g. pulse pair (PP), polarization diversity pulse pair (PDPP), FFT, etc.) and the short coherency time of the signal. In this chapter the assessment of the relative

effect of the different error sources for typical convective scenarios for the specifications of the EC-CPR is presented, by identifying the most relevant ones and by evaluating the impact of different correction techniques onto the error reduction. In the first approximation it can be assumed that the different error sources are independent so that the total quadratic error results from a quadratic sum of the different errors:

$$\epsilon^2_{TOT} = \epsilon^2_N + \epsilon^2_{MS} + \epsilon^2_{NUBF} + \epsilon^2_{aliasing} + \epsilon^2_{pointing} + \epsilon^2_{averaging} \tag{6.1}$$

In order to improve performance of the instrument it is important to develop methodologies capable of mitigating these errors. The radar simulation framework is exploited to disentangle the effect of each of these errors. In fact, thanks to the availability of different spectra, all error sources can be isolated and quantified - the first mandatory step towards the development of quality-controlled Doppler products.

6.2 Notional Studies of 3D Convective Scenarios - Case Study

To assess error sources in spaceborne radars the end-to-end Doppler Radar Simulator described in Chapter 5 is applied to scenarios produced by a 0.33 km resolution WRF simulation for the EarthCARE configuration (Table. 3.2). The vertical cross section

of the overpass over a convective core is shown in Fig. 6.1. The forward model mean velocity (noiseless, no radar receiver model applied) is shown on the top left panel. The convective system reaches 13 km altitude with a convective core visible at 5 - 10 km along-track distance. In the following description the adopted convention is that the velocities of hydrometeors approaching the radar are assumed positive, while downdraughts correspond to negative velocities. A signal from ranges below the surface corresponds to the second and successive order of scattering interactions with hydrometeors, possibly also involving the surface as a scattering target. In such a situation the signal is scattered at least two times before returning to the radar receiver, hence the radar no longer possesses ranging capabilities. What is even more important is the fact that the single scattering theory derived radar products are no longer reliable in regions where significant multiple scattering is present. The contour line marks the Signal-to-Noise Ratio (SNR) of 6 dB which is used as the threshold value where Doppler moments are estimated (Sect. 6.3). For clarity, the following images are plotted only for the specified SNR threshold with white pixels corresponding to the signal below the SNR threshold.

The simulator outputs of zeroth and the first radar moments for all orders of scattering (marked MS), radar reflectivity and the mean Doppler velocity are shown in the rest of the figure with the EC-CPR reflectivity shown in the center left panel. The figure reveals that the profiling capabilities are limited only to the upper part of the convective cloud for 94 GHz radar. Considerable attenuation occurs which

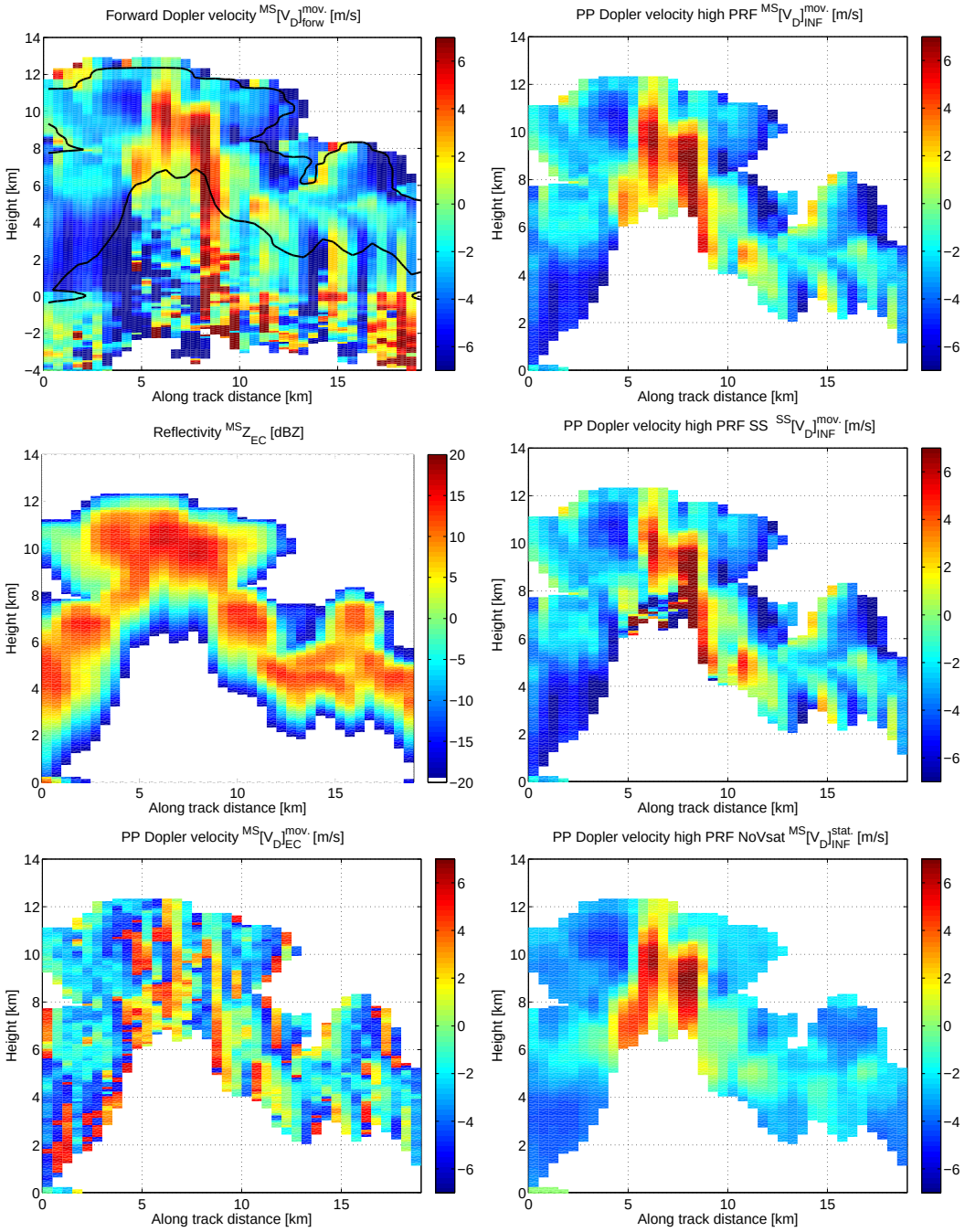

Figure 6.1: Left panels: forward mean Doppler velocity [m s^{-1}], EC reflectivity, EC Pulse-Pair mean Doppler velocity with multiple scattering (MS) signal for PRF = 7000 Hz (top, center, bottom respectively). Right panels: PP mean Doppler velocity for high PRF system: in MS approximation, in SS approximation, in MS approximation without satellite motion.

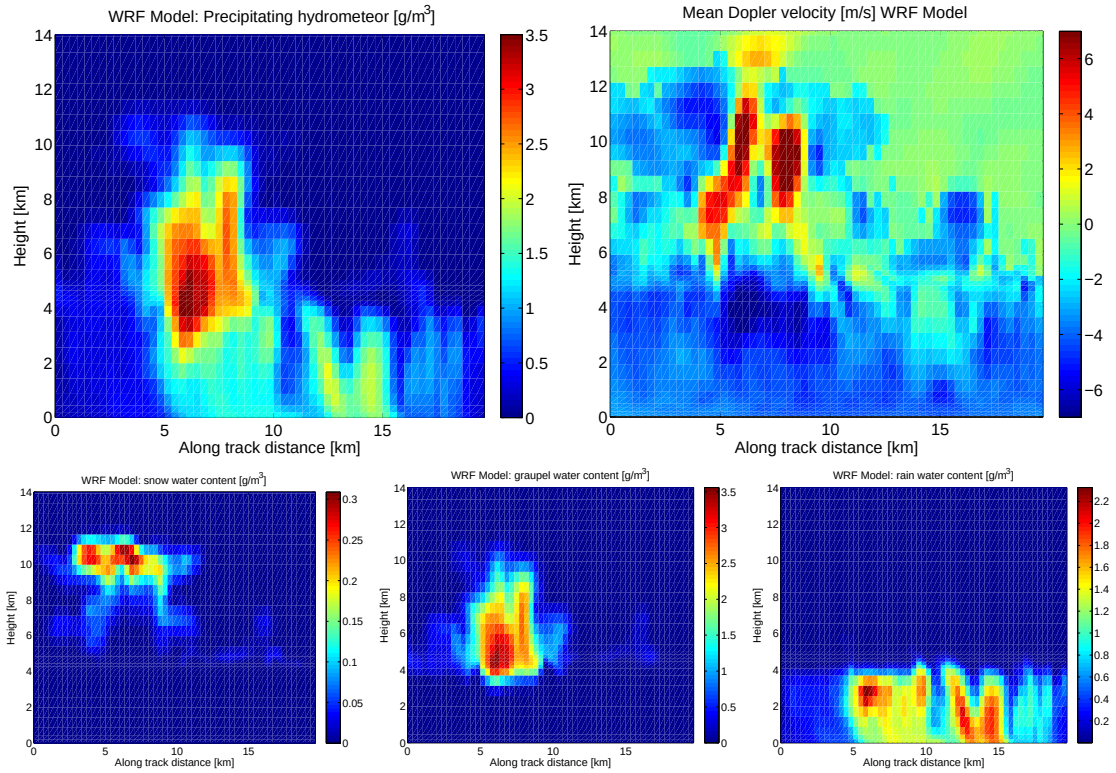

Figure 6.2: Top left panel: WRF model total hydrometeor content $[g/m^3]$ and top right: mean Doppler velocity from WRF model $[m/s]$ including vertical wind and hydrometeor fall speed. Bottom panels: the case study hydrometeor content separated into snow, graupel and rain contents, respectively.

explains disappearance of the signal (even of the strong surface echo return) in a large part of the simulation, but especially in the region of the convective core. The bottom left panel shows the mean Doppler velocities calculated for EC configuration using Pulse-Pair technique. Because of EC-CPR low PRF (PRF in the range 6.1 - 7.5 kHz) significant aliasing occurs in correspondence with velocities larger than the EC-CPR Nyquist velocity (folding velocity). To avoid and highlight the problem of aliasing the radar outputs are calculated for high a PRF configuration as well (for convenience adopted to be an integer multiple of the EC-CPR PRF, i.e. five

times the EC PRF) which is enough to avoid the problem of aliasing in the analysed scenarios. The high PRF mean Doppler velocities (also called "INF" - infinite PRF) are shown on the right side of the panel. The top right figure illustrates the mean Doppler velocities calculated including all orders of scattering for the high PRF configuration. If compared to the bottom left panel using the top right one as a reference one can see areas of velocity folding (abrupt changes in velocity). The convective core is more distinguishable using high PRF and several areas where severe velocity folding occurs at the actual EC-CPR PRF, e.g. in the lower troposphere at the 0-5 km distance (especially in the regions where heavy precipitation is present), can be seen. Updraughts exceeding 8 m/s are visible as well as downdraughts of 6 m/s. The high PRF mean Doppler velocity calculated only for the first order of scattering (SS approximation) is shown in the center right panel. This indicates that MS effects cause the radiation to dwell in the convective core, resulting in pulse stretching a phenomenon discussed in Hogan and Battaglia [2008] which generally extends the regions where the signal stays above the noise level.

The mean Doppler velocity with high PRF presents another detrimental effect - the NUBF error due to the satellite motion where large gradients in reflectivity exists (best seen in non-homogenous fields, e.g. at cloud boundaries, compared with the top right and the bottom right panels). Within the rain shaft, due to NUBF, downdraught motions can appear as updraughts (e.g.: this is visible at 15 km along-track distance, close to the ground). In the simulation framework the

output of the instrument model can be calculated as if the satellite platform was stationary - hence satellite motion will not cause errors in data, as it is displayed in the bottom right panel. The product without the satellite motion provides a reference for assessing NUBF effects and testing NUBF mitigation schemes. When compared to a high PRF Doppler velocity product it is noticeable that for boundary regions the velocity fields are more uniform if NUBF is neglected.

The WRF model vertical cross section of the case study precipitating scene is shown in Fig. 6.2. The top left panel shows the precipitating hydrometeor content including inputs from rain, graupel and snow water contents. The mean Doppler velocity resulting from the hydrometeor fall speed and the air vertical motion straight from the WRF model is shown in the right panel. In this plot no radar geometry, satellite motion or NUBF effects are introduced. This plot can therefore only be compared with ideal, high PRF, no satellite motion version of Doppler radar simulator output shown in bottom right panel in Fig. 6.1. The case study hydrometeor content separated into snow, graupel and rain contents is shown in the bottom panels of the same figure, respectively. From this the malting layer can be easily seen.

The reflectivity and mean Doppler velocity plots for another six simulations are plotted in Fig. 6.3 and Fig. 6.4. The left panels on both figures shows EarthCARE reflectivity including all orders of scattering. For clarity, the mean Doppler velocity is plotted for high PRF, thus reducing the signal processing errors. Simulations shown

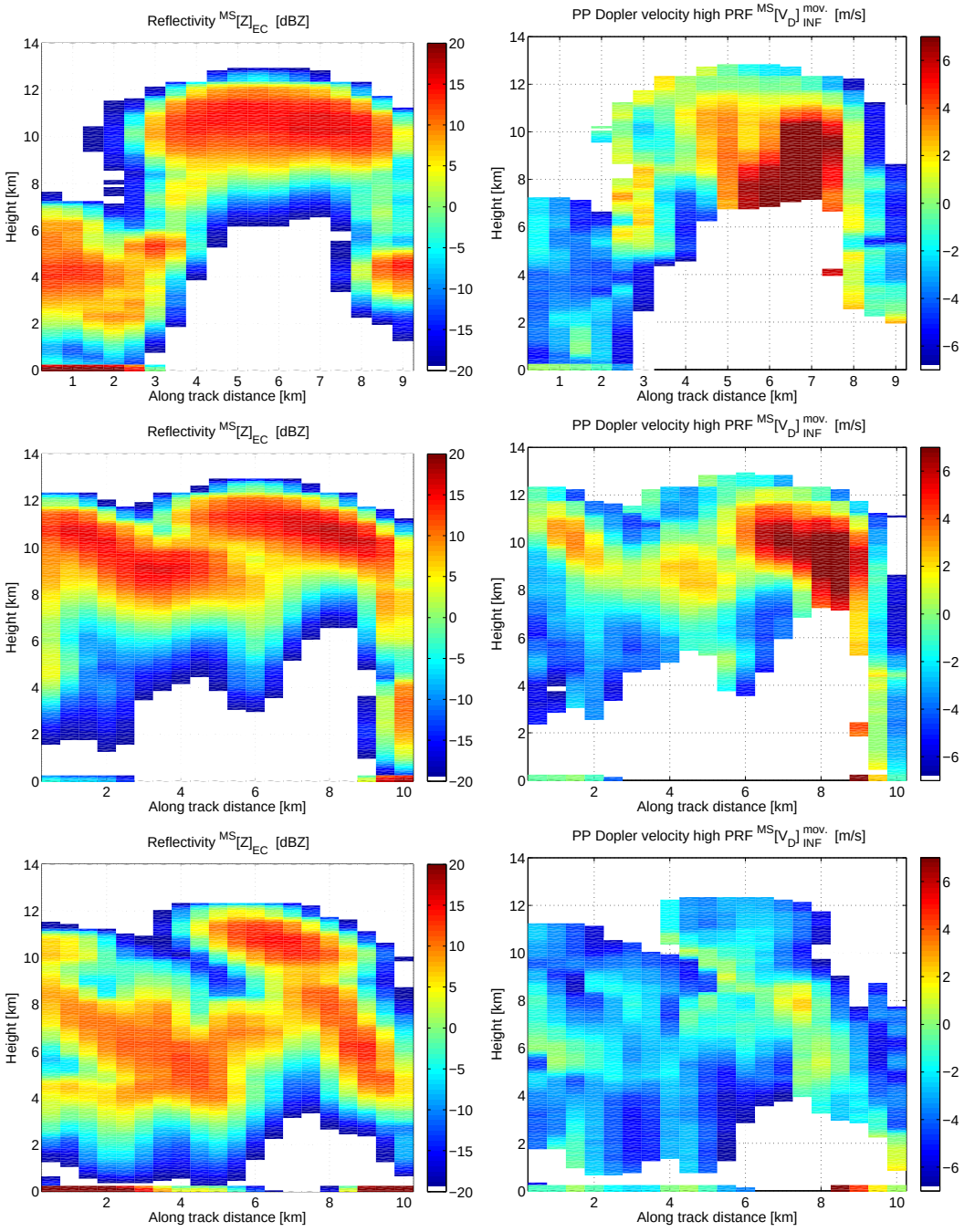

Figure 6.3: Plots of the scenarios chosen for the general analysis, part 1 (of 2). The left panels shows the simulated radar reflectivity while the right panels show the simulated high PRF mean Doppler velocity. Both include all orders of scattering (MS version).

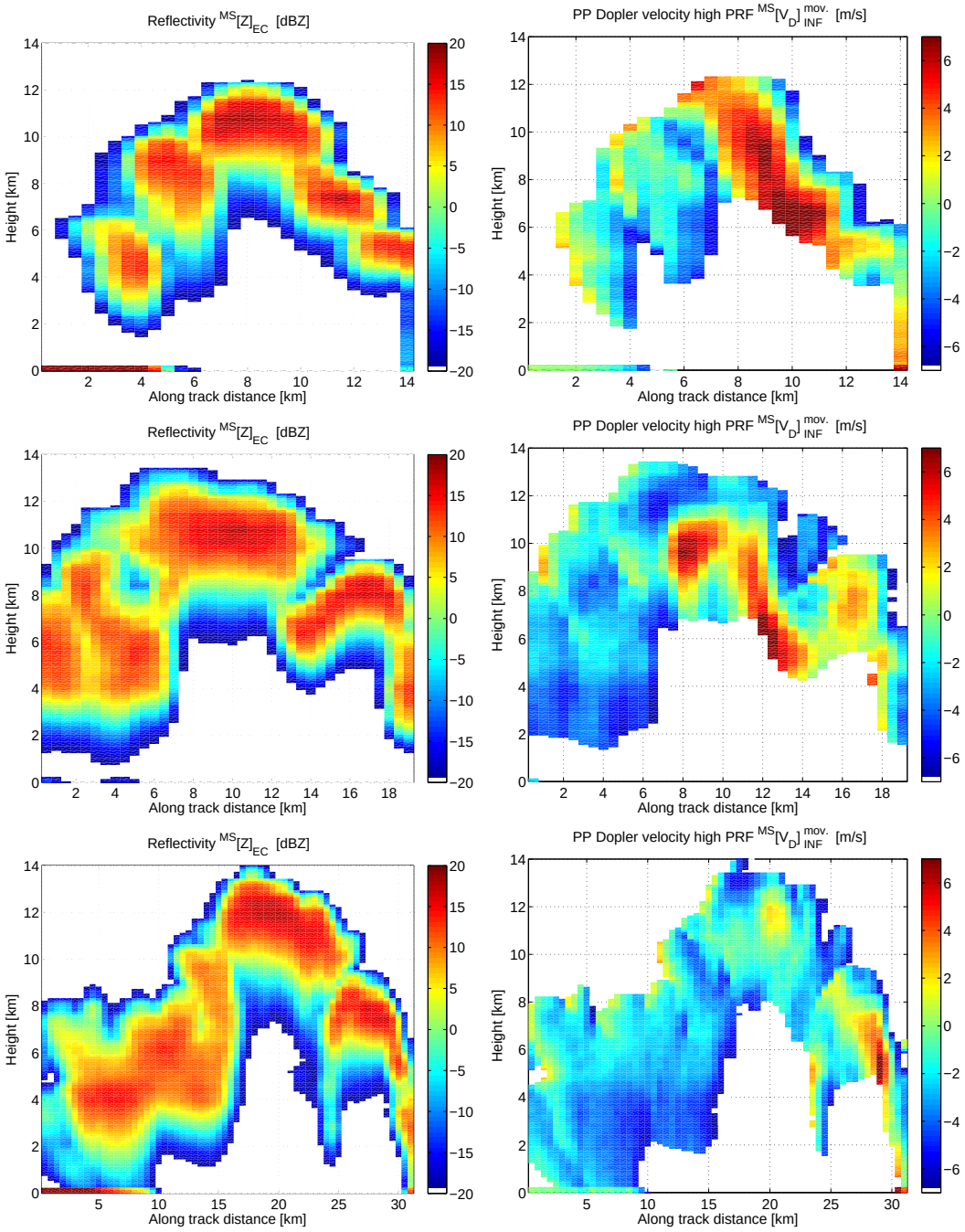

Figure 6.4: Plots of the scenarios chosen for the general analysis, part 2 (of 2). The left panels shows the simulated radar reflectivity while the right panels show the simulated high PRF mean Doppler velocity. Both include all orders of scattering (MS version).

on Fig. 6.3 and Fig. 6.4 including the case study as referred to as "whole dataset". This is the dataset from which general conclusions are drawn. The dataset was simulated for the EarthCARE configuration (for this chapter) and repeated for any of the described configurations in the following chapter.

6.3 Noise Errors

Parameters critical to the EarthCARE-CPR performance for the pulse-pair moment estimation are the spectral width, the signal-to-noise ratio (SNR) and the number of processed samples per estimate M (proportional to PRF and the along-track integration length) (Tanelli et al. [2008]). The noise error ϵ_N is a configuration and a signal processing technique dependent. Given the EC-CPR parameters the range of selected operational PRF (6.1 - 7.5 kHz) is well below the required value of 14 kHz (Sect. 2.2.1) needed to fulfill the coherency criterion (Kollias et al. [2014]). The upper limit of the EC-PRF is required by the constraint to observe the entire troposphere and represents a considerable limitation for the EC-CPR accuracy. Furthermore, the high velocity of LEO satellites implies the need for a short along-track integration to achieve a high spatial resolution. In case of EC the integration distance for level 0 products (i.e. reflectivity) will be 500 m which corresponds to 477 pulses per estimate for PRF equal to 7500 Hz (414 pulses for PRF = 6500 Hz, taking into account the EC sampling scheme: 22 pulses followed by 2 pulses empty for the background noise estimation). For Doppler velocity products the integra-

tion distance will be increased to 1 km. Using this set of parameters, accuracy in Doppler estimates may be calculated using the formula provided by Zrnic [1977] which provides the variance of the autocorrelation function for pulse-pair estimates. The left panel in Fig. 6.5 illustrates the EC-CPR Doppler velocity accuracy for the operational EC PRFs for 1 km integration length and moderate spectral width $\sigma =$ 3.8 m/s. At low SNR conditions the standard deviation of Doppler velocities is high which makes its application challenging. Kollias et al. [2014] suggested to discharge velocity estimates in regions with reflectivities below -20 dBZ, i.e. with SNR below 1.5 dB) and to filter them out from CPR Doppler velocity products. In our case it has been decided to filter out EC data with SNR lower than 6 dB, where for the lowest operational PRF the noise component of the Doppler accuracy is about 1 m/s at 1 km integration; on the other hand, and for the highest PRF, the corresponding accuracy of EC Doppler estimates reaches the asymptotic level of approximately 0.32 m/s for moderate spectral widths. The right panel in Fig. 6.5 shows the dependance of the Doppler accuracy on the integration length [0.5, 1, 2, 4 and 10 km] in correspondence to the highest possible EC PRF. The longer integration lengths can be used for stratiform clouds to improve accuracy, however, for convective systems, longer integrations should be used with caution, as this may smooth the naturally occurring variability and, as a result, decrease the accuracy (see Sect. 6.7.2).

The noise error calculated for the previously discussed case study for 500 m integration length (including the simulated spectrum width for EC configuration,

the resulting SNR and for a PRF equal to 7500 Hz) is shown in Fig. 6.6. The average value of the noise error for the case study scenario equals 0.55 m/s. This is due to the large spectrum width (shown in left panel in Fig. 6.6) in convective core.

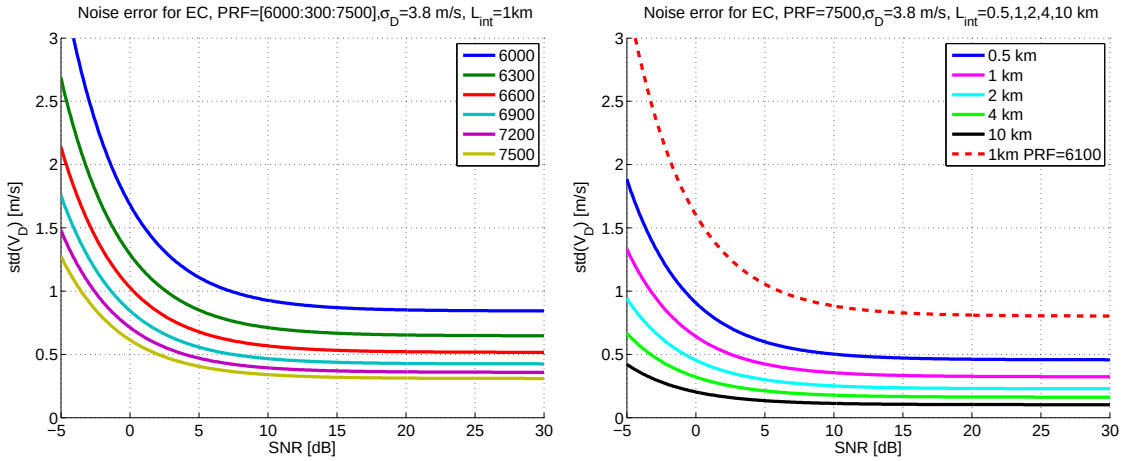

Figure 6.5: Left panel: Standard deviation of noise error for EC configuration as a function of spectral width, PRF and SNR for 1 km along-track integration. Right panel: as a function of different integration lengths of 0.5, 1, 2, 4, 10 km calculated for PRF=7500 Hz.

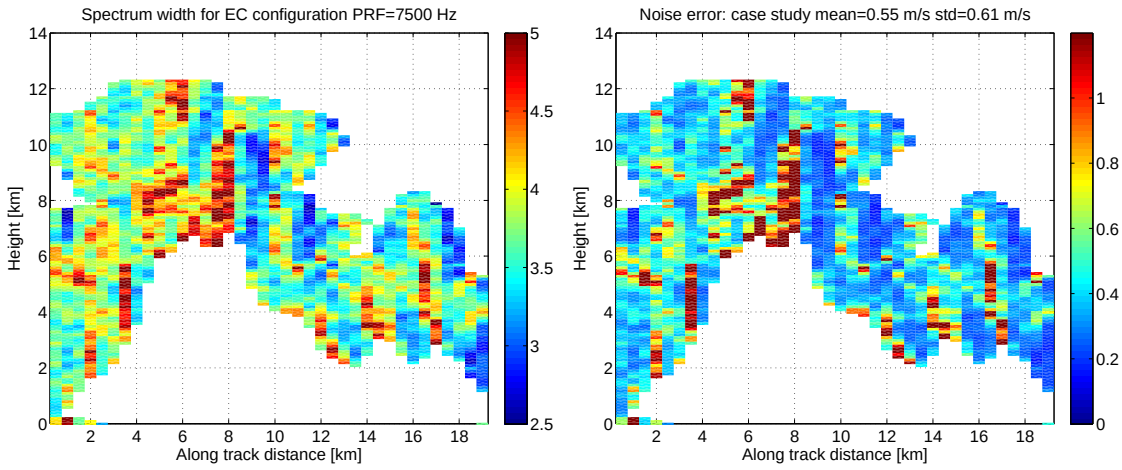

Figure 6.6: Left panel: Spectrum width for EC configuration. Right panel: noise error for case study for PRF = 7500 Hz and simulated spectrum width for EC configuration. The mean of the noise error is 0.55 m/s for case study.

6.4 Multiple Scattering Effects

During the past decade major advances have occurred in understanding of multiple scattering (Hubbert and Bringi [2000]; Marzano et al. [2003]). It has been concluded that multiple scattering is very likely to happen when considering W-band spaceborne radar observations of convective clouds as has been indicated in previous works (Battaglia et al. [2007, 2011, 2008b]; Bouniol et al. [2008]). Battaglia et al. [2010] produced a review paper on the effects of MS for pulsed millimeter wavelength radars, including MS regimes, MS effects seen in airborne and spaceborne measurements and techniques to compute MS effects.

For all ranging active instruments the radiation's time of return is assumed proportional to the straight-line, round-trip distance between the scattering volume and the receiver. Ideally the radiation scattering once is the only one contributing to the radar signal, thus the straight line assumption is satisfied and the sample volume responsible for backscattering of the transmitted radiation is ranged precisely in space. Radiation may, however, encounter a large number of scattering interactions. With each successive scatter, the dwelling time of radiation within the medium is increased and makes the returning radiation appear to originate from a range beyond the distance which it actually penetrated. Once MS contributions to the return signal become significant, the ranging capability of the instrument deteriorates significantly. Depending on the extended dwelling time of such multiple scattered radiation, its energy is mapped to range locations at considerably larger

distances from the sample volume. When this happens both the range of interaction and the backscattered power from the radar volume is incorrect. As a result, the MS effects can partially compensate for the attenuation losses, thus producing a signal even in otherwise below minimum sensitivity regions in SS approximation. As radiation does not penetrate the depths indicated by the raw return, there is no way to retrieve properties relative to such depths from the sensor signal (Battaglia et al. [2008a]). In the presence of a cloud/rain layer this translates into a "pulse stretching" well beyond the layer base (Battaglia et al. [2011]). This implies that signal can not be used for producing outputs which are valid only when the SS signal is considered.

The radiation height from which the radiation undergoing MS is truly coming from is referred as effective radiation height, and for the discussed case study has been illustrated in Fig. 6.9. With the second and higher orders of scattering becoming more and more preponderant the mean Doppler velocity of the backscattered signal will depart more and more from the SS mean Doppler velocity determined by the combined effect of the vertical wind and hydrometeors terminal velocities. On the other hand, especially in the presence of preferentially forward scattering particles, the radar pulse will propagate through the medium and the measured Doppler velocity will remain close to the SS Doppler velocity (small angle multiple scattering, Hogan [2008]).

The strength of MS effect is mainly driven by the aperture of the radar antenna

(inverse proportion) that is why it is particularly important to operate spaceborne systems with large antenna apertures. The Doppler spectrum tends to broaden with increasing MS effect adding up to the uncertainty caused by Doppler fading due to the satellite motion. Not only can MS effects overwhelm the SS reflectivity signal, but they have a large impact on the reliability of mean Doppler velocity estimates as well (Battaglia and Tanelli [2011]).

The MS effect has been defined as a crucial issue to be addressed for spaceborne radars. In particular, it is important to ascertain how deep into convection the Doppler signal is still useful, and how MS error affects the overall total error, and investigate criteria to identify such a level.

In summary, multiple scattering has several effects: 1) - enhancement of the reflectivity (enhancement of a backscattered signal) 2)- spreading a signal from a given range bin to further neighbouring range bins, due to extended propagation paths of multiple scattered waves (thus compensating for attenuation) 3)- broadening of the Doppler spectrum, leading to degradation of velocity estimates.

6.4.1 Effect of MS on Doppler Estimates

The effect on Doppler estimates caused purely by MS is displayed in Fig. 6.7. On the X axis mean Doppler velocities as derived from forward modelling (including the MS contribution) are plotted. The Y axis displays the velocities computed from cloud resolving model in SS approximation but accounting for the platform motion

and radar footprint with the colourbar corresponding to MS enhancement ΔZ_{MS} (difference in MS and SS contribution; defined in Sect. 6.2). The scatterplot shows that MS enhancements larger than 3 dB (cyan and warmer colours) have a huge impact on the reliability of mean Doppler velocity estimates, causing error several times larger than the desirable accuracy for EC-CPR. This highlights the necessity of pre-flagging MS contaminated profiles. The MS effect is extremely detrimental when the MS enhancement exceeds 10 dB (red/brown dots), which is clearly shown in the departure of the data from one-to-one line, where the errors of estimates may exceed several m/s.

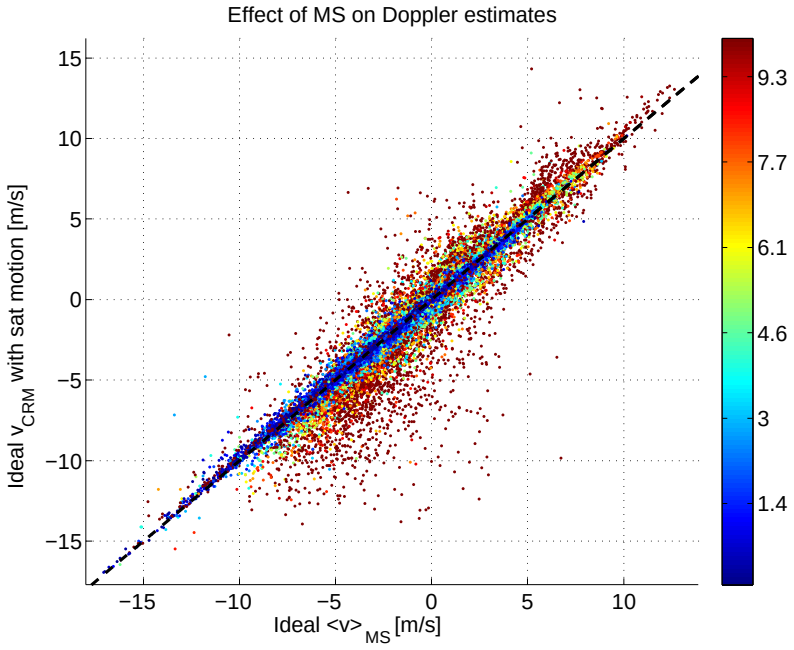

Figure 6.7: Effect of MS on mean Doppler velocity estimates. X-axis: estimates from Doppler spectra computed by the forward model including MS. $Y-$axis: SS estimates derived from the cloud resolving model output accounting for the radar footprint and the platform movement. The departure from the one-to-one line is caused purely by MS effects. The colourbar is modulated by the MS enhancement ΔZ_{MS} expressed in dB and is capped at 10 dB .

6.4.2 Identification of Onset of Multiple Scattering

The EarthCARE CPR's vertical velocity measurements will be collected in all cloud conditions, including deep convection. Thus, before the spaceborne Doppler radars are used for scientific applications, it is imperative to develop a method to identify radar range gates contaminated by multiple scattering contributions.

Linear depolarization ratio (LDR) measurements have been suggested as a method to identify MS contamination (Battaglia et al. [2007]). Since LDR measurements are not available from the EarthCARE's CPR, it is important to develop an alternative objective methodology for identifying MS contamination based on the reflectivity profile alone for flagging MS-contaminated radar-ranges. The reflectivity profiles can be characterised by several variables:

- The MS enhancement, i.e. the departure of the total observed return (that accounts for all orders of scattering) from the SS approximation, which can be computed only in a simulation framework (shown in Fig. 6.8 as horizontal distance between SS and MS profile, the green arrow):

$$\Delta Z_{MS}[dB](z) \equiv Z_{MS}(z)[dBZ] - Z_{SS}(z)[dBZ] \tag{6.2}$$

  where Z_{MS} refers to the reflectivity computed accounting for all orders of scattering for each range bin centered at the height z.

- The maximum value of reflectivities above the given height:

$$Z_{max-above}(z) \equiv \max_{\tilde{z} \geq z}(Z_{obs}(\tilde{z})). \tag{6.3}$$

  The maximum value of the reflectivity profile reach, without the contribution from surface return (i.e., calculated from TOA to 0.5 km height above the surface).

- The integral of the reflectivity above a certain threshold, $\tilde{Z}$, from the top of the atmosphere (TOA) down to level z:

$$\mathcal{I}(z)_{>\tilde{Z}} \equiv 10 \ \log_{10}\left[\int_{z}^{TOA}\left\{Z_{obs} - \tilde{Z}\right\}(z)\ dz\right] \tag{6.4}$$

  where the integral is performed only at those heights where $Z_{obs} > \tilde{Z}$, with the threshold value subtracted. The integral (shaded area in Fig. 6.8) is expressed in linear units [mm^6/m^2]. Recalling the definition of dBZ and following Kulie et al. [2010], the dBZ_{int} is used as a unit for $10\log_{10}$ of integrated reflectivity in mm^6/m^2.

The onset of MS is assumed to be the level where $\Delta Z_{MS} \equiv 3\ dB$, i.e. where the contribution of the second and successive orders of scattering are equal to the SS contribution. The $\tilde{Z}$ in the cumulative integral for EC configuration equals 12 dBZ as for reflectivity profiles with maximum values in the profile of 12 dBZ ($Z_{max-above} < 12$ dBZ) the MS effects are not likely to have any significant impact.

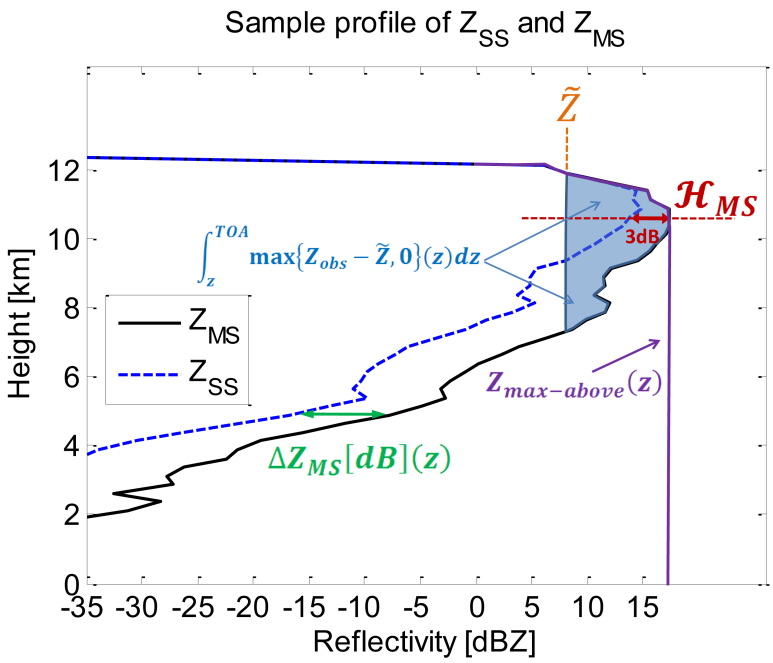

Figure 6.8: Example of simulated SS (blue) and MS (black) reflectivity profiles for deep convection as observed by a spaceborne nadir-looking 94 GHz radar.

The threshold value for the MS onset estimation was chosen based on an ensemble of simulations for which the method of the equitable threat score (ETS - calculating and optimizing detection for the four regions: MS affected pixels correctly predicted, SS range pixels correctly predicted, the missed detections and false alarms, Battaglia et al. [2011]) was used to find best performing threshold. The highest ETS value is achieved in correspondence to cumulative integral of reflectivity $\mathcal{I}(z)_{>12dBZ} = 41.5$ dBZ_{int}.

For the case study the MS enhancement and cumulative integral of reflectivity has been plotted in Fig. 6.9. The first panel shows the MS enhancement with colourbar displaying the values of the enhancement in dB. This confirms that most

of the MS events occur in convective core. On both panels the MS enhancement $\Delta Z_{MS} = 3\ dB$ is plotted as contour lines in magenta with the values of a cumulative integral plotted in yellow and black, respectively. The second panel displays the high PRF PP mean Doppler velocity with MS enhancement and the cumulative integral plotted on top of the analysed scenario. The cumulative integral works very well for deep convection, where it follows the 3 dB MS enhancement contour line. For shallower convection the cumulative integral does not always pick up the 3 dB MS enhanced regions, a further analysis is needed and a different value of cumulative integral should be applied for regions outside convective cores. However, for those regions the MS is usually less severe. The contour lines displays the region where SS theory can be used; pixels outside this region should be flagged and used for further Doppler processing.

The value of $\tilde{Z}$ in the integral calculation is configuration dependant and for CloudSat configuration the value is found to be 8 dBZ (Battaglia et al. [2011]). The different radar reflectivity threshold corresponds to the larger CloudSat footprint and the corresponding value for the cumulative reflectivity threshold is found to be $\mathcal{I}(z)_{>8dBZ} = 41.9\ \mathrm{dBZ}_{int}$.

The calculation of described cumulative integral of reflectivity with configuration dependent $\tilde{Z}$ threshold results in the best performing threshold for MS onset identification in deep convection. However, for other concepts where $\tilde{Z}$ has not been specified/simulated it was found that the value of the direct cumulative integral,

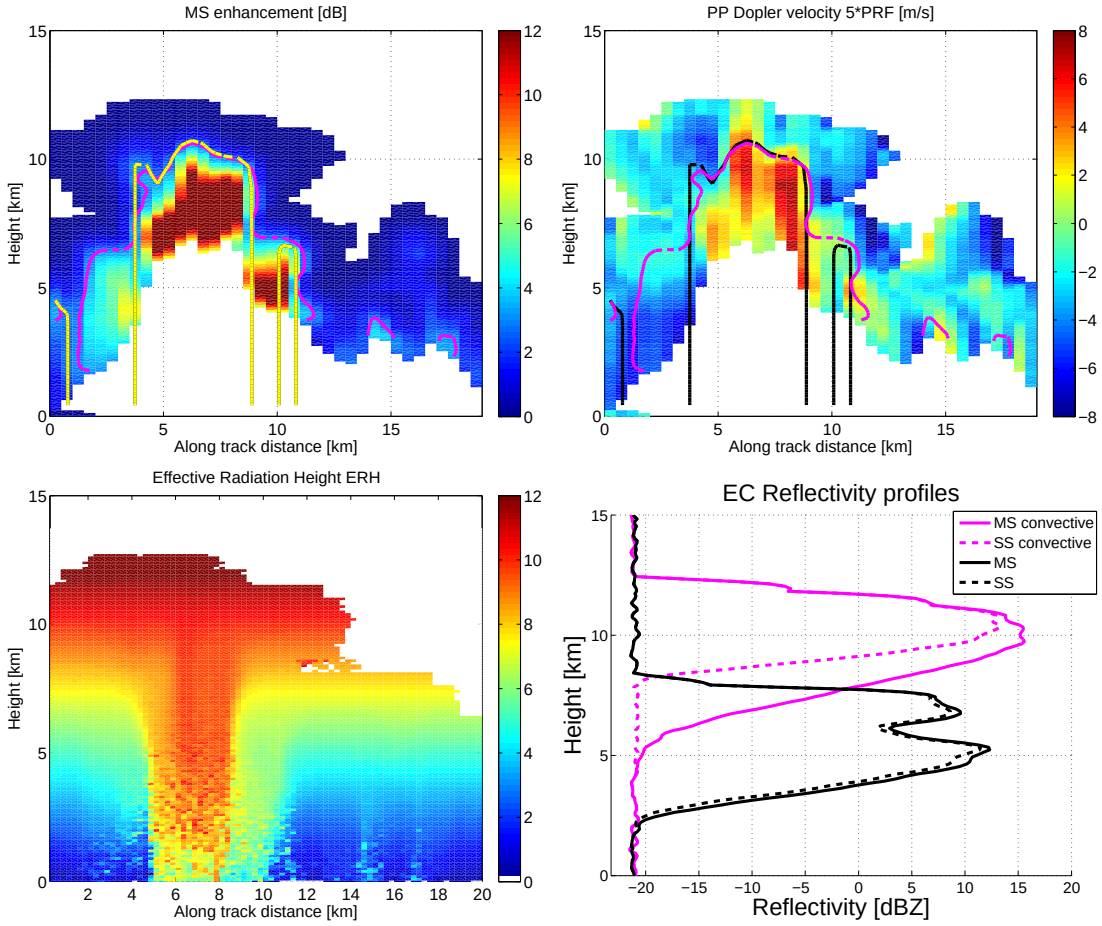

Figure 6.9: Top left: MS enhancement; top right: mean high PRF Doppler velocity. The dashed contour lines corresponds to 3 dB MS enhancement (magenta) and cumulative reflectivity integral (yellow and black respectively). Bottom left: effective radiation height ERH; right: reflectivity profiles for convective and non convective regions (7.5 and 17 km along-track).

without the threshold value of $\tilde{Z}$ gives a reliable first order approximation, and can be defined as:

$$\mathcal{I}(z) \equiv 10 \ \log_{10} \left[\int_{z}^{TOA} Z_{obs}(z) \ dz \right] \tag{6.5}$$

The threshold value of the cumulative reflectivity integral for MS onset can be roughly found by plotting the $\mathcal{I}(z)$ versus the MS enhancement. For such calcula-

tions, $\mathcal{I}(z) = 46$ dBZ$_{int}$ was found for the EC configuration and $\mathcal{I}(z) = 44.3$ dBZ$_{int}$ for CloudSat configuration.

The altitude where SS equals the MS contribution is selected as a reference of MS onset and is marked as $\mathcal{H}_{MS}$ (dashed red line in Fig. 6.8). Extensive simulations have indicated that rarely radar range gates below this level are not contaminated by MS (it may occasionally happen in multi-layer thick cloud situations). Thus, we assume that when MS contamination takes place it affects downward the whole profile. Above $\mathcal{H}_{MS}$ SS remains a valid approximation and the radar does have ranging capabilities.

6.4.3 Assessment of Errors Introduced by MS

First, to assess the effects caused solely by multiple scattering, the forward model simulated data is used with the assumption of no satellite motion of spaceborne platform or a static configuration (hence the subscript stat.). This separates MS errors from other sources and for this purpose a large dataset of simulations has been produced using end-to-end Doppler simulator for EarthCARE configuration consisting of 462 vertical profiles in convective regions. The point-wise error maps which are used to examine error sources can be defined for MS as:

$$\delta[V_D]_{MS} = {}^{MS}(V_D)\,{}^{stat.}_{forw} \; - \; {}^{SS}(V_D)\,{}^{stat.}_{forw} \tag{6.6}$$

The mean and standard deviation of the $\delta[V_D]_{MS}$: β_{MS} and ϵ_{MS}, respectively, are used as an indication of the amplitude of MS error. When selecting only the areas with $SNR > 6$ dB initial error due to MS for the ensemble of simulations yields standard deviation ϵ_{MS} of 1.22 m/s with a bias β_{MS} of 0.22 m/s. This alone already exceeds the ambitious scientific requirement of 1 m/s accuracy for EC-CPR (Sect. 3.2.2).

Aiming at optimal performance of EC-CPR the trade-offs have to be considered. The more stringent the MS threshold filter gets, the more data points are deleted and the less data will be available for a scientific analysis. There is also little sense in reducing one kind of error to minimal values, if other types are dominating. For this purpose the percentage of pixels deleted via applying the MS onset threshold has been calculated and is shown in Fig. 6.10 (blue line in the left panel). For the $\mathcal{I}(z)_{>12dBZ} = 41.5$ dBZ$_{int}$ approximately 29 % of pixels are flagged out from the whole dataset. On the same plot the standard deviation ϵ_{MS} is shown which displays large variability even for a small change of $\mathcal{I}(z)_{>12dBZ}$ value. There is also a sharp rise in the point-wise error for $\mathcal{I}(z)_{>12dBZ}$ threshold values bigger than 42 dBZ$_{int}$ which is in agreement with the previous study on a different dataset used in Battaglia et al. [2011].

Applying the cumulative integral of reflectivity $\mathcal{I}(z)_{>12dBZ} = 41.5$ dBZ$_{int}$ to the whole set of simulations reduces the standard deviation ϵ_{MS} to 0.34 m/s and mean β_{MS} down to 0.03 m/s. Results for MS error mitigation using described threshold

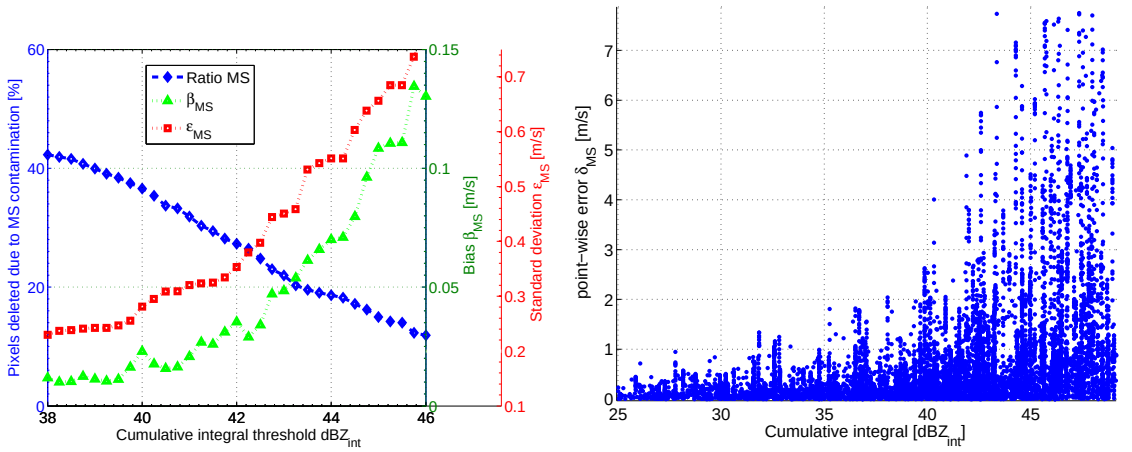

Figure 6.10: Thresholds of cumulative integral of reflectivity used as indication of magnitude of MS presence. Blue line: percentage of pixels deleted after the MS identification. Red line: standard deviation ϵ_{MS} [m/s] and green line: velocity bias β_{MS} [m/s]. Right panel: scatterplot of cumulative integral thresholds versus the point wise errors δ_{MS}.

are shown in Table. 6.1. Had all the data with MS enhancement $>$ 3 dB been deleted the resulting standard deviation ϵ_{MS} would have yield 0.25 m/s, which is fairly close to the value with data filtered out by the cumulative reflectivity threshold considering also the shallow convection in the simulations. Restricting the Doppler analysis to regions not severely affected by MS has the clear benefit of improving the Doppler velocity accuracy, however at the price of further reducing the areas with available data points of Doppler estimates.

Table 6.1: Isolated contribution of MS error for the EarthCARE configuration in convection

std $\epsilon^{MS}_{initial}$	**std** ϵ^{MS}_{corr}	**bias** $\beta^{MS}_{initial}$	**bias** β^{MS}_{corr}
1.22	0.34	0.22	0.03

6.5 Non-Uniform Beam Filling

When the radar is observing a non-homogeneous 3D hydrometeors field, the contributions to the Doppler spectrum from different portions of the resolution volume are unevenly weighted. Since the contribution of the satellite high speed to the observed radial velocity is proportional to the along-track displacement the inhomogeneous weighting induces a bias in the estimates of vertical velocity (Tanelli et al. [2004]). NUBF effects can also result in additional broadening of the spectrum width and reflectivity-dependant radar products since they are not properly weighted by the entire radar sampling volume.

This is further explained in Fig. 6.11. Each point located at along-track distance x from the antenna boresight in the radar sampling volume has an "apparent" Doppler velocity V_r which is different from its "legitimate" Doppler velocity V_D, as given by:

$$V_r = -\frac{V_{sat}}{H_{sat}}x + V_D \tag{6.7}$$

where V_{sat} and H_{sat} are the satellite velocity and altitude. Points located in the forward section of the footprint have an upward apparent Doppler velocity and aft-located points within the radar beam have a negative apparent Doppler velocity. In a homogenous medium their contributions cancel out and the resulting mean Doppler velocity has no bias. In a non-uniform filled medium the contributions are not symmetrical along the beam axis causing the NUBF error. For example, hy-

drometeors positioned in the forward/aft section of the radar antenna footprint at an along-track distance of 113 m are biased by ±1 m/s. For very strong nonhomogeneous cases (strong along-track reflectivity gradients) this can even cause fictitious updraughts/downdraughts to appear, as pointed out in the description of the case study.

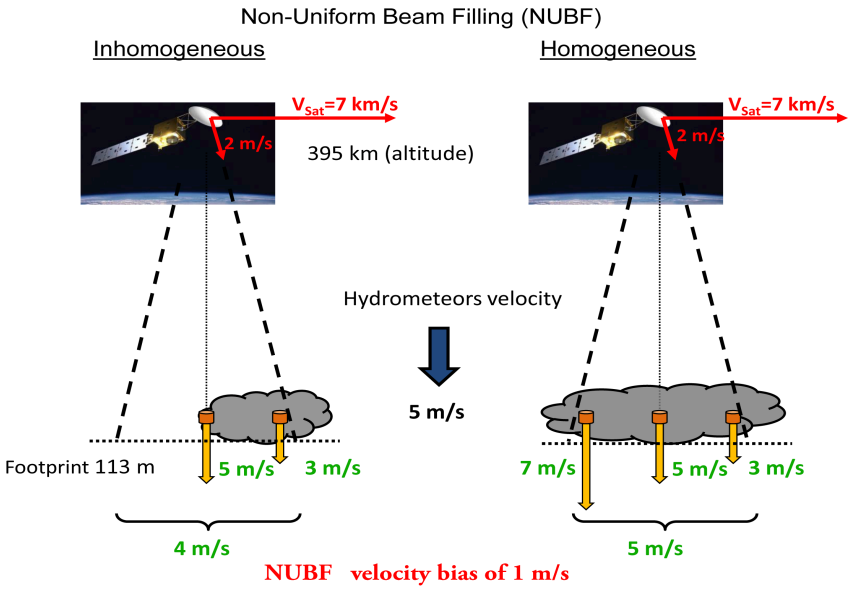

Figure 6.11: Schematic explaining Doppler velocity bias due to Non Uniform Beam Filling. If the reflectivity of the target is not uniform, the observed velocity has a bias.

The NUBF-induced Doppler velocities errors are assessed by comparing simulated data for EarthCARE radar parameters in SS approximation from forward model ($^{SS}(V_D)\,^{mov.}_{forw}$) with the data abstained from the forward modelling in SS approximation but for a static satellite platform ($^{SS}(V_D)\,^{stat.}_{forw}$). The $^{SS}(V_D)\,^{stat.}_{forw}$ is therefore assumed as the reference data in this section. All data are horizontally

averaged for 500 m and, as in previous section, only data with SNR higher than 6 dB are taken into account.

The point-wise error for NUBF is calculated as:

$$\delta[V_D]_{NUBF} = {}^{SS}(V_D)\,{}^{mov.}_{forw} \; - \; {}^{SS}(V_D)\,{}^{stat.}_{forw} \tag{6.8}$$

The point-wise error $\delta[V_D]_{NUBF}$ calculated for the case study analysed before is shown on the left panel in Fig. 6.12. It can be seen that the largest NUBF errors correspond to regions with the large along-track reflectivity gradients, displayed on the right panel in the same figure. This hint is later used in the method to correct NUBF errors.

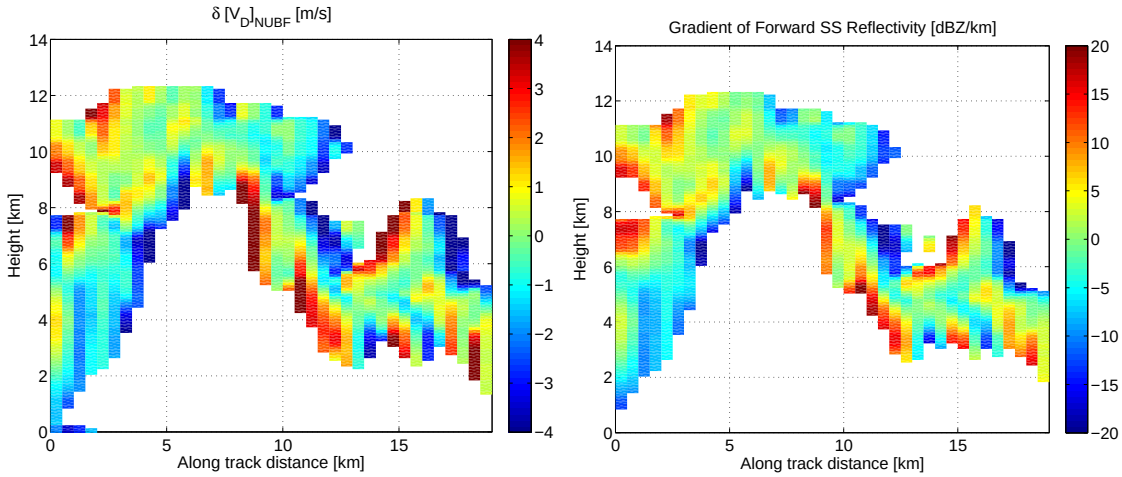

Figure 6.12: Left panel: Point-wise NUBF error $\delta[V_D]_{NUBF}$ in m/s displayed for case study. Right panel: Along-track reflectivity gradients. Colourbars in m/s and dBZ/km respectively.

6.5.1 Correction Using the Along-track Reflectivity Gradient Method

Previous studies have shown that the velocity bias due to NUBF can be corrected using the along-track reflectivity gradient technique (Schutgens [2008]; Sy et al. [2013]; Tanelli et al. [2002a, 2004]).

The corrected velocity can be computed based on the relationship:

$$V_{EC}^{corr} = V_{EC} - \alpha \times \nabla_x Z_{EC} \tag{6.9}$$

where α is a coefficient that depends on the antenna pattern and satellite geometry. In the simulation framework, where the reference mean velocity not affected by NUBF is available, the coefficient α can be calculated using the relation:

$$\alpha_{EC} \equiv \frac{\delta[V_D]_{NUBF}}{\nabla_x Z_{EC}} \tag{6.10}$$

where $\delta[V_D]_{NUBF}$ is the previously defined point-wise error. The coefficient α can be then found by a least-square linear fit between the $\delta[V_D]_{NUBF}$ and the along track derivative of Z_{EC} ($\nabla_x Z_{EC}$), given in dBZ/km.

The along-track reflectivity gradients which are found in the case study as well as for the whole dataset exceed values of 20 dBZ/km (Fig. 6.12), which agrees well with the previously described airborne data collected by ER-2 aircraft in Sect. 4.1.5. The velocity error δ_{NUBF} displays the same structure as the along-track reflectivity

gradients which proves the merit of the method for NUBF correction.

6.5.1.1 Linear and Step function: theoretical result for α_{EC}

If the idealized radar spectrum without satellite motion is not available a perturbation method can be applied to determine an analytical expression for the correction coefficient α (Sy et al. [2013]). Two simple scenarios can be considered a linear variation of Z_{EC} or a step-function variation of Z_{EC}.

The linear assumption for the EarthCARE system yields:

$$\alpha_{linear} = \frac{V_{sat}}{h_{sat}} \times \frac{\ln 10}{40 \ln 2} \times r^2 \approx 0.165 \cdot m \cdot s^{-1} (dBZ \cdot km^{-1})^{-1} \tag{6.11}$$

and the step-function:

$$\alpha_{step} = \frac{V_{sat}}{h_{sat}} \times \frac{\ln 10}{10\sqrt{2\pi \ln 2}} \times r^2 \approx 0.219 \cdot m \cdot s^{-1} (dBZ \cdot km^{-1})^{-1} \tag{6.12}$$

These two expressions can provide a range of plausible values of the coefficient α for a given reflectivity variability and a radar configuration.

6.5.1.2 The Correction Coefficient α Derived from Case Study

Plotting the NUBF point-wise error against the along-track reflectivity gradients shows that the data are strongly correlated. The slope of the least squares fit (red line) of the data on the scatterplot in Fig. 6.13 provides the value of the correction coefficient α_{EC}.

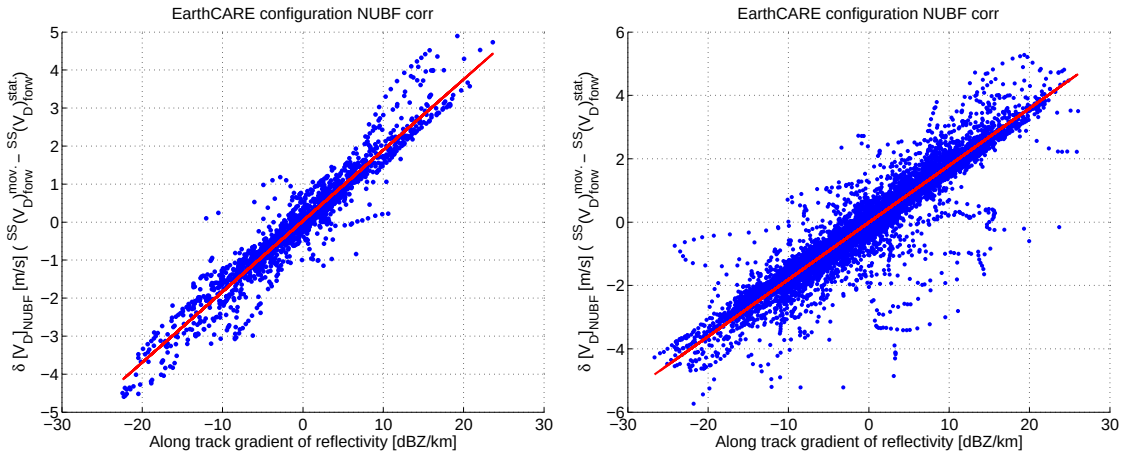

Figure 6.13: Left panel: NUBF correction based on reflectivity gradient for a case study. Scatterplot shows the dependance of the velocity bias on the reflectivity gradient. The slope of the curve provides the correction coefficient α_{EC}. Right panel: same plotted for the whole dataset.

Fig. 6.13 displays the scatterplot of the calculated velocity bias versus the along-track reflectivity gradient; it shows a linear dependance of the reflectivity gradient and velocity bias. The coefficient for the case study found by a least squares fit line is the correction coefficient α. The α_{EC} found for the case study is equal to $0.18ms^{-1}(dBZkm^{-1})^{-1}$. which fits well into the interval set by α_{linear} and α_{step}.

6.5.2 Best Coefficient α for Correction

To choose the best possible correction parameter α_{EC} a whole set of simulations has been used. A range of α_{EC} values has been tested and the final error has been compared to the initial value of NUBF error. This is depicted in Fig. 6.14 with the resulting best value of $\alpha_{EC} = 0.18m \cdot s^{-1}(dBZ \cdot km^{-1})^{-1}$. The plot also shows that small variations of α_{EC} do not significantly affect the resulting accuracy, as long as

it is in the theoretical interval set by α_{linear} and α_{step} and small variations of α_{EC} are acceptable. This is a good message for the operational use of such a correction, as the coefficient α is likely to vary from a scenario to a scenario depending on the encountered reflectivity gradients and strength of convection. Applying the correction of α_{EC} from the theoretical interval already significantly improves the final accuracy.

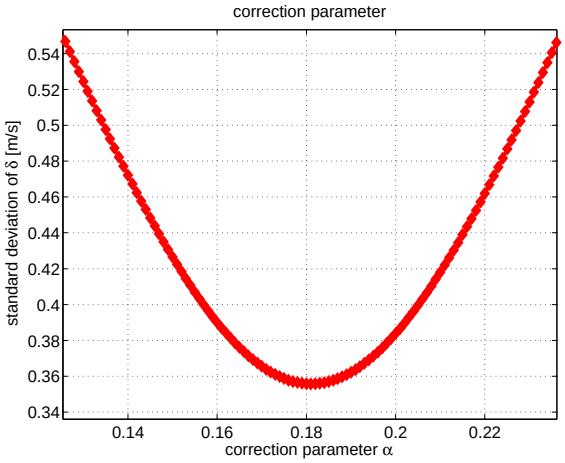

Figure 6.14: Dependance of NUBF residual errors on the correction coefficient α_{EC}.

6.5.3 Assessment of Error introduced by NUBF

Having applied the correction coefficient α to the whole available set of simulations, the initial value of the standard deviation ϵ_{NUBF} of the $\delta[V_D]_{NUBF}$ NUBF error is reduced from 2.05 m/s to a final value of 0.36 m/s (Table. 6.2). This is a significant reduction and shows how the pure effect of NUBF affects the velocity accuracy in deep convection. The velocity bias β_{NUBF} which oscillates around a zero value is reduced from -0.04 to -0.03 m/s once the ideal simulated spectrum is used. However,

because of aliasing, this gets more complicated if the instrument spectrum is used, as for the real EarthCARE-CPR situation, which is discussed in the next section.

Table 6.2: Isolated effect of NUBF correction for the EarthCARE-CPR

$\alpha = \mathbf{0.18}\ m \cdot s^{-1}(dBZ \cdot km^{-1})^{-1}$	
std $\epsilon_{INITIAL}$	std ϵ^{corr}_{NUBF}
2.05	**0.36**
bias $\beta_{INITIAL}$	bias β^{corr}_{NUBF}
-0.04	-0.03

6.6 Aliasing

Aliasing of Doppler speeds may occur when the line-of-sight velocities within the IFOV are larger than the Nyquist velocity (folding velocity). For a specific radar wavelength λ, the Nyquist folding is related to the PRF:

$$V_{Nyq} = \frac{\lambda PRF_{EC}}{4} \tag{6.13}$$

For EarthCARE CPR the PRF varies from 6100 to 7500 Hz, which corresponds to the Nyquist folding interval of $\pm$ 4.86 m/s and $\pm$ 5.98 m/s, respectively. This makes the measurements in convection very challenging as the hydrometeors' velocities often exceed this value even by several times and will be therefore possibly folded into the Nyquist interval multiple times. As has been pointed out in Sect. 4.1.4 it is not rare to see values of Doppler velocity larger than 20 m/s in convective cores.

Evidence of velocity folding for the EarthCARE configuration is demonstrated

for 10 convective profiles and displayed in Fig. 6.15 a), where the points in the top left-hand corner and the bottom right-hand corner of the scatterplot are wrongly folded (did not follow one-to-one line). It is clear that the addition of double Nyquist interval value would move aliased points closer to the one-to-one line pattern.

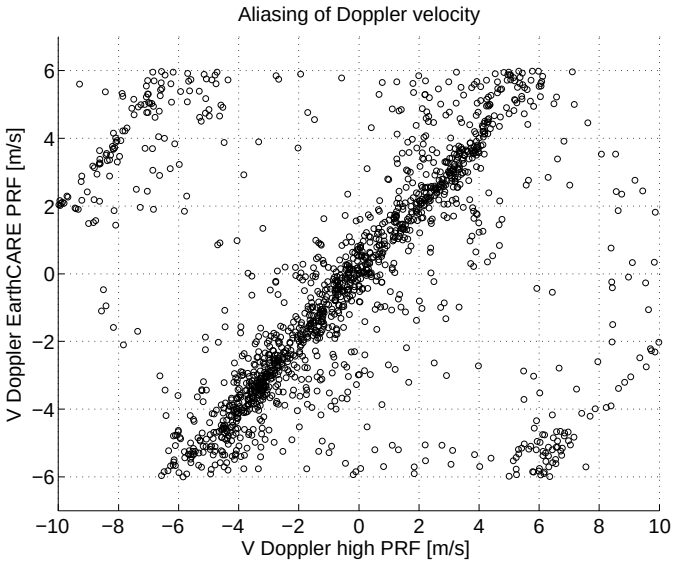

Figure 6.15: Eample of velocity folding into Nyquist interval, displayed for 94 GHz EC radar for PRF = 7500 Hz.

6.6.1 De-aliasing of Velocity in Simulator Framework

One of the symptoms of aliasing is the presence of abrupt variations of the velocity as a function of spatial coordinates. Unfortunately, so far no de-aliasing method has been developed for convective regions. The continuity or near-neighbour techniques (Sy et al. [2013]) can be useful for de-aliasing data in stratiform regions or moderate dynamic systems where velocities are only folded once and most of the velocity profile stays within the un folded region. For convective regions where a velocity

profile can be repeatedly folded there are also significant noise errors. An attempt to unfold velocities using techniques based on near-neighbour or continuity fields may cause the whole velocity field to be wrongly de-aliased. As identified using airborne data, Doppler velocities in convection displays no clear correlation to reflectivity or its horizontal or vertical gradients which might help with the de-aliasing. Hence, to assess the effect of aliasing on Doppler velocity, theoretical (available only in simulator framework) reference method is used to unfold Doppler velocities. It makes use of aliasing-free Doppler velocity such as high PRF $(V_D)_{INF}$ or forward model velocity $(V_D)_{forw}$ as a reference. The function calculates differences between the reference velocity and aliased velocity $\pm 2V_{Nyq}$ and searches for the minimum of the differences which are output as the de-aliased velocity. The process is repeated in the vertical and horizontal direction.

An example profile of Doppler velocity de-aliased in such a way is displayed in Fig. 6.16. The velocity profile before de-aliasing $(V_D)_{EC}$ is shown in magenta. It displays several regions of velocity folding when compared to $(V_D)_{INF}$ shown as a black dashed line. The black line is used as an aliasing-free reference. The properly de-aliased profile of velocity $(V_D)_{EC}^{de-al}$ is displayed as a green curve. This is a relatively easy case showing the concept when the PRF is high (7500 Hz, $V_{Nyq} =$ $\pm$ 5.98 m/s) and SNRs assume positive values as can be seen on the left panel in Fig. 6.16. Aliasing is expected to be much more severe for convective regions when the EC-CPR usees low PRF with aliasing errors coupled with noise errors resulting

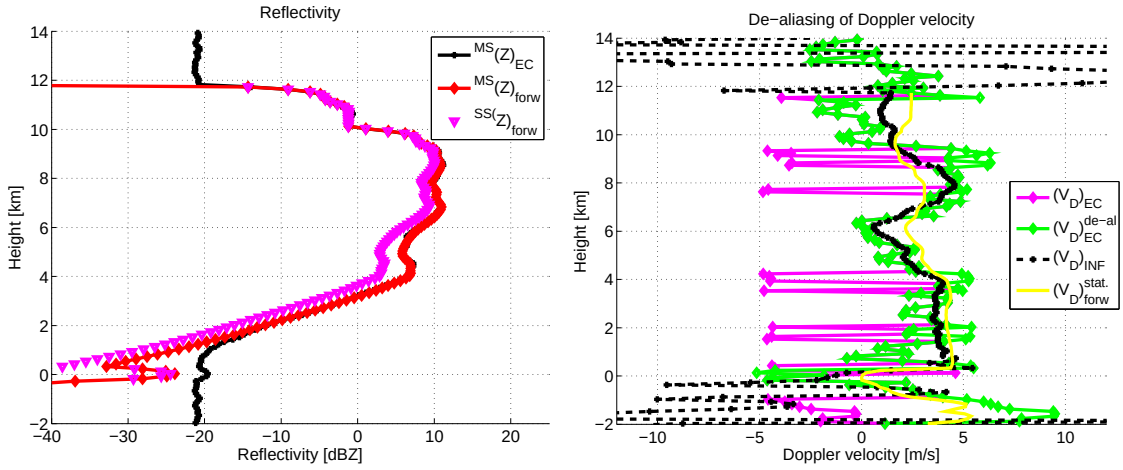

(a) Reflectivity (b) De-aliasing of $(V_D)_{EC}$

Figure 6.16: De-aliasing of Doppler velocity

from a broad spectrum and/or profiles with low SNR.

6.6.2 Along-track Averaging of the Pulses

The received signals will be averaged (in each range cell) for a period of time equivalent to the transit time of the satellite over the along-track averaging distance. The processing for this calculation will be performed onboard the satellite to minimize the downlink data rate. Along-track signal integration is a well-known approach to reduce the variance of measurements, however it comes at a price of a reduced representativeness of the underlying scenarios.

The EarthCARE-CPR will measure the reflectivity for 500 m along-track integration length. The Doppler velocity will be integrated for 1 km distance and will be available as quality controlled joint standard grid product. As the NUBF effect can be corrected using the along-track reflectivity gradients it is beneficial to correct

this error at the finer scale of 500 m integrated reflectivity. Also the MS onset can be calculated at this stage. A quality controlled product at 1 km integration length can be produced next, as illustrated in Fig. 6.17.

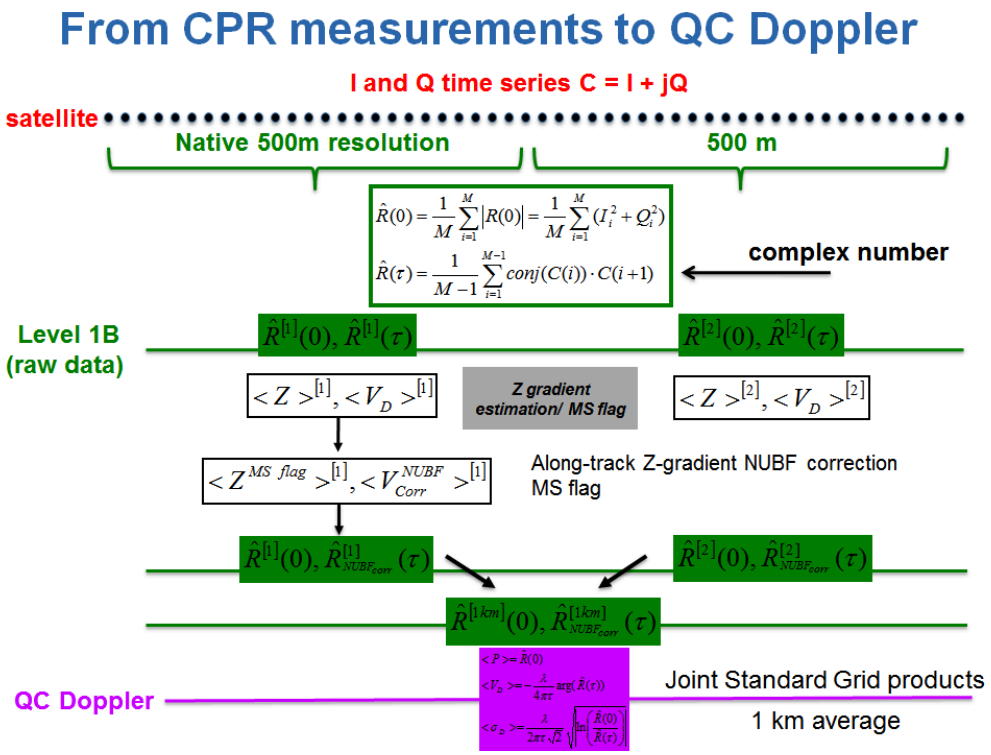

Figure 6.17: Schematic showing simulation of Doppler moments from I and Q time series for 1 km along-track integration - Quality Controlled Joint Standard Grid Product, image credit A. Battaglia.

6.7 Total Error Budget for EarthCARE-CPR

Using the specifics of the EC-CPR, the radar simulator produces the Doppler velocity ${}^{MS}(V_D)^{mov.}_{EC}$, as sampled by the EC-CPR radar and including all detrimental effects and all orders of scattering. In order to produce a quality-controlled data

product in convective scenarios the following procedure is proposed:

I –> Identification of pixels with good SNR (SNR >6 dB).

II –> Exclusion of pixels affected by surface clutter and deletion of signal coming from below the surface.

III –> Identification of pixels affected by MS via the threshold of the cumulative integral of reflectivity.

IV –> Application of the NUBF correction based on the coefficient α coming from along-track reflectivity gradients.

V –> Total error budget estimation for EC-CPR for spectra for which no de-aliasing has been applied.

VI –> Total error budget estimation for EC-CPR for spectra when the spectra is de-aliased using simulator framework available only de-aliasing technique.

VII –> Doppler velocity accuracy is estimated on the quality controlled product.

Note that, in reality the VI and VII points from the procedure can be undertaken within simulation framework only, however this part of the study allow to assess the quality of the Doppler products if the de-aliasing techniques are found.

6.7.1 Total Error Shown for Case Study

The whole procedure is illustrated for the previously described case study (Fig. 6.1) for a 500 m integration length. The EC mean Doppler velocity ${}^{MS}(V_D)\,{}^{mov.}_{EC}$ with the first three steps already applied (SNR, surface clutter and MS onset) is shown on the top left panel in Fig. 6.18. The contour lines display the SNR >6 dB for MS approximation (in magenta) and for SS approximation (plotted in black). The application of the cumulative integral of reflectivity as MS threshold further restricts the regions where data are available. This reveals that 94-GHz system can be used to characterise the upper part of convective cores only. The scenario is plotted for the highest PRF available for EC-CPR and even for this moderately dynamical system there are still regions with velocity folding (compare the top with the bottom left panel). The center left panel shows the data with the NUBF correction applied. After the NUBF correction the regions where severe NUBF effects are likely to exist (i.e. in the presence of large along-track reflectivity gradients, proximity of cloud borders) have more uniform velocity fields (i.e. top range-bins at 0 - 12 km distance, compare to the reference velocity with no NUBF effect shown in the top right panel). The regions of severe velocity folding are more pronounced. After educated de-aliasing (only available in the simulation framework) is applied to the NUBF corrected data the resulting velocity fields are displayed in the bottom left panel. These velocity fields demonstrate a better resemblance to the reference forward mean Doppler velocities without satellite motion ${}^{MS}(V_D)\,{}^{stat.}_{forw}$ (depicted in the

top right panel). The main difference between these two panels is the EarthCARE noise error embedded in the corrected EC product.

The last two panels show the point-wise velocity errors: the initial velocity error and the error after all corrections including the de-aliasing. The initial velocity field shows very large errors reaching positive and negative errors of 4 m/s. The final velocity field displays a much more homogenous field, with errors within -1 to 1 m/s interval for the majority of range-bins. However, the described case study is simulated adopting the highest EC PRF and has been de-aliased by using educated the de-aliasing method (i.e. the best possible de-aliasing). This highlights the fact that proper de-aliasing is crucial for EarthCARE CPR configuration.

6.7.2 Calculations of Total Doppler Velocity Error Budget for the whole Dataset

Finally, the whole dataset is used to assess the EarthCARE-CPR error budget. The point-wise error is calculated as:

$$\delta[V_D] = {}^{MS}(V_D)\,{}^{mov.}_{EC} \; - \; {}^{SS}(V_D)\,{}^{stat.}_{forw} \tag{6.14}$$

Proceeding with the methodology the previously described accuracy of Doppler velocities is found after each step of corrections for 1 km integrated Doppler velocity. For the 1 km integrated products the gradients of reflectivity provided at 500 m

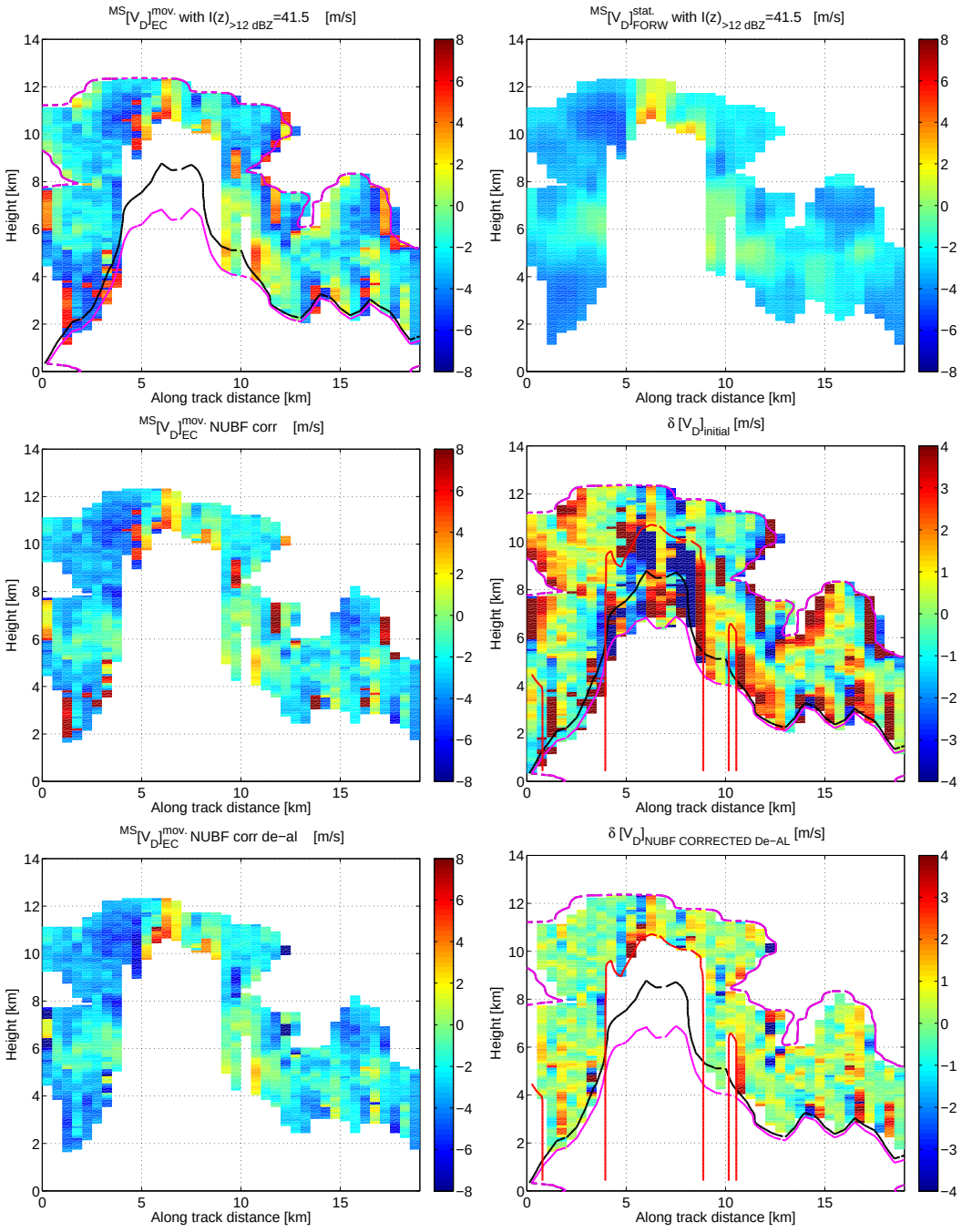

Figure 6.18: Left column: EC-CPR Doppler velocity with MS affected pixels excluded (top), with NUBF correction (center) and with de-aliasing function (bottom). Right column: Top: Doppler velocity without satellite motion (reference), center: initial point-wise error, point-wise error after corrections for MS, NUBF and de-aliasing.

are used to correct for the NUBF biases (as illustrated in Sect. 6.6.2). The results are summarized in Table. 6.3. The initial error is calculated already after the SNR thresholding and the reduction of surface clutter (steps I and II). The following two columns correspond to the standard deviation ϵ of $\delta[V_D]$ after the NUBF correction and the MS correction, respectively. The next column illustrates the accuracy if perfect de-aliasing is possible. The last column is an indication of the averaging error, described later. The 1 km integrated accuracy for quality controlled standard joint product is provided for PRF = 6100 and PRF = 7500 Hz. For comparison - the accuracy of Doppler velocity has been calculated for 0.5 and 2 km integration length for the highest PRF (7500 Hz).

Until now the Doppler velocity product integrated for 1 km along-track distance was compared with the reference product integrated also for 1 km along-track. However, as the reflectivity from the EarthCARE-CPR will be provided at 500 m along-track integration, it can be investigated if the integration of Doppler product for longer distance in convection introduces an additional "averaging" error. This can be done by interpolation of the Doppler product provided at 1 km to the 500 m resolution and by comparing these products with the 500 m resolution reference Doppler velocity. The difference between those values is referred as "averaging error" due to smoothing out the fine structure of convection and averaging out of the aliased velocities. The accuracy of the Doppler velocity calculated for 1 km integration (and in the next row for 2 km) and then interpolated to 0.5 km resolution is shown

as the last column in Table. 6.3. This allows to estimate the effect of averaging in convection to be in the order of $\sim$ 0.15 m/s and shows that long integration in convection is not advisable and can introduces additional uncertainties.

Table 6.3: Accuracy of EarthCARE-CPR Doppler velocity in m/s

PRF	Integration	ϵ INITIAL	ϵ NUBF corr	ϵ MS corr	ϵ De-al corr	Averaging effect
6100 [Hz]	1 km	3.14	2.97	**2.70**	1.74	
7500 [Hz]	1 km	2.88	1.98	**1.57**	1.07	1.69
7500 [Hz]	2 km	2.72	1.75	1.54	0.97	1.68
	0.5 km	3.19	2.49	2.08	1.43	

The last of the errors not discussed before is the pointing error. This depends on the satellite hardware, and for the EarthCARE the goal value of mis-pointing accuracy is $\sim$40 microrad and the resulting contribution towards the total error budget for EC configuration is believed to be $\sim$ 0.3 m/s (Tanelli et al. [2005], private communication with A. Battaglia and P. Kollias).

Thus, the final value for the Doppler velocity accuracy in deep convection for the highest PRF is just slightly under 2 m/s. For lower PRF the aliasing is the biggest contributor to error. The aliasing of velocities is also the most difficult error to mitigate making the measurements in deep convection very challenging.

6.8 Results and Discussion

The main sources of uncertainty in EarthCARE-CPR Doppler products in convective clouds have been described. Using the simulation framework it was possible to separate the different sources of error and estimate the contribution of each of them.

The MS error not only causes biases in Doppler velocity estimates but excludes also use of the SS theory for radar products in regions where SS theory is not valid. It was found that the threshold value of cumulative integral of reflectivity $\mathcal{I}(z)$ can be used as a reliable proxy for the identification of the regions affected by MS in deep convection. The threshold of 41.5 dBZ_{int} reduces the standard deviation of the MS point-wise error from 1.22 m/s to 0.34 m/s. As a result, pixels where $\mathcal{I}(z)$ exceeds the selected threshold should be excluded, which restricts the regions where quality-controlled Doppler products are available. For our dataset of convective storms this corresponds to a 29 % reduction of coverage.

Another source of error severely affecting accuracy of spaceborne Doppler radars is Non-Uniform Beam Filling, which is connected to the high velocity of the satellite platform and to regions where the medium is not homogenous in FOV of the satellite. It has been shown that using the reflectivity gradient technique the NUBF error can be mitigated via use of correction coefficient α. The correction coefficient α_{EC} for the EarthCARE configuration has been estimated to be $\alpha_{EC} = 0.18m \cdot s^{-1}(dBZ \cdot km^{-1})^{-1}$. After the NUBF correction, there is a significant reduction of the standard deviation of the point-wise error introduced by NUBF from 2.05 m/s to 0.36 m/s, which is the residual NUBF contribution to the error budget.

The noise error connected to chosen radar specifics and Doppler moments estimation method can also introduce severe detrimental effect on Doppler accuracy, especially for combined low PRF, large spectral width and low SNR conditions. It

is likely that this kind of error can take up 0.5 m/s from the overall error budget. For future EC follow-up mission the noise error can be mitigated by choosing other signal processing techniques or using higher PRFs.

In addition to previous considerations the error due to the velocity folding seems to be both the hardest to mitigate and the most significant for the EarthCARE-CPR in deep convection. It stems from the Doppler dilemma and the use of low PRF. Airborne radar data indicated that updraughts in convective cores can be bigger than 25 m/s which exceeds the EarthCARE resolved velocity interval several times over. It is worth noting that the extreme cases from airborne data or recorded in the literature involve even bigger updraught velocities than the simulated scenarios in this work. The fact that the velocity fields can be folded many times and that in convective systems updraughts and downdraughts are not correlated to reflectivity fields or its gradients makes the development of a reliable de-aliasing techniques still a big challenge. De-aliasing of the Doppler velocities using an idealized de-aliasing scheme reveals that velocity folding is responsible for at least 0.96 and 0.5 m/s error for the lowest and the highest PRF, respectively. Without proper de-aliasing, the estimated Doppler velocities in convection will have a very large uncertainties, thus not meeting the ambitious scientific requirements.

The other sources of error affecting Doppler velocity measurements are mentioned briefly error due to antenna mis-pointing which is believed to be in the range of $\sim$ 0.3 m/s and the averaging error. The averaging error stems from the natural

structure of convective clouds and as phenomenon of high spatial resolution the long integration traditionally improving the accuracy of Doppler products may actually cause decrease it. This is highly dependent on type of convection and varies with each separate system.

Finally the total error budget for EarthCARE CPR Doppler products has been discussed by disentangling the contributions from the different sources of errors, apart from mis-pointing errors. Techniques to mitigate the MS and NUBF errors were also proposed. The reflectivity profiles at 500 m along-track integration were used to correct for NUBF effect of the 1 km-integrated mean Doppler velocities. The results are summarized in Table. 6.3 for two low and high EC-CPR PRFs (6100 and 7500 Hz). For both PRFs the initial error oscillated around 3 m/s, for data with SNR $>$ 6 dB. For 6100 Hz PRF the NUBF and MS correction reduced the error to 2.97 and 2.7 m/s respectively. For this low PRF the velocity aliasing and noise errors pose a serious difficulty. On the other hand, for the higher PRF of 7500 Hz the NUBF and MS correction reduced the total error from 2.88 m/s to 1.98 and 1.57 m/s respectively. These values are closer to the scientific requirements, hence use of the highest possible PRF is recommended in convective regions. However including mis-pointing errors and the fact that in the tropics EC-CPR will use lower PRFs the total error will probably be in the order of 2 m/s.

Those results were imperative to pursue in finding optimal technique for EarthCARE-like Doppler radars for use in convective systems, especially the technique where

aliasing of velocities can be significantly reduced. One of possible approaches is polarization diversity, described in the following chapter.

Chapter 7

Performance Assessment of Future Doppler Radar Concepts with Polarization Diversity

7.1 Introduction

The Polarization Diversity Pulse-Pair (PDPP) technique has been developed to overcome issues of the standard Pulse-Pair technique, and was first introduced by Doviak and Sirmans [1973]. The main strength of PDPP is that it can disentangle the maximum unambiguous range and the maximum unambiguous velocity of a Doppler radar. A solution for the so-called Doppler dilemma. Bringi and Chandrasekar [2001] noted that for meteorological scatterers the back scattered signal from ensem-

ble of scatterers at copolar horizontal ($V_H^H(t)$) and vertical polarization ($V_V^V(t)$) have a high degree of correlation (notation: channel of polarization $V_{sent}^{received}$). However, the correlation coefficient between copolar ($V_H^H(t)$) and cross-polar ($V_V^H(t)$) component is low. Similarly, the correlation coefficient between ($V_H^V(t)$) and ($V_V^V(t)$) is low. Having high degree of correlation between the orthogonal copolarized backscatter coefficients of atmospheric particles closely spaced with each other allows to use modified pulse-pair techniques to mitigate the effect of the aliasing of velocities. This means that the aliasing problem can be eliminated in most cases with the accuracy of Doppler velocity estimates typically better compared to a standard Pulse-Pair (PP) due to the higher sampling of a fast decorrelating signal typical for spaceborne measurements. Pazmany et al. [1999] used the PDPP technique to study the reflectivity and velocity structure in severe thunderstorms using a 94 GHz ground-based radar. Kobayashi et al. [2002] proposed this technique for spaceborne applications of a nadir-looking configuration, while Battaglia et al. [2013] tested PDPP for W and K_a-band radars with an in-depth discussion of the accuracy in Doppler velocity estimates as a function of the pulse-pair interval for a wide range of spectral widths. The paper includes methods to mitigate cross-talk between orthogonally polarized channels, which are one of the drawbacks of the method.

Having linear copolar and cross-polar moments, the linear depolarization ratio (LDR) can be estimated. The LDR can be used for particle and precipitation phase identification and to improve the quality of the data. Specifically, the polarization

mode can be utilized for discrimination between different hydrometeor types (e.g., ice crystals, snowflakes) which is shown in Fig. 7.1. Furthermore, it can be utilized for identification of mixed-phase conditions and the melting layer. Figure 7.1 illustrates the dependance of the LDR on different hydrometeor types and shows the details which polarization can provide on the atmosphere structure. For instance, at a vertical incidence angle the melting layer has a very high cross-polarization signature ($LDR > -15dB$) providing the ability to clearly mark the boundary between snow and liquid.

Another important application of polarization measurements is the detection of multiple scattering events, with high LDR values being a proxy for large multiple scattering enhancement as already noted in Battaglia et al. [2007]; this topic is further investigated in Sect. 7.4.1.

In this chapter the author presents the results of Doppler radar simulations where the polarization diversity technique has been applied to an EarthCARE-like radar system, assuming that it has two orthogonally polarized transmitters and receivers. It has also been applied to the radar configurations described in Sect. 3.3 for CLDY, ACE and the "large antenna concept" for both 94 GHz and 35 GHz frequency radars. Due to a high degree of similarity between 94 GHz EC-CPR and CLDY-CPR, the EC-CPR specifics were chosen to simulate the PDPP technique. This approach enables a direct comparison of the contribution of different error sources as a function of the radar parameters.

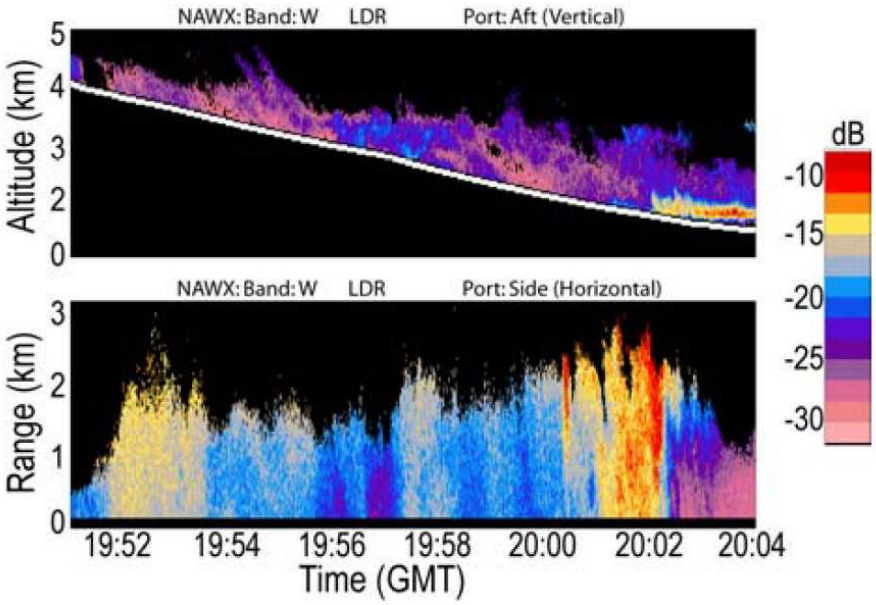

Figure 7.1: LDR measured by $NAWX$ on 01.03.2007 as the aircraft descended form an altitude of 4 km to 1.5 km. Top: Vertical cross-section form upward pointing radar beam. The white line shows the aircraft altitude. Bottom: LDR form side-looking dual-pol antenna (CLDY-Proposal [2011]).

7.2 Signal Processing for Polarization Diversity Technique

The signal processing for PDPP varies significantly from standard pulse-pair processing. A polarization diversity radar measures a signal simultaneously using two channels to receive scattered power from two orthogonally polarized pulses closely spaced with the pulse-pair separation denoted as T_{HV}. Despite the use of pulses from separate receiver channels (H and V) their phase coherency (due to short intervals between the H and V transmission) is the main attribute to extract the Doppler velocity. The Nyquist (folding) velocity in such systems can be calculated using

$V_{Nyq} = \lambda T_{HV}/4$. The pairs of orthogonal pulses are transmitted separated by the interval marked as T_s. The pair-repetition interval T_s is related to the unambiguous range, $r_{max} = cT_s/2$.

For a polarimetric radar the measured voltage that corresponds to scattering from range r at time t two components can be written in terms of signal and noise components according to:

$$\mathbf{V_m}(r,t) = \begin{bmatrix} V_{VV}(r,t) & V_{HV}(r,t) \\ V_{HV}(r,t) & V_{HH}(r,t) \end{bmatrix} + \begin{bmatrix} N_V(r,t) & N_V(r,t) \\ N_H(r,t) & N_H(r,t) \end{bmatrix} \tag{7.1}$$

where V_{ij} is the signal component of the voltage at the output of the $i-$polarized receiver when j polarization was transmitted, and N_V and N_H represent system noise in the vertical and horizontal receiver channels, respectively.

The term V_{ij} where $i \neq j$ represents cross-talk between the receiving channels which originated from cells located at ranges $r \pm \Delta r$, with $\Delta r = cT_{HV}/2$. This can affect the Doppler velocity estimation by producing a blind zone which reduces the volume where velocity retrievals are meaningful. Cross-talk is determined by contributions from: 1) multiple scattering, 2) non-spherical atmospheric targets 3) ground clutter 4) instrument cross-talk induced by internal components of the radar hardware (radars designed for dual polarization typically aim for cross-polar isolation of -20 dB or better). It is believed that the MS is the key source of cross-talk for spaceborne millimeter radars. This is also observed by the lidar community (Hu et al.

[2001]). Another source of cross-talk can stem from non-spherical particles which tend to depolarize radar signal depending on their microphysical characteristics (among others: size, orientation, density, shape, phase (liquid,ice,...)). The blind layers are also introduced by the surface (Kobayashi et al. [2002]) which effects can be visible as interference signal on heights depending on the chosen T_{HV} or by depolarization signal returns due to the melting layer. Finally, the cross-talk can derive from different components of the radar hardware itself.

7.2.1 Generation of I and Q Voltage Pairs for PDPP

The Monte Carlo forward model allows to compute the ideal velocity spectra for the co-polar (correlated) and the cross-polar (uncorrelated) channels, S_{co} and S_{cx}. From these we can derive the ideal spectra in the H (first transmitted) and V (second transmitted) pulse as:

$$S_H(r) = S_{co}(r) + S_{cx}(r - \frac{cT_{HV}}{2}) \tag{7.2}$$

$$S_V(r) = S_{co}(r) + S_{cx}(r + \frac{cT_{HV}}{2}) \tag{7.3}$$

that accounts for the cross-talk between the two channels.

An example of copolar and cross-polar antenna pattern gain is shown on Fig. 7.2. The left panel illustrates the copolar HH signal with a visible pattern of the main beam of the antenna. The corresponding cross-polar HV signal is displayed on the right panel and the four cross-polar peaks located around the center of the figure

can be seen (Zrnic et al. [2010]).

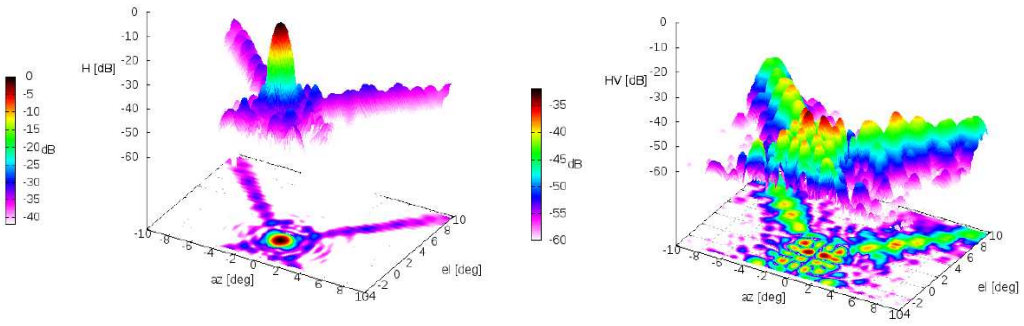

Figure 7.2: Example of copolar HH and cross polar HV gain for the antenna of the DWSR-5001/SDP/CE EEC radar system (from Frech et al. [2011]).

From the forward spectra the radar receiver model derives the signal fluctuations measured at the radar antenna port (I and Q time series) as in the case of the standard PP, including phase fluctuation and thermal noise (Zrnic' [1975]). The procedure of computation of I and Q for PDPP has to take into account the correct correlations of the I and Q components. It has been neatly described in recently published work of Battaglia et al. [2013]. As the orthogonal pulses consist of contributions from correlated (co-polar) and uncorrelated (cross-polar) returns this needs to be reflected in I and Q time series generation. First the I and Q time series of correlated spectrum are generated, using the same random number seed sequence:

$$V^H_{corr} = I^H_{corr} + jQ^H_{corr} \quad || \quad V^V_{corr} = I^V_{corr} + jQ^V_{corr} \tag{7.4}$$

After that two I and Q time series corresponding to uncorrelated components including noise powers for each channel are generated:

$$V^H_{unc} = I^H_{unc} + jQ^H_{unc} \quad || \quad V^V_{unc} = I^V_{unc} + jQ^V_{unc} \tag{7.5}$$

Then the correlated and uncorrelated sequences are summed up:

$$V^H = V^H_{unc} + V^H_{corr} \quad || \quad V^V = V^V_{unc} + V^V_{corr} \tag{7.6}$$

and finally the I and Q series are properly under-sampled to account for the correct sampling frequency PRF. These steps are illustrated in Fig 7.3).

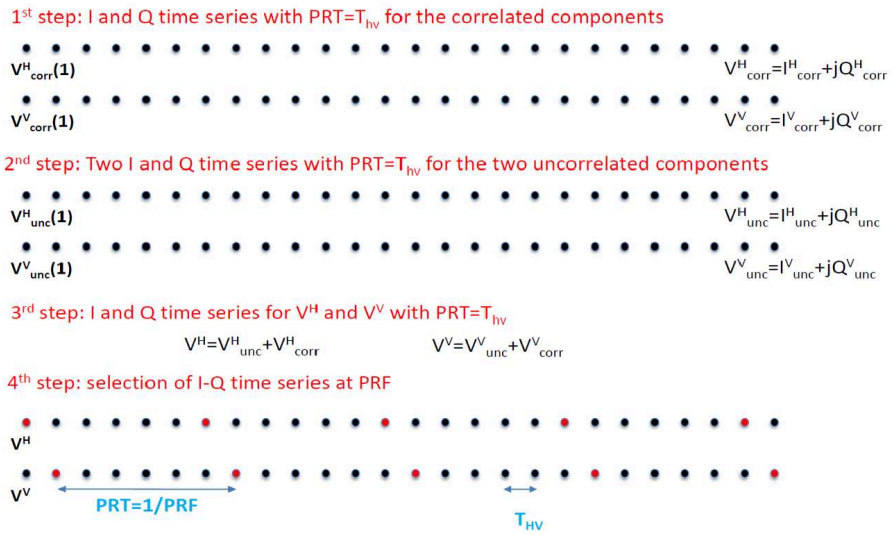

Figure 7.3: Schematic for the simulation of I and Q time series for PDPP Doppler radar, image from Battaglia et al. [2013].

7.2.2 Doppler Moments Estimation

The signal processing for PDPP has similar form to standard PP in a sense that it uses the correlation function, however the autocorrelation function between the following pulses is replaced with the cross-correlation function between orthogonally polarized signals (Pazmany et al. [1999]). Despite the use of separate receiver

channels for the H and V pulses, their phase coherency (due to the short interval between the H and V transmission) is used to extract the Doppler velocity. The cross-polarization function at lag $\tau = T_{HV}$ is defined as in Doviak and Sirmans [1973]; Pazmany et al. [1999]

$$\hat{R}_{HV}(r,\, T_{HV}) = \frac{1}{M}\sum_{i=1}^{M} V_H^*(r,\, t_i)\, V_V(r,\, t_i + T_{HV}) \tag{7.7}$$

where t_i is the sample time of the $i-$th pairs first sample, and the superscript $*$ represents a complex conjugate. M represents $M/2$ independent VH pairs combined with $M/2$ independent HV pairs. By inserting Eqs. (7.1) into Eq. (7.7) the estimated cross-correlation function reduces to:

$$\hat{R}_{HV}(r,\, T_{HV}) = \frac{1}{M}\sum_{i=1}^{M} V_{HH}^*(r,\, t_i)\, V_{VV}(r,\, t_i + T_{HV}) \tag{7.8}$$

due to the fact that only $V_{HH}(r)$ and $V_{VV}(r)$ are correlated.

The cross-correlation function $\hat{R}_{VH}(r,\, T_{HV})$ has a similar form, but has the opposite phase. The combination of both cross-polarization functions allows to estimate the Doppler moments as:

$$\hat{V}_D = \frac{\lambda}{4\pi T_{HV}} \arg\sqrt{\hat{R}_{HV}(T_{HV})\, \hat{R}_{VH}(T_{HV})} \tag{7.9}$$

$$\hat{\sigma}_D = \frac{\lambda}{2\pi\sqrt{2}T_{HV}} \sqrt{\log\left|\frac{\hat{R}_{HV}(T_{HV})}{\hat{R}_{HV}(0)}\right|} \tag{7.10}$$

7.3 EC-like System with Polarization Diversity

In this section the concept of EarthCARE-like radar, with an addition of polarization diversity is described (EC-PD). The addition of polarization diversity to an EC-like radar concept can reduce or fully eliminate the most difficult to mitigate contributor to the EarthCARE-CPR error budget; i.e.the aliasing of the velocity. We refer to an EarthCARE-like system as to a system with the same spacecraft altitude (400km), viewing geometry (nadir) and frequency of the radar (94 GHz).

This means that by changing the T_{HV} time (spacing between V and H pulses) we control the Nyquist velocity interval which is the direct cause of the aliasing of velocities in the EarthCARE configuration. For example, a short PDPP interval of $T_{HV} = 10\ \mu s$ produces a large Nyquist velocity interval of 75 ms^{-1}, which is large enough for velocity estimates in the atmosphere. However, the $T_{HV} = 40\mu$s, which produces a smaller Nyquist interval (18.75 ms^{-1}) has a better accuracy of velocity estimates as described in Sect.(7.3.3) and provides still a substantial improvement over the EC folding velocity. The optimal choice of T_{HV} is governed by three factors: the desirable folding velocity, the Doppler accuracy and the shift of interference signal - areas where Doppler estimates are noisy and reflectivity fields are affected by "ghost-like" features coming from interference.

The biggest issue with the PDPP concept is that the signal corresponding to each of the polarization diversity pair of pulses is a mixture of co-polar channel and a residual signal from the cross-polar channel, delayed by a value equal to T_{HV}

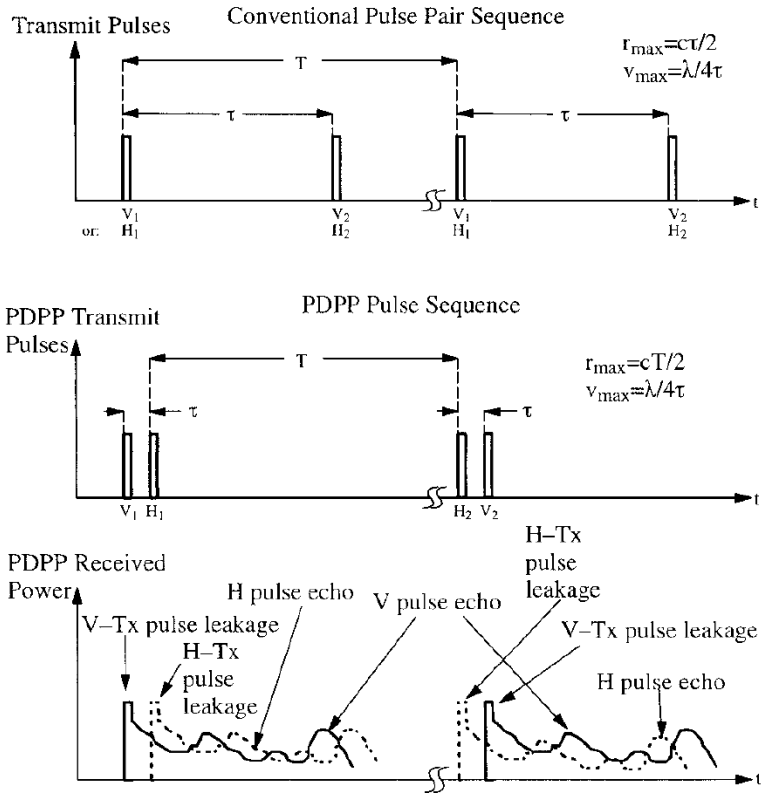

Figure 7.4: Comparison of a conventional pulse-pair technique (top panel) with PDPP technique (middle panel).Extracted from Pazmany et al. [1999].

(Eq. 7.3). Since the used model only accounts for spherical targets cross-talk of -20 dB has been used to account for the combined effect of atmospheric target depolarization and antenna cross-isolation (Battaglia et al. [2013]). On top of that the multiple scattering is the key source of cross-talk (Battaglia et al. [2013] and references therein). The effect of imperfect isolation of polarization between the co- and cross-polarized signals is depicted in Fig. 7.5. It is especially evident in reflectivity, where the effect causes areas of “fake” or “ghost” reflectivity (green curve at heights 9 to 12 km and red curve at 5 km to the surface). This is well visible in areas with weak copolar backscattering return or in areas where the copolar signal is produced

by weaker backscattering clouds. For the estimates of the mean Doppler velocity though, cross-talk does not produce such structures (cross-polarization interference does not bias the phase of cross correlation function, used to estimate mean Doppler velocity as shown in Pazmany et al. [1999]) and appears as increased noise in such regions - (e.g. see the Vel_{Dop}^{PDPP} for the region about 4.5 km height). The effect is further explained in the example scenario plots in Fig. 7.6. The signal from the co-polar channel is depicted in Fig. 7.6 a) with a signal received in the H channel depicted in Fig. 7.6 b) for $T_{HV} = 40\mu s$. The interference signal appears as a weaker image of the copolar backscattering return shifted up and down by 6 km. Also the surface effect comes into play in the described scenario and can be seen in Fig. 7.6 b) where the cross-polar surface return is visible at 6 km height (for the first 8 km of the scenario for the given T_{HV}).

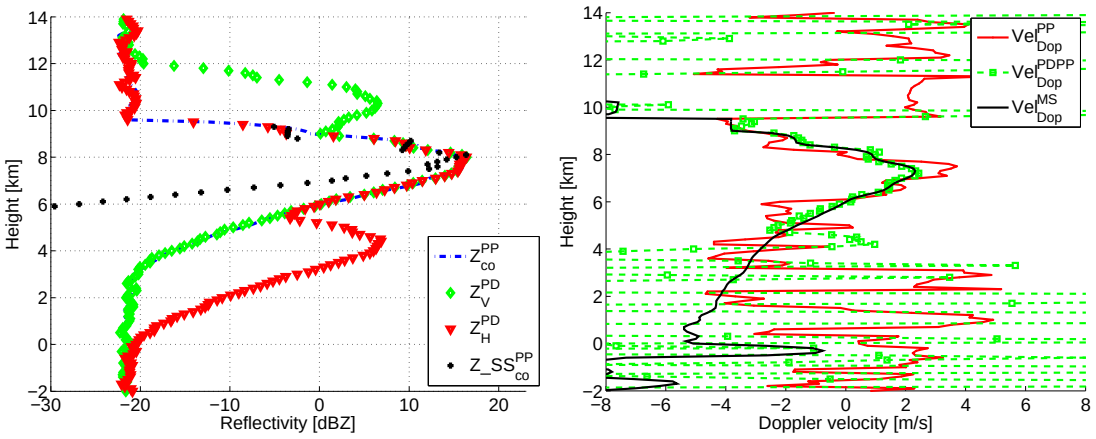

Figure 7.5: Example of cross talk between channels for reflectivity (left) and Doppler velocity for PDPP (right).

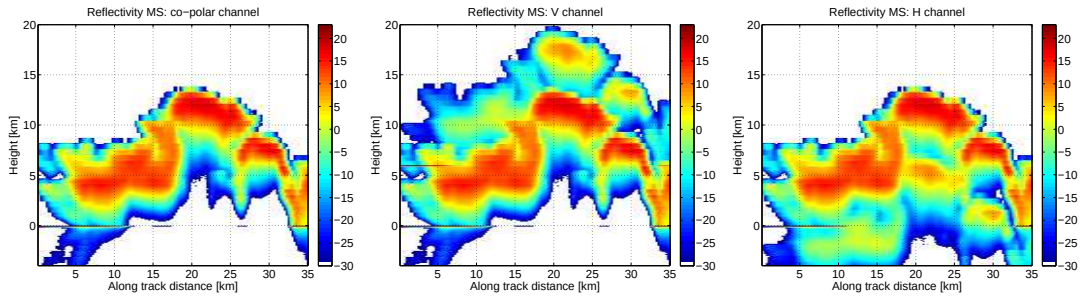

Figure 7.6: Example of cross-talk between channels seen in reflectivity, calculated for $T_{HV} = 40\ \mu s$ for 500 m integration. Reflectivity is shown for co-polar channel, V-channel and H-channel, respectively. The cross-talk is responsible for the areas of "fake" reflectivity fields, visible when all three channels are inter-compared.

7.3.1 Blind Layer

The operation of a Doppler radar in pulse-pair polarization diversity mode can result in the observation of a "blind layer" close to the surface (Kobayashi et al. [2002]). This is a consequence of the received radiation backscattered from the surface being depolarised, compared with the emitted pulses of radiation which are originally either horizontally or vertically polarised. The creation of a blind layer due to surface clutter is illustrated in Figure 7.7.

The ground surface is at range distance of ct_g from the radar, where t_g is the time taken for an emitted pulse to reach the ground. The times τ_p and T_s correspond to the pulse duration and the pulse-pair interval, respectively. The leading edge of the first pulse is backscattered at point G_1 on the ground. This backscattered signal will then contaminate the atmospheric return signal from the second pulse, which is scattered along the line A_1B_1. Similarly, the trailing edge of the first pulse is backscattered by the ground at point G_2, which then contaminates the second signal

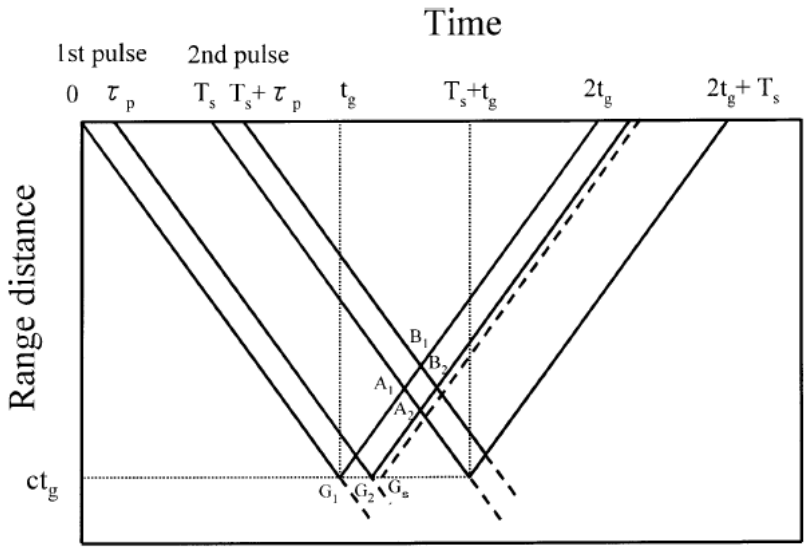

Figure 7.7: Range-time diagram illustrating the effect of ground clutter when operating a Doppler spaceborne radar in pulse-pair mode (taken from Kobayashi et al. [2002]).

along the line A_2B_2. All second pulse signals, which are scattered back towards the radar from within the rhombus shape $A_1A_2B_2B_1$, are therefore contaminated by ground clutter from the first pulse, thus creating in a nadir configuration a blind layer at the altitude $cT_s/2$ with range width $c\tau_p/2$. When deciding on the timings of the pulse-pair system, it is important to consider the range at which the blind layer will affect the measurements and ensure that it falls outside of the target range.

Similarly multiple scattering and interaction with non-spherical targets may cause considerable cross-talk that is seriously harmful in any Doppler analysis and that, in practise, is producing an additional blind zone which strongly reduces the 3D volume where retrievals are meaningful.

7.3.2 Interlaced Mode

Receiver channel cross-talk affected regions can be identified when a polarization diversity mode is interlaced with the conventional pulse-pair mode. Few methods are mentioned in the literature (Battaglia et al. [2013]; Kobayashi et al. [2002]; Pazmany et al. [1999]) with slightly different implementation. Here the method described in Battaglia et al. [2013] is followed. Every few HV pulses are interlaced with H (or V) pulse and using those single pulses conventional pulse-pair method is applied which allows to measure co-polar and cross-polar reflectivity signals. This in turn allows to calculate LDR as the ratio of the two; which can be used to identify MS affected regions. Moreover the use of an interlaced mode allows the identification of areas contaminated by polarization "ghost" signals. In fact, a ghost over co-polar signal ratio can be defined as:

$$\mathcal{G}(r) \equiv 10\ \log_{10}\left[\frac{Z_H(r) - Z_{HH}(r) + Z_V(r) - Z_{VV}(r)}{0.5\,(Z_{HH}(r) + Z_{VV}(r))}\right] \tag{7.11}$$

(where Z_H, Z_V, Z_{HH} and Z_{VV} are the reflectivities corresponding to the spectra S_H, S_V, $S_{co}(H)$ and $S_{co}(V)$ defined in Eq. (7.3), respectively). The assumptions here follows Battaglia et al. [2013] that areas with $\mathcal{G} < -3$ dB are "ghost-free".

The $\mathcal{G} < -3$ dB contour line has been plotted for CLDY 35 GHz Doppler velocity $(V_D)^{PDPP}$ in magenta in Fig. 7.8, where everything inside the magenta contour line is assumed to be ghost-free.

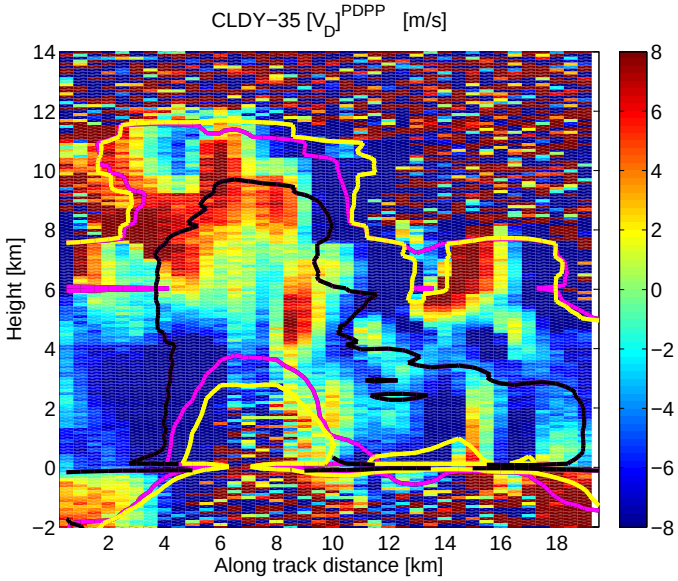

Figure 7.8: PDPP Doppler velocity for CLDY-35 configuration with SNR threshold = 6 dB (yellow contour line), LDR threshold of -15 dB (black) and No Ghost $\mathcal{G}(r)$ -3 dB (magenta) contour lines.

7.3.3 Theoretical Accuracy of Doppler Products

The theoretical accuracy of the Doppler velocities can be estimated using the following equation (Zrnic [1977]):

$$\begin{aligned} \mathrm{var}(V_D) &= \frac{\lambda^2}{16\pi^2 T_{HV}^2 \rho^2(T_{HV})} \Bigg\{ \frac{1-\rho^2(T_{HV})}{2M^2} \sum_{m=-(M-1)}^{M-1} \rho^2(mT_s)(M-|m|) + \\ &\frac{1}{2M\,(\mathrm{SNR})^2} + \frac{1}{\mathrm{SNR}\;M} \left[1 - (1-\frac{1}{M})\rho(2\,T_{HV})\delta_{T_s,T_{HV}} \right] \Bigg\} \end{aligned} \tag{7.12}$$

where M is the number of pulses, SNR is Signal-to-Noise Ratio and ρ is the normalised correlation function. The study by Zrnic [1977] shows that accuracy of mean Doppler velocities depend on T_{HV}.

The velocity accuracy for PDPP systems is shown in Fig. 7.9. The noise error

is relatively small for a wide range of the PRFs. The dependence of the velocity accuracy on the PDPP pulse pair interval T_{HV} is depicted in bottom panel of Fig. 7.9.

Two competitive effects are responsible for the shape of the accuracy curves:

1. The deterioration of correlation for large T_{HV};

2. Decrease in resolution of Doppler phase at small T_{HV}.

7.4 Evaluation of Future Radar Concepts for Convection

In general the polarization diversity pulse pair technique allows shorter along-track integration by supplying a larger number of correlated radar returns when compared to the standard pulse pair over the same distance. This allows to utilize integration of radar moments for 500 m along-track distance and thus to mitigate the averaging error discussed before. Based on analysis of ensemble of scenarios the PDPP pair interval T_{HV} has been chosen to 30 μ s, which is in agreement in visual justification based on Fig. 7.9.

7.4.1 MS Onset Identification Using LDR

Polarization diversity provides another method to identify regions affected by MS employing Linear Depolarization Ratio (LDR). LDR is defined as the ratio between

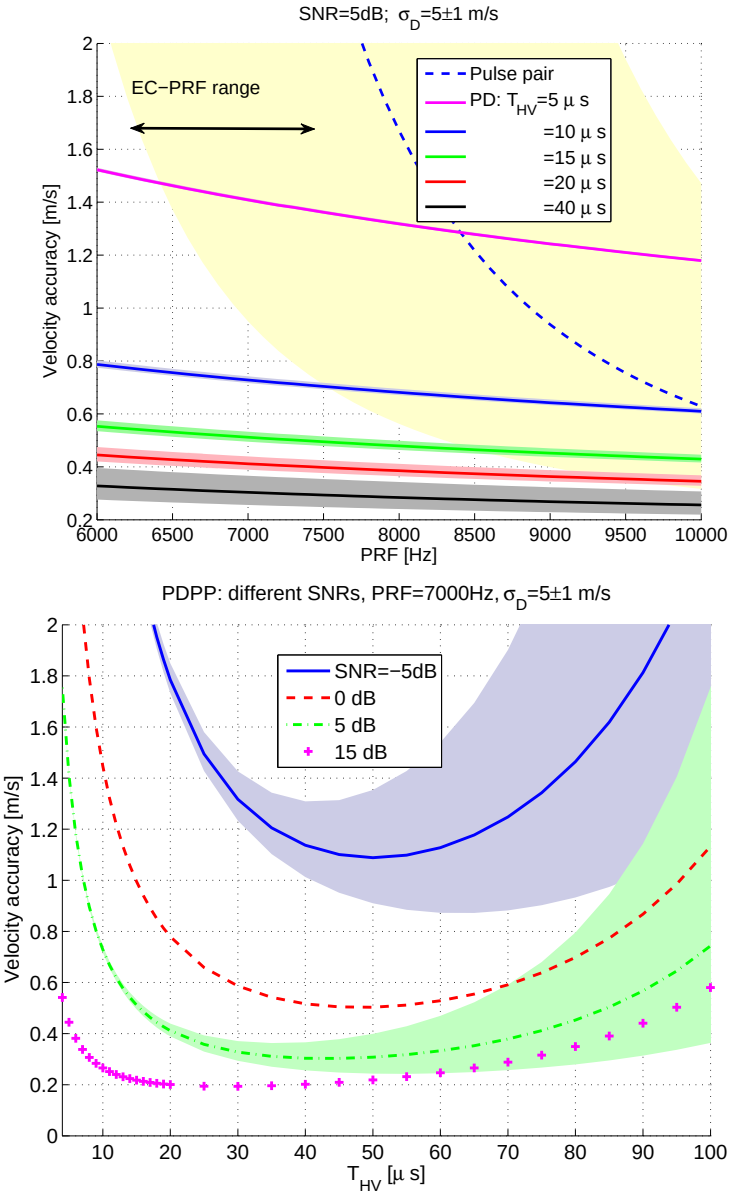

Figure 7.9: Top panel shows the theoretical Doppler accuracy for different PRFs and different T_{HV}.The bottom panel displays the dependance of the theoretical accuracy on T_{HV} for different SNR ratios for a system with PRF = 7000 Hz. The integration length is assumed to be 500 m. The same curves with the y-axis amplified by a factor 2.7 apply to the 35 GHz systems (Battaglia et al. [2013]).

the energy backscattered in the polarization orthogonal to the incident one and the

energy backscattered in the same polarization as the incident one:

$$LDR_V = \frac{Z_{HV}}{Z_{VV}} \tag{7.13}$$

Battaglia et al. [2006, 2007] demonstrated that MS effects manifest themselves by producing significant cross-talk. LDR_{MS} is much stronger than LDR_{SS} and provides clear signatures with high LDR (up to 0 dB) in regions where high MS enhancements are located. Such effects have been confirmed by airborne observations (Battaglia et al. [2010]).

LDR represents a valuable proxy of MS effects as it is possible to select a threshold of the LDR above which MS effects cause substantial change in the reflectivity. Utilizing the point-wise error map $\delta[V_D]_{MS}$ (point by point data comparison) for spectrum with isolated MS contribution as defined in Sect. 6.4.3 and plotting it versus LDR values displays strong correlation of LDR value and the resulting error variability (left panel in Fig. 7.10). By changing the LDR threshold value the Doppler accuracy and bias can be calculated. This can be seen in Fig. 7.10 where such errors are computed for the ACE-94 GHz configuration. Repeating this method for other spaceborne radar configurations provides the values summarized in Table. 7.1. The second column shows the selected LDR threshold in dB, based on the optimal performance for accuracy improvement and ratio of screened out data points; the third column displays the standard deviation of error due to the MS $\delta[V_D]_{MS}$ after the LDR threshold has been applied to the whole dataset. The last

column shows the percentage of pixels flagged out after the LDR MS threshold has been applied.

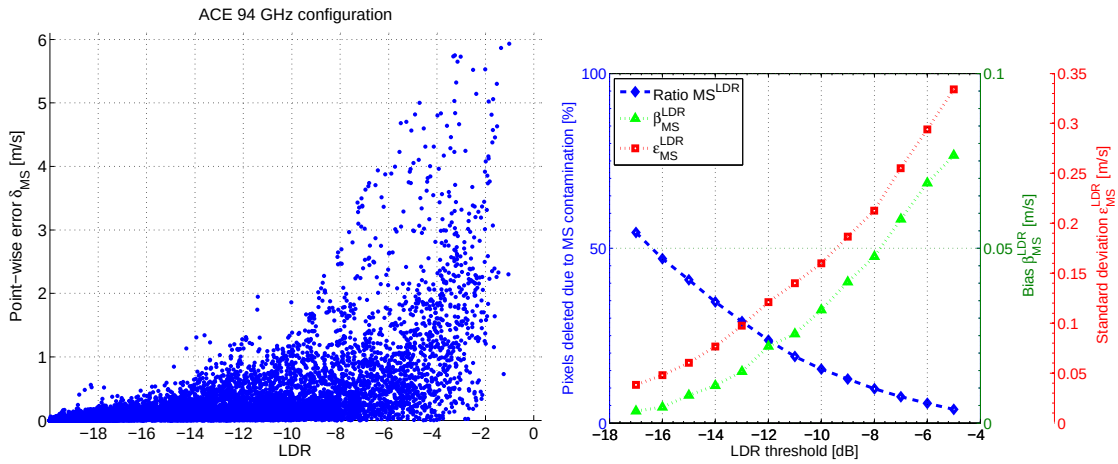

Figure 7.10: Left panel:the LDR threshold used as indication of multiple scattering presence for ACE 94 GHz configuration. Right panel displays the Doppler velocity accuracy for different LDR thresholds. Blue line shows the ratio of pixels deleted due to MS threshold value to the initial number of pixels, data (in %). Red line shows the standard deviation ϵ_{MS} [m/s] and green line displays the velocity bias (β_{MS} [m/s].

Table 7.1: LDR threshold for multiple scattering onset identification

Configuration	LDR threshold [dB]	std ϵ_{MS}^{corr}	MS flag [%]
EC-PD	-11	0.29	29
ACE-94	-11	0.14	19
10m-94	-8	0.12	2
CLDY-35	-15	0.41	39
ACE-35	-11	0.28	8
10m-35	-8	0.11	1

When selecting the LDR threshold of -11 dB the resulting standard deviation of error due to MS ϵ_{MS} for EC-PD equals 0.29 m/s with the 29 % of pixels flagged out from the dataset. The same LDR threshold for ACE configuration show that the

accuracy is improved ($\epsilon_{MS}^{corr} = 0.14$ m/s) with only 19 % of pixels flagged out. The LDR threshold of -8 dB shows that the 10 m antenna radar concept is marginally affected by MS. Indeed the thresholding eliminates only very few outliers points (2 % of the pixels). Both large antenna radar systems show that the MS will have a little effect on their total accuracy. The most severely affected concept by MS is CLDY-35 where the chosen LDR threshold is the lowest (-15 dB) which results in large number of pixels being flagged out (39 %). After flagging out these points the standard deviation due to MS effects is reduced to 0.41 m/s.

7.4.2 NUBF Error Mitigation Using Along-track Reflectivity Gradient

The method described in Sect. 6.5.2 is used here to find the correction coefficients α for the five remaining configurations, whose specifics are listed in Table. 3.2. The derived values are included in Table. 7.2. The theoretical α_{linear} and α_{step} are provided for a reference.

Table 7.2: NUBF correction coefficient α $[ms^{-1}(dBZkm^{-1})^{-1}]$

Config.	EC	CLDY-35	ACE 94	ACE 35	10m 94	10m 35
α	**0.18**	**1.26**	**0.05**	**0.36**	**0.01**	**0.08**
α_{linear}	**0.16**	**1.18**	**0.04**	**0.30**	**0.01**	**0.08**
α_{step}	**0.22**	**1.57**	**0.06**	**0.40**	**0.01**	**0.10**

The calculated coefficient α is utilized to correct the NUBF error for the whole dataset when the NUBF error is isolated (as in Sect. 6.5.3) to examine the contri-

bution of NUBF error. The calculated values are included in Table. 7.3. After the correction the NUBF contribution to the accuracy of all 94 GHz radar systems is less than 0.4 m/s with the large antenna radar being the least affected (0.17 m/s). The same antenna size as for a W-band (94 GHz) radar results in a beamwidth 2.7 larger for a K_a-band (35 GHz) radar. This larger beamwidth cause larger velocity errors due to NUBF effects. As a result the 35 GHz radars tend to be more heavily affected by NUBF than the same antenna size 94 GHz counterparts, which is clearly seen when the initial values of standard deviation of NUBF error are compared for corresponding 94 and 35 GHz system (ϵ_{INIT}). In fact the radar with the largest beamwidth - CLDY 35 GHz- is the most severely affected by NUBF. On the opposite side is the 10m 94 GHz concept for which the initial accuracy before NUBF correction is already fairly good, this is reflected in a standard deviation value of $\delta[V_D]_{NUBF}$ of 0.24 m/s and in the small value of the correction coefficient α_{10m-94} = 0.01. However, the 35 GHz radars tend to penetrate down into deep convective systems (Battaglia et al. [2013]).

Table 7.3: NUBF correction coefficient α and resulting velocity standard deviation ϵ and bias β of error due to the isolated NUBF effect $\delta[V_D]_{NUBF}$

configuration	α	std ϵ_{INIT}	std ϵ^{corr}_{NUBF}	bias β_{INIT}	bias β^{corr}_{NUBF}
EC	0.18	**2.05**	**0.36**	-0.03	-0.03
ACE-94	0.05	**0.71**	**0.22**	0.00	0.01
10m-94	0.01	**0.24**	**0.17**	0.00	0.01
CLDY-35	1.26	**5.97**	**0.54**	0.03	0.02
ACE-35	0.36	**2.68**	**0.58**	-0.03	0.00
10m-35	0.08	**0.82**	**0.28**	0.00	0.01

7.5 Total Error Budget for PDPP Configurations

The analysis of the whole dataset for the six polarization diversity configurations is first restricted by SNR thresholding and by deleting pixels affected by the surface clutter (i.e. below 0.3 km). This is when the first "initial" standard deviation and bias are calculated as point wise error $\delta[V_D]_{INITIAL}$:

$$\delta[V_D]_{INITIAL} = {}^{MS}(V_D)^{mov.}_{CONF} - {}^{SS}(V_D)^{stat.}_{forw} \tag{7.14}$$

for each of the configurations (labeled "conf" in ${}^{MS}(V_D)^{mov.}_{CONF}$). Then the data are restricted to areas which are $MS-$free (the onset of MS contamination is calculated using the LDR threshold). The error after MS onset correction is calculated from $\delta[V_D]^{corr}_{MS}$. After that the NUBF effect is reduced by applying the reflectivity gradient technique, and the consequent error is labeled as $\delta[V_D]^{corr}_{NUBF}$. The values of the standard deviation of these errors for 500 m integration and SNR threshold of 6 dB are reported in Table. 7.4. The velocity biases β for the point-wise errors are small and oscillate around 0 value.

The analysis restricted to regions which are $MS-$free and ghost-free is coined as NoGhost (i.e. $(V_D)^{PDPP}_{NoGhost}$). For those results, summarized in Tables (7.4 - 7.5) the MS and "ghost" corrections are applied together (and shown every second row).

The same analysis is then repeated for a SNR threshold of 0 dB. The threshold of 6 dB used in the analysis was dictated by the consequence of the SNR threshold used in previous chapter. However the PDPP method performs better than PP even

Table 7.4: Velocity accuracy of specified configurations, calculated for whole dataset for SNR threshold of 6 dB and 500 m along-track integration.

Conf/LDR	velocity	std INITIAL	std MS corr	std. NUBF corr
EC-PD	$(V_D)^{PDPP}$	**2.02**	**1.97**	**0.45**
-11	$(V_D)^{PDPP}_{NoGhost}$	**2.02**	**1.72**	**0.42**
ACE-94	$(V_D)^{PDPP}$	**0.89**	**0.75**	**0.31**
-11	$(V_D)^{PDPP}_{NoGhost}$	**0.89**	**0.64**	**0.29**
10m- 94	$(V_D)^{PDPP}$	**0.43**	**0.42**	**0.25**
-8	$(V_D)^{PDPP}_{NoGhost}$	**0.43**	**0.29**	**0.22**
CLDY-35	$(V_D)^{PDPP}$	**6.10**	**6.60**	**1.39**
-15	$(V_D)^{PDPP}_{NoGhost}$	**6.10**	**6.24**	**1.15**
ACE-35	$(V_D)^{PDPP}$	**2.97**	**2.95**	**0.80**
-12	$(V_D)^{PDPP}_{NoGhost}$	**2.97**	**2.42**	**0.64**
10m-35	$(V_D)^{PDPP}$	**1.13**	**1.08**	**0.64**
-8	$(V_D)^{PDPP}_{NoGhost}$	**1.13**	**0.78**	**0.37**

Table 7.5: Velocity accuracy of specified configurations, calculated for whole dataset for SNR threshold of 0 dB and 500 m along-track integration.

Conf/LDR	velocity	std INITIAL	std MS corr	std. NUBF corr
EC-PD	$(V_D)^{PDPP}$	**2.38**	**2.28**	**0.54**
-11	$(V_D)^{PDPP}_{NoGhost}$	**2.38**	**1.79**	**0.45**
ACE-94	$(V_D)^{PDPP}$	**1.05**	**0.88**	**0.40**
-11	$(V_D)^{PDPP}_{NoGhost}$	**1.05**	**0.66**	**0.31**
10m- 94	$(V_D)^{PDPP}$	**0.61**	**0.59**	**0.36**
-8	$(V_D)^{PDPP}_{NoGhost}$	**0.61**	**0.31**	**0.23**
CLDY-35	$(V_D)^{PDPP}$	**6.88**	**7.58**	**1.68**
-15	$(V_D)^{PDPP}_{NoGhost}$	**6.82**	**6.62**	**1.28**
ACE-35	$(V_D)^{PDPP}$	**3.37**	**3.30**	**0.98**
-12	$(V_D)^{PDPP}_{NoGhost}$	**3.37**	**2.48**	**0.69**
10m-35	$(V_D)^{PDPP}$	**1.65**	**1.56**	**0.97**
-8	$(V_D)^{PDPP}_{NoGhost}$	**1.65**	**0.79**	**0.39**

for lower SNR regions and the SNR threshold can be lowered to a value of 0 dB. The calculations for this threshold are summarized in Table. 7.5.

To visualize differences of the discussed configurations the final mean Doppler velocity panels after all corrections and resulting point-wise error maps (final product minus reference) are plotted for case study scenario for 94 GHz configurations in Fig. 7.11 and for 35 GHz in Fig. 7.12. The colour-scale of the plots is standardized to illustrate the differences. The case study epitomizes the numbers is included in the tables. The 5 m antenna provides a big improvement over the smaller ones, while the large antenna concept allows a few more km of penetration inside the convective core thanks to the much lower multiple scattering contamination level. For EC-PD and CLDY-35 it also confirms previous findings of Battaglia et al. [2013] that the advantage of deeper penetration of the K_α-band in convective core is partially lost due to a similar level of MS contamination.

7.6 Conclusions

Polarization diversity provides extended Nyquist velocity (folding velocity) therefore is a true improvement for the aliasing problem, compared to conventional pulse-pair systems. The application of PDPP reduces the uncertainty in the Doppler velocity estimates due to the higher sampling rate of fast decorrelating signals of millimeter spaceborne systems.

As expected the 35 GHz channel penetrates a larger portion of deep convective

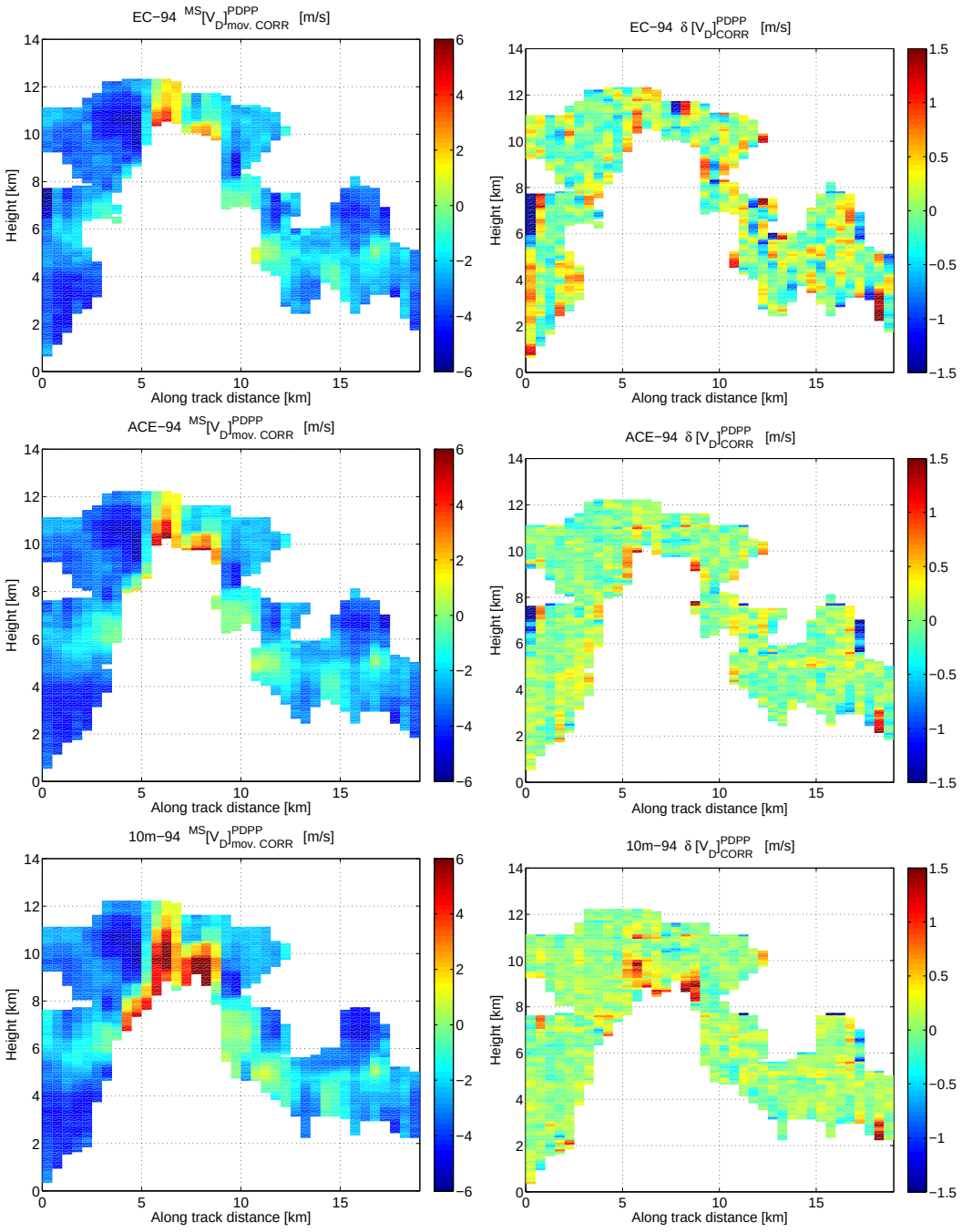

Figure 7.11: Plots displayed for the case study. Left column: mean Doppler velocity after MS and NUBF correction for different 94 GHz configurations: EC (top), ACE (middle), large antenna concept (bottom). Right column: corresponding final pointwise error for the three configurations, respectively.

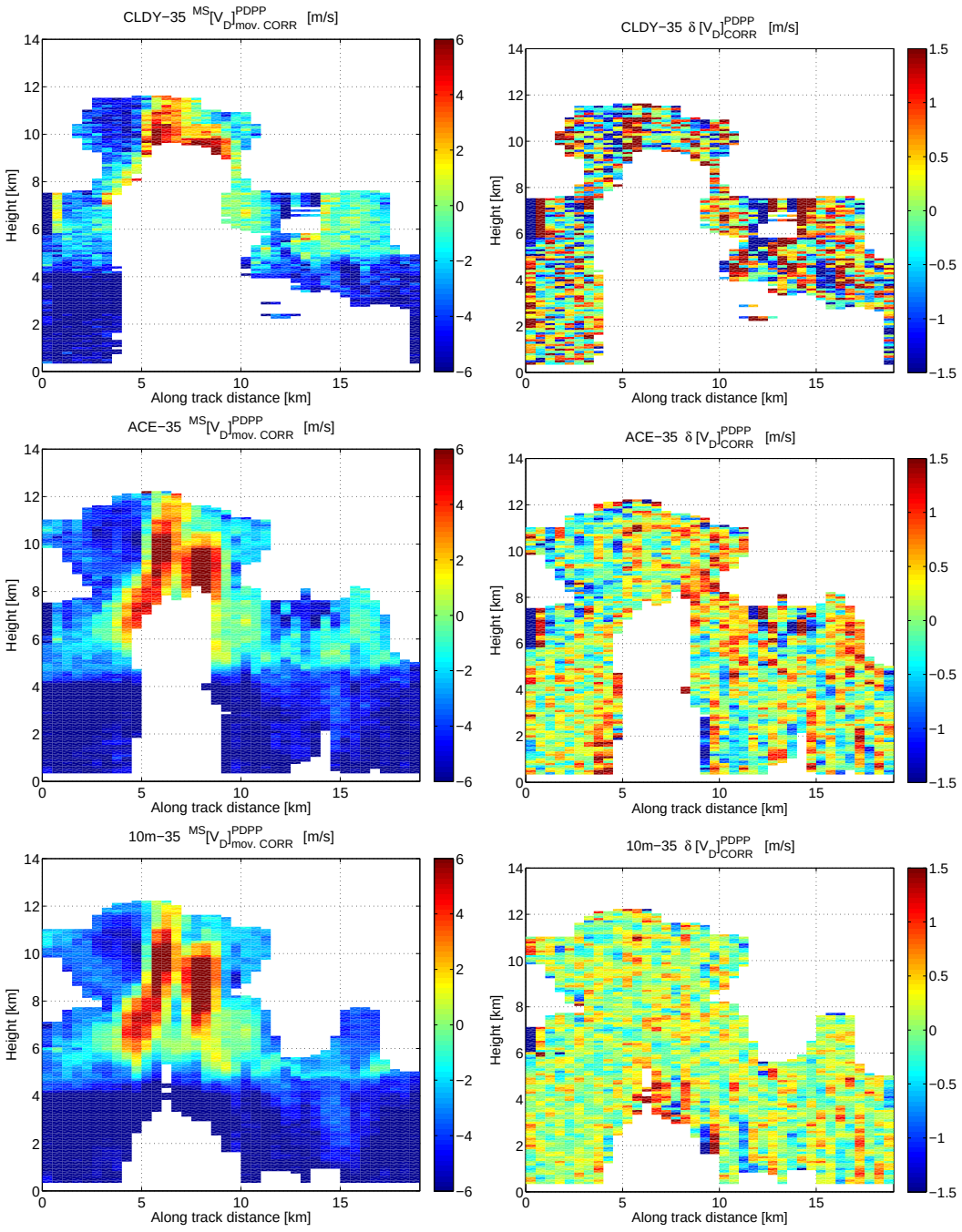

Figure 7.12: Plots displayed for the case study. Left column: mean Doppler velocity after MS and NUBF correction for different 35 GHz configurations: CLDY (top), ACE (middle), large antenna concept (bottom). Right column: corresponding final point-wise error for the three configurations, respectively.

systems compared to 94 GHz, however the 35 GHz systems are heavily affected by NUBF effects which bias the velocity estimates in regions of strong along track reflectivity gradients. The 94 GHz systems have smaller footprints for the same antenna size compared to 35 GHz, thus are more adequate for fine structure of convective cells. Those systems are ideal for the upper part of convective cores due to combined effect of MS contamination and signal attenuation.

Receiver channel cross-talk regions can be identified when a polarization diversity method is interlaced with the usual pulse-pair method. It also enables estimation of LDR which can be used for MS onset identification. Presence of interference "ghosts" producing blind zones can be minimized by screening out regions using the ghost over co-polar signal ratio of -3 dB. This further improves the accuracy of all systems.

After the corrections methods for MS and NUBF effects are applied the scientific requirement of 1 m/s accuracy for 500 m integration are possible for all W-band configurations described. This includes relatively small antennas of 2.5 m currently being deployed in space.

The large antenna along with described correction techniques will help to minimize the effects of non-uniform beam filling and multiple scattering and the polarization diversity can solve the problem of aliasing of velocities.

Chapter 8

Conclusions

The potential of millimeter-wavelength cloud profiling Doppler radars for measurements in deep convection has been investigated in the thesis. It also discusses the comprehensive total error budget analysis for the EarthCARE-CPR Doppler velocity estimates in deep convection scenarios.

In Chapter 4 the NASA high-altitude ER-2 aircraft X and W-band Doppler radar data were used in order to investigate the naturally occurring variability of Doppler velocities in convection as well to examine the vertical and horizontal reflectivity gradients. In the small investigated dataset from the CRYSTAL-FACE campaign updraught velocities of 25 m/s were recorded. However, updraughts exceeding 30 m/s are reported in the literature (Heymsfield et al. [2010]). In addition, along-track reflectivity gradients of 30 dBZ/km were measured by both 9.6 and 94 GHz radars. These extreme values for vertical velocities and horizontal reflectivity gradients already pinpoint two challenges associated with spaceborne Doppler radar observations of deep convective clouds (aliasing of velocities and NUBF effects).

A rigorous assessment of Doppler velocity estimates from LEO platforms for deep convective cores is only possible via notional studies. For this purpose an end-to-end Doppler radar simulator has been developed, tested and applied to 3D scenarios simulated by cloud resolving models. Chapter 5 describes the end-to-end Doppler radar simulator with focus on its forward component, simulation of different spectra, and finally the developed signal processing module to account for the specific radar instrument configuration.

EarthCARE-CPR is expected to deliver a new dimension in atmospheric measurements for weak dynamic systems such as stratiform and cirrus clouds (e.g. ice sedimentation regimes), where the pulse-pair technique performs well in case where there are not many strong reflectivity gradients (Kollias et al. [2014]). It will be a valuable demonstrator of technology as the first spaceborne atmospheric Doppler radar. Velocity measurements in deep convective systems will be more challenging.

The performance of the EarthCARE Cloud Profiling Radar in deep convection has been analysed in depth in this work (Chapter 6), first by a selected case study, and then followed by an analysis of ensemble of simulations. The different sources of error were separated and quantified, thanks to the flexibility of the end-to-end simulator to produce all kinds of different Doppler spectra. In order to improve the instrument performance a methodology to mitigate two of a main contributors to the EC-CPR error budget: the effects of multiple scattering and non-uniform beam filling effects has been developed. It has been found that the cumulative integrated

reflectivity can be used as a reliable proxy for the identification of regions affected by multiple scattering for deep convective cores. For the EarthCARE CPR value of 41.5 dBZ_{int} was selected based on a statistical analysis and purely on reflectivity profile values (i.e. observations that will be available from the EC-CPR) as a threshold value to identify pixels contaminated by MS. Based on our set of simulations this entails roughly a 30 % reduction in the observations when producing the quality controlled Doppler product. Similarly it has been shown that the error due to Non-Uniform Beam Filling effect can be reduced by applying the along-track reflectivity gradient method. The derived correction coefficient relating along-track reflectivity gradients to the NUBF velocity bias equals to 0.18 m/s /dBZ/km for EC-CPR which agrees well with the recent findings of Sy et al. [2013] made for stratiform rain and snowstorm with moderate convection and with a significantly different simulation method. As the method uses reflectivity to calculate the gradients, reflectivity with good along-track resolution should be provided, especially in convection. The effectiveness of the NUBF correction method highly depends on whether or not the Doppler spectrum used has been affected by velocity folding. If the Doppler spectrum contains aliased regions, the benefit of NUBF correction is not significant. On the other hand, for properly de-aliased Doppler spectrum, the NUBF correction works very well (i.e. for ideally de-aliased spectra and for isolated NUBF effects, the initial accuracy is improved from 2.05 m/s to 0.35 m/s).

Apart from MS and NUBF errors, velocity aliasing especially related to the

low PRF mode envisaged for EC-CPR operations, has been identified as the main contributor to the EC-CPR error budget. The Development of a reliable de-aliasing method poses still a big challenge. As a result, the CPR is expected to have a better performance at high latitudes (where higher PRF will slightly reduce the effect of aliasing) compared to the tropics and the mid-latitudes. Our findings demonstrate that achieving the mission′ s scientific requirements for Doppler measurements in convection (1 m/s for 1 km along-track integration) will be extremely challenging. The accuracy of Doppler velocities after the MS and NUBF corrections (however without mis-pointing errors assumed to be in the order of $\sim$ 0.3 m/s) will be in order of 2.7 m/s (at 6100 Hz PRF) and 1.57 m/s (at 7500 Hz PRF), respectively. Even with perfect de-aliasing our results show that the accuracy of EC-CPR will be 1.74 m/s (at 6100 Hz PRF) and 1.07 m/s (at 7500 Hz PRF), respectively. It seems unrealistic to use the lowest operational PRFs for the deep convection regions as this introduces large uncertainty. The upper limitation imposed by the height of the troposphere combined with the short de-correlation time associated to 94 GHz radars on LEO platforms and the need for short along-track integration length to retain the fine structure of convective clouds makes the use of single-polarization method not ideal. Due to the fine-scale of convection longer integration lengths are also not beneficial because they introduce an averaging error that may harm the overall accuracy.

As proposed for several space missions targeting convection (ACE, CLDY), be-

cause of its limited penetration in deep convection (attenuation) and due to multiple scattering often found in convective cores, 94-GHz radar systems can be used to characterise the upper part of convective cores only. A better characterization of convective profiles requires a second, lower frequency radar (e.g. 35 GHz). However, a 35 GHz radar system with the same 2.5 m antenna size can provide only a slight improvement over a 2.5 m antenna 94 GHz system due to a comparable height of the MS affected regions but stronger NUBF effects (see also Battaglia et al. [2013]).

Bearing in mind that the aliasing is potentially the main cause of uncertainty in deep convective observations for the EarthCARE CPR the polarization diversity has been proposed for future radar systems targeting convective clouds. Such a technique enables shorter along-track integration of Doppler moments as compared to the conventional pulse pair technique. This is essential in deep convection as it not only provides the Doppler products with a better resolution but also the uncertainty introduced by averaging error can be avoided. The polarization diversity is the key method to mitigate aliasing related errors and beneficial to achieve good accuracy.

The study conducted for different antenna size radars unequivocally shows that the largest improvement is gained from having a large antenna, a result which certainly has not been unexpected. For example, the large antenna PDPP concept is very lightly affected both by the MS errors and by NUBF errors. Good accuracy can also be achieved by a 5 m elliptical antenna (like in the ACE configuration) at W-band in combination with polarization diversity capabilities. This makes concepts

like those proposed for ACE extremely appealing for convective studies.

One of the drawbacks for the polarization diversity processing - introduction of polarization "ghosts", can be partially mitigated by the introduction of an interlaced mode within polarization diversity. This further improves the accuracy of the PDPP Doppler products and provides useful tools to flag out regions affected by multiple scattering.

Considering the results presented in this thesis, there is scope for further investigation. The convective systems extracted from CRM models which were used as input to the radar simulator in this thesis represent only a small subset of possible convective systems encountered globally. The convective systems during TC4 campaign, used as a source for CRM model data, did not contain extreme convective cores if compared to those referred in the literature, which could lead to even larger contribution of aliasing effects to the EarthCARE accuracy. As is often the case, the study could take advantage from producing more simulations with different microphysical assumptions both for the input CRM data and for the end-to-end radar simulator. Furthermore, the study would benefit from other locations and types of environment where deep convection was triggered (i.e. land, sea-breeze type convection).

Continuing along these lines, the main area for future work exists in the development of a reliable technique for de-aliasing of the Doppler velocities. This would be extremely beneficial for the upcoming EarthCARE mission. Another possibility for

improvement would be to investigate thresholds of cumulative integral of reflectivity to be used as the operational threshold of multiple scattering onset for shallow convection.

To summarise, two key results can be inferred for the design of future millimeter-wavelength spaceborne radar concepts for convection-oriented studies. A large antenna will help to minimize the effects of non-uniform beam filling and multiple scattering, and the polarization diversity can solve the problem of aliasing of velocities.

References

ACE-Science-Group, 2010: Aerosol, Cloud and Ecosystems (ACE) Proposed Satellite Mission. Tech. rep., NASA Publication Division. Available at http://dsm.gsfc.nasa.gov/ace/documents/. 3

Alfieri, L., P. Claps, and F. Laio, 2010: Time-dependent Z-R relationships for estimating rainfall fields from radar measurements. *Nat. Hazards Earth Syst. Sci.*, **10**, 149 158. 24

Amayenc, P., J. Testud, and M. Marzoug, 1993: Proposal for a spaceborne dual-beam rain radar with Doppler capability. *J. Atmos. Ocean Technol.*, **10 (3)**, 262–276. 9, 18, 21, 35

Arakawa, A., 2004: The cumulus parameterization problem: Past, present, and future. *J. Climate*, **17**, 24932525. 4, 13

Baptista, J. P. V. P., 2004: EarthCARE- Earth Clouds, Aerosols and Radiation Explorer, Technical and Programmatic Annex. Tech. rep., ESA Publication Division. Available at http://www.esa.int/esaLP/LPearthcare.html. 46, 47, 48

Baptista, P. and W. Leibrandt, 2001: EarthCARE Earth Clouds, Aerosols and Radiation Explorer, reports for assessment - the five candidate earth explorer core missions. Tech. Rep. ESA SP-1257(1), European Space Agency, Nordwijk (NL). ISBN 92-9092-628-7. 50

Battaglia, A., M. O. Ajewole, and C. Simmer, 2006: Evaluation of radar multiple scattering effects from a GPM perspective. Part I: model description and validation. *J. Appl. Meteorol.*, **45 (12)**, 1634–1647. 75, 163

Battaglia, A., M. O. Ajewole, and C. Simmer, 2007: Evaluation of radar multiple scattering effects in CloudSat configuration. *Atmos. Chem. Phys.*, **7**, 1719–1730. 111, 115, 147, 163

Battaglia, A., T. Augustynek, S. Tanelli, and P. Kollias, 2011: Multiple scattering identification in spaceborne w-band radar measurements of deep convective cores. *JGR-Atmospheres*, **116 (D19201)**. 21, 111, 112, 117, 118, 121

Battaglia, A., J. M. Haynes, T. L'Ecuyer, and C. Simmer, 2008a: Identifying multiple-scattering affected profiles in CloudSat observations over the Oceans. *J. Geophys. Res.*, **113, D00A17**, doi:10.1029/2008JD009960. 112

Battaglia, A., N. Humpage, P. Kollias, and S. Tanelli, 2012: Report on capability of atmospheric parameter retrieval and modelling for WIde-Swath space-borne atmospheric Doppler Radars. Tech. rep., University of Leicester, McGill University, UCLA JIFRESSE. ESA ITT AO/1-6661/11/NL/LvH. 18, 20

Battaglia, A., S. Kobayashi, S. Tanelli, E. Im, and C. Simmer, 2008b: Multiple scattering effects in pulsed radar systems: an intercomparison study. *J. Atmos. Ocean Technol.*, **25 (9)**, doi: 10.1175/2008JTECHA1023.1. 111

Battaglia, A. and S. Mantovani, 2005: Forward Montecarlo computations of fully polarized microwave radiation in non isotropic media. *J. Quant. Spectrosc. Radiat. Transfer*, **95 (3)**, 285–308. 75, 80

Battaglia, A. and S. Tanelli, 2011: DOppler MUltiple Scattering simulator. *IEEE Trans. Geosci. Remote Sens.*, **49 (1)**, 442–450, doi:10.1109/TGRS.2010.2052818. 75, 113

Battaglia, A., S. Tanelli, S. Kobayashi, D. Zrnic, R. J. Hogan, and C. Simmer, 2010: Multiple-scattering in radar systems: A review. *J. Quant. Spectrosc. Radiat. Transfer*, **111**, 917–947, doi:10.1016/j.jqsrt.2009.11.024. 65, 111, 163

Battaglia, A., S. Tanelli, and P. Kollias, 2013: Polarization diversity for milimeter space-borne Doppler radars: an answer for observing deep convection? *J. Atmos. Oceanic Technol.*, **13**. xiv, xv, 1, 39, 75, 146, 151, 152, 155, 159, 162, 166, 169, 177

Battan, L. J., 1973: *Radar Observation of the Atmosphere*. University of Chicago Press, Chicago and London. 37, 95

Benham, F. C., H. L. Groginsky, A. S. Soltes, and G. A. Works, 1972: Pulse pair

estimation of doppler spectrum parameters. Tech. Rep. Final Rep., Contract F-19628-71-C-0126, Raytheon Co., Wayland, Mass. 75

Bennartz, R., P. Joe, U. Loehnert, J. Koskinen, G. Skofronick-Jackson, and D. Vane, 2011: Report on the Third International Workshop on Space-based Snowfall Measurement 30 March - 2 April 2011, Grainau, Germany, 30 pages. Tech. rep. Available from http://www.isac.cnr.it/ ipwg/meetings/grainau-2011/iwssm_3_report_final.pdf. 54

Bouniol, D., A. Protat, A. Plana-Fattori, J.-P. Vinson, M. Giraud, and N. Grand, 2008: Comparison of airborne and spaceborne 95 GHz radar reflectivities and evidence of multiple scattering in CloudSat measurements, . *J. Atmos. Ocean Technol.*, **25 (11)**, 1983–1995, dOI: 10.1175/2008JTECHA1011.1. 111

Bringi, V. N. and V. Chandrasekar, 2001: *Polarimetric Doppler Weather Radar, Principles and applications*. Cambridge University Press, pp 636. 145

Cecil, D. J., S. J. Goodman, D. J. Bocippio, E. J. Zipser, and S. W. Nesbitt, 2005: Three years of TRMM precipitation features. Part I: Radar, radiometric, and lightning characteristics. *Mon. Wea. Rev.*, **133**, 543566. 49

Chae, J. H., D. L. Wu, W. G. Read, and S. C. Sherwood, 2011: The role of tropical deep convective clouds on temperature, water vapor, and dehydration in the tropical tropopause layer (TTL). *Atmos. Chem. Phys.*, **11**, 3811–3821, doi:10.5194/acp-11-3811-2011. 16

Chevalier, F. L., 2002: *Principles of Radar and Sonar Signal Processing*. Artech house. 23

CLDY-Proposal, 2011: Report on CLDY - the climate dynamics mission proposal for the ESA-ISS climate change. Tech. rep., CLDY Science Team. 2011/11/04. xiv, 53, 148

CloudSat Online, D., 2013: Spacecraft and Data Status Update. Accessed: 2013-06-25, http://http://www.cloudsat.cira.colostate.edu/, accessed: 2013-06-25. 44

Corti, T., et al., 2008: Unprecedented evidence for deep convection hydrating the tropical stratosphere. *Geophys. Res. Lett.*, **35 (L10810)**. 16

Craig, G. C. and A. Dörnbrack, 2008: Entrainment in cumulus clouds: what resolution is cloud-resolving? *J. Atmos. Sci.*, **65**, doi: http://dx.doi.org/10.1175/2008JAS2613.1. 77

Delanoë, J., A. Protat, D. Bouniol, A. Heymsfield, A. Bansemer, and P. Brown, 2007: The characterization of ice cloud properties from doppler radar measurements. *J. Appl. Meteorol. Climatol.*, **46**, 1682–1698, doi: http://dx.doi.org/10.1175/JAM2543.1. 19

Doviak, R. J. and D. Sirmans, 1973: Doppler radar with polarization diversity. *J. Atmos. Sci.*, **30**, 737–738. 145, 153

Doviak, R. J. and D. S. Zrnic, 1984: *Doppler Radar and Weather Observations*. Academic Press. 34, 39, 92

Doviak, R. J. and D. S. Zrnić, 1993: *Doppler Radar and Weather Observations*. Academic Press, INC., second edition. 38

Dufresne, J.-L. and S. Bony, 2008: An Assessment of the Primary Sources of Spread of Global Warming Estimates from Coupled AtmosphereOcean Models. *J. Climate*, **21**, 51355144. ix, 6

EarthCARE Mission Advisory Group, 2006: Earthcare mission requirement document. Tech. rep., ESA Publication Division. Http://esamultimedia.esa.int/docs/EarthObservation/EarthCARE_MRD_v5.pdf. 17, 48

ESA Earthnet Online, E., 2013: ESA Website. Accessed: 2013-06-25, https://earth.esa.int/web/guest/missions/esa-future-missions/earthcare, accessed: 2013-06-25. 41

ESA Mission Experts Division, C.-o., P. Ingmann, 2004: Earthcare earth clouds, aerosols and radiation explorer, reports for mission selection. Tech. Rep. ESA SP-1279(1), European Space Agency, Nordwijk (NL). ISBN 92-9092-962-6. 9, 14

Forster, P. M. and K. P. Shine, 1999: Stratospheric water vapour changes as a possible contributor to observed stratospheric cooling. *Geophys. Res. Lett.*, **26**, 33093312. 16

Fournier, J. D., 1999: Reflectivity-rainfall rate relationships in operational meteorology. *NOAA*. 24

Frech, M., B. Lange, T. Mammen, J. Seltmann, C. Morehead, and J. Rowan, 2011: Onsite radome performance verification. *35st Conf. on Radar Meteorology, Pittsburgh, PA,*, A. M. Soc., Ed. xiv, 151

Fu, Q., S. K. Krueger, and K. N. Liou, 1995: Interactions of radiation and convection in simulated tropical cloud clusters. *J. Atmos. Sci*, **52**, 1310–1328. 58

Geleyn, J. F. and A. Hollingsworth, 1979: An economical method for the computation of the interaction between scattering and line absorption of radiation. *Contrib. Atmos. Phys.*, **52 (116)**. 13

Giangrande, S. E., S. Collis, J. Straka, A. Protat, C. Williams, and S. Krueger, 2013: A summary of convective-core vertical velocity properties using arm uhf wind profilers in oklahoma. *J. Appl. Meteor. Climatol.*, **52**. 2, 18

Goldhirsh, J. and B. Musiani, 1986a: Rain cell size statistics derived from radar observations at Wallops Is. Virginia. *IEEE Trans. on Geosci. Remote Sens.*, **GE-24 (6)**, 947–954. 77

Goldhirsh, J. and B. Musiani, 1986b: Rain cell size statistics derived from radar observations at wallops island, virginia. *IEEE Trans. Geosci. Remote Sens.*, **GE-24**, 947954. 48

Gregory, D. and P. R. Rowntree, 1990: A mass flux convection scheme with representation of cloud ensemble characteristics and stability dependent closure. *Mon. Weather Rev.*, **118 (1483-1506)**. 15

Heymsfield, G. M., L. Li, L. Tian, M. McGill, and Z. Wang, 2003: Thunderstorm generated cirrus observed from x and w-band airborne radar during crystal-face. *31st Conf. on Radar Meteorology, Seattle, WA,*, A. M. Soc., Ed. 60

Heymsfield, G. M., L. Tian, A. Heymsfield, L. Li, and S. Guimond, 2010: Characteristics of deep tropical and subtropical convection from nadir-viewing high-altitude airborne Doppler radar. *J. Atmos. Sci.*, **67**, 285–308. 8, 21, 49, 60, 173

Heymsfield, G. M., et al., 1996: The EDOP radar system on the high-altitude NASA ER-2 aircraft. *J. Atmos. Oceanic Technol.*, **13**, 795809. 62

Hildebrand, P. H. and R. S. Sekhon, 1974: Objective determination of the noise level in doppler spectra. *J. Appl. Meteorol.*, **13 (7)**, 808–811. 75

Hlire, A., A. Lefebvre, T. Wehr, J.-L. Bzy, and Y. Durand, 2007: The earthCARE mission: Mission concept and lidar instrument pre-development. *Geoscience and Remote Sensing Symposium, Barcelona*, IEEE, Ed., 4975 – 4978, iSBN 978-1-4244-1211-2. x, 41, 43

Hogan, R. J., 2008: Fast lidar and radar multiple-scattering models: Part I: Small-angle scattering using the photon variance-covariance method. *J. Atmos. Sci.*, **65**, 3621–3635, doi: 10.1175/2008JAS2643.1. 112

Hogan, R. J. and A. Battaglia, 2008: Fast lidar and radar multiple-scattering models: Part 2: Wide-angle scattering using the time-dependent two-stream approximation. *J. Atmos. Sci.*, **65**, 3636–3651, doi: 10.1175/2008JAS2643.1. 104

Houghton, J. T., L. G. M. Filho, B. A. Callander, N. Harris, A. Katenberg, and K. Maskell, 1995: *Climate Change 1995: The Science of Climate Change*. Cambridge University Press. 4

Hu, Y.-X., D. Winker, P. Yang, B. Baum, L. Poole, and L. Vann, 2001: Identification of cloud phase from PICASSO-CENA lidar depolarization: a multiple scattering sensitivity study. *J. Quant. Spectrosc. Radiat. Transfer*, **70 (4-6)**, 569–579. 149

Hubbert, J. and V. N. Bringi, 2000: The effects of three-body scattering on differential reflectivity signatures. *J. Atmos. Ocean Technol.*, **17**, 51–61. 111

IPCC, 2013: *Climate Change 2013: The Physical Science Basis. Contribution of Working Group I to the Fifth Assessment Report of the Intergovernmental Panel on Climate Change [Stocker, T.F., D. Qin, G.-K. Plattner, M. Tignor, S.K. Allen, J. Boschung, A. Nauels, Y. Xia, V. Bex and P.M. Midgley (eds.)]*. Cambridge University Press, Cambridge, United Kingdom and New York, NY, USA,, 1535 pp. 5

Jensen, E., D. Starr, and O. B. Toon, 2004: Mission investigates tropical cirrus clouds. *Eos, Trans. Amer. Geophys. Union*, **84 (5)**, 4550. 58

Joe, P., et al., 2010: The polar precipitation measurement mission. *Proc. 6th European Conference on Radar Meteorology and Hydrology: Satellite radar measurements and hydro-met eorological applications, Sibiu, Romania, 6-10 September, 2010*. 18

Joss, J. and R. Lee, 1995: The application of radar-gauge comparisons to operational precipitation profile corrections. *Journal of Applied Meteorology*, **34**, 2612–2630. 24

Kain, J. S., 2004: The kain-fritsch convective parameterization: An update. *J. Appl. Meteor.*, **43**, 170–181. 13, 14

Kain, J. S. and J. M. Fritsch, 1990: A one-dimensional entraining/detraining plume model and its application in convective parameterization. *J. Atmos. Sci.*, **47**, 2784–2802. 13

Kingsley, S. and S. Quegan, 1992: *Understanding Radar Systems*. McGraw-Hill Book Company. 84, 92

Kobayashi, S., H. Kumagai, and T. Iguchi, 2003: Accuracy evaluation of doppler velocity on a spaceborne weather radar through a random signal simulation. *J. Atmos. Oceanic Technol.*, **20**, 944949. 85

Kobayashi, S., H. Kumagai, and H. Kuroiwa, 2002: A Proposal of Pulse-Pair Doppler Operation on a Spaceborne Cloud-Profiling Radar in the W Band.

J. Atmos. Ocean Technol., **19**, 12941306, doi: http://dx.doi.org/10.1175/1520-0426(2002)019¡1294:APOPPD¿2.0.CO;2. xv, 21, 36, 37, 146, 150, 157, 158, 159

Kollias, P., 2010: Doppler effect modelling for Air Motion Estimates (DAME),atbd1. Tech. rep., McGill University Scientific Research, DEIMOS Space. 84, 97

Kollias, P., E. E. Clothiaux, M. A. Miller, B. A. Albrecht, G. L. Stephens, and T. P. Ackerman, 2007: Millimeter-wavelength radars: New frontier in atmospheric cloud and precipitation research. *Bull. Amer. Met. Soc.*, **88 (10)**, 1608–1624, doi: 10.1175/BAMS-88-10-1608. ix, 25, 26

Kollias, P., S. Tanelli, A. Battaglia, and A. Tatarevic, 2014: Evaluation of EarthCARE Cloud Profilling Radar Doppler Velocity Measurements in Particle Sedimentaion Regimes. *J. Atmos. Ocean Technol.*, **31 (366386)**. 108, 109, 174

Kuang, Z. and C. S. Bretherton, 2004: Convective influence on the heat balance of the tropical tropopause layer: A cloud-resolving model study. *J. Atmos. Sci.*, **61 (23)**, 2919–2927, doi: 10.1175/JAS-3306.1. 7

Kulie, M. S., R. Bennartz, T. J. Greenwald, Y. Chen, and F. Weng, 2010: Uncertainties in microwave properties of frozen precipitation: Implications for remote sensing and data assimilation. *J. Atmos. Sci.*, **67 (11)**, 3471–3487, doi: 10.1175/2010JAS3520.1. 116

Kummerow, C. D., W. Barnes, T. Kozu, J. Shiue, and J. Simpson, 1998: The

tropical rainfall measuring mission (TRMM) sensor package. *J. Atmos. Ocean Technol.*, 809–817. 2

Lange, S., B. Rockel, J. Volkholz, and B. Bookhagen, 2014: Regional climate model sensitivities to parametrizations of convection and non-precipitating subgrid-scale clouds over South America. *Clim. Dyn.*, **44 (2839-2857)**. 15

Lhermitte, R., 1990: Attenuation and scattering of millimeter wavelength radiation by clouds and precipitation. *J. Atmos. Ocean Technol.*, **7**, 464–479. 25

Li, L., G. M. Heymsfield, P. E. Racette, L. Tian, and E. Zenker, 2004: A 94-GHz Cloud Radar System on a NASA High-Altitude ER-2 Aircraft. *JAOT*, **21 (9)**, 1378–1388. 62

Liu, C. L. and A. J. Illingworth, 2000: Toward more accurate retrievals of ice water content from radar measurements of clouds. *J. Appl. Meteorol.*, **39 (11301146)**. 13

Marzano, F. S., L. Roberti, S. Di Michele, A. Mugnai, and A. Tassa, 2003: Modeling of apparent radar reflectivity due to convective clouds at attenuating wavelenghts. *Radio Sci.*, **38(1), 1002**, doi: 10.1029/2002RS002 613. 111

Meneguz, E. and D. J. Thomson, 2013: Improved scheme for parametrization of convective transport in NAME III. *Proceedings of the* 15^{th} *Conference on Harmonisation within Atmospheric Dispersion Moelling for Regulatory Purposes, 2013, Madrid, Spain.* 14

Miller, K. S. and M. M. Rochwarger, 1972: A covariance approach to spectral moment estimation. *IEEE Trans. Inf. Theory*, **18**, 588597. 39

Moran, K. P., B. E. Martner, M. J. Post, R. A. Kropfli, D. C. Welsh, and K. B. Widener, 1998: An unattended cloud-profiling radar for use in climate research. *Bull. Amer. Met. Soc.*, **79**, 443 455. 25

Morcrette, J. J. and Y. Fourquart, 1986: The overlapping of cloud layers in shortwave radiation parameterizations. *J. Atmos. Sci.*, **43 (321328)**. 13

Narita, M. and S. Ohmori, 2007: Improving precipitation forecasts by the operational nonhydrostatic mesoscale model with the kain-fritsch convective parameterization and cloud microphysics. *Proceedings of the* 12^{th} *Conference Mesoscale Processes, 2007, Waterville Valley, NH, Amer. Meteor. Soc., 37.* 15

Nesbitt S., W. and E. J. Zipser, 2003: The diurnal cycle of rainfall and convective intensity according to three years of trmm measurements. *J. Climate*, **16**, 14561475. 18

North, G., J. Pyle, and F. Zhang, 2015: *Encyclopedia of Atmospheric Sciences*. 2d ed., Academic Press, imprint of Elsevier, London. xii, 98

Parodi, A. and S. Tanelli, 2010: Influence of turbulence parameterizations on high-resolution numerical modeling of tropical convection observed during the tc4 field campaign. *J. Geophys. Res.*, **115 (D00J14)**, doi:10.1029/2009JD013302. 77

Pazmany, A., J. Galloway, J. Mead, I. Popstefanija, R. McIntosh, and H. Bluestein, 1999: Polarization Diversity Pulse-Pair Technique for Millimetre-Wave Doppler Radar Measurements of Severe Storm Features. *JAOT*, **16**, 1900–1910. xiv, 21, 146, 152, 153, 155, 156, 159

Phillips, V. T. J. and L. J. Donner, 2006: Cloud microphysics, radiation and vertical velocities in two- and three-dimensional simulations of deep convection. *Quart. J. Roy. Meteor. Soc.*, 3011–3033. 1

Rickenbach, T., P. Kucera, M. Gentry, L. Carey, A. Lare, R.-F. Lin, B. Demoz, and D. O. Starr, 2008: The Relationship between Anvil Clouds and Convective Cells: A Case Study in South Florida during CRYSTAL-FACE. *Mon. Wea. Rev.*, **136**, 39173932. 58, 65

Rinehart, R. E., 2004: *Radar for Meteorologists*. 4th ed., Rinehart Publishing, Columbia. 23, 32

Sassen, K., 1987: Ice cloud content from radar reflectivity. *J. Climate Appl. Meteorol.*, **26 (10501053)**. 13

Schutgens, N. A. J., 2008: Simulated Doppler Radar Observations of Inhomogeneous Clouds: Application to the EarthCARE Space Mission. *J. Atmos. Oceanic Technol.*, **25 (9)**, 1514–1528, doi: 10.1175/2007JTECHA1026.1. 21, 36, 80, 126

Sekelsky, S. M. and R. E. McIntosh, 1996: Cloud observations with polarimetrc 33 GHz and 95 GHz radar. *Meteor. Atmos. Phys.*, **59**, 123140. 62

Sherwood, S. and A. E. Dessler, 2001: A model for transport across the tropical tropopause. *J. Atmos. Sci.*, **58**, 765779, doi:10.1175/1520-0469(2001)058¡0765:AMFTAT¿2.0.CO;2. 16, 17

Sirmans, D. and B. Bumgarner, 1975: Numerical comparison of five mean frequency estimators. *J. Appl. Meteorol.*, **14 (6)**, 991–1003, doi: 10.1175/1520-0450. 75, 97

Skamarock, W. C., J. B. Klemp, J. Dudhia, D. O. Gill, D. M. Barker, W. Wang, and J. G. Powers, 2005: A Description of the Advanced Research WRF Version 2. Tech. rep., NCAR Tech Note. 88 pp. 77

Skolnik, M. I., 2001: *Introduction to Radar Systems*. McGraw-Hill, 3-rd ed., New York. ix, 29, 33

Smith, C. A., J. D. Haigh, and R. Toumi, 2001: Radiative forcing due to trends in stratospheric water vapour. *Geophys. Res. Lett.*, **28**, 179182. 16

Smith, R. N. B., 1990: A scheme for predicting layer clouds and their water content in a general circulation model. *Q. J. R. Meteorol. Soc.*, **116 (435460)**. 11

Sohn, B.-J. and J. Schmetz, 2004: Water VaporInduced OLR Variations Associated with High Cloud Changes over the Tropics: A Study from Meteosat-5 Observations. *J. Clim.*, **17 (10)**, 1987–1996, doi: 10.1175/1520-0442. 8

Stensrud, D., 2012: An Overview of Convection Parameterization. *13th Annual*

WRF Users' Workshop, Boulder, Colorado, USA, N. Oceanic and A. Administration, Eds. 7

Stephens, G. L., S. C. Tsay, P. W. Stackhouse, and P. J. Flatau, 1990: The relevance of the microphysical and radiative properties of cirrus clouds to climate and climate feedback. *J. Atmos. Sci*, **47**, 1742–1752. 4

Stephens, G. L. and N. B. Wood, 2007: Properties of tropical convection observed by millimeter-wave radar systems. *Month. Weath. Rev.*, **135 (3)**, 821–842, doi: 10.1175/MWR3321.1. 1, 26, 59

Stephens, G. L., et al., 2002: The CloudSat mission and the A-train. *Bull. Amer. Met. Soc.*, **83 (12)**, 1771–1790. 2, 25

Sy, O. O., S. Tanelli, N. Takahashi, Y. Ohno, H. Horie, and P. Kollias, 2013: Simulation of EarthCARE Spaceborne Doppler Radar Products Using Ground-Based and Airborne Data: Effects of Aliasing and Nonuniform Beam-Filling. *Geoscience and Remote Sensing, IEEE Transactions on*, **PP (99)**. 21, 68, 126, 127, 131, 175

Tanelli, S., G. M. Heymsfield, G. S. Stephens, S. L. Durden, E. Im, P. Racette, L. Li, and G. Sadowy, 2010: NASA ACE (Aerosol-Cloud-Ecosystem). Tech. rep., NASA. Http://dsm.gsfc.nasa.gov/ace/documents.html). 18

Tanelli, S., E. Im, S. Durden, D. Giuli, and L. Facheris, 2008: Spaceborne Doppler radars for atmospheric dynamics and energy budget studies. *Proceedings of IEEE Radar Conf.*, 1–6, May 26-30, 2008, Rome, Italy. 108

Tanelli, S., E. Im, S. L. Durden, L. Facheris, and D. Giuli, 2002a: The effects of nonuniform beam filling on vertical rainfall velocity measurements with a spaceborne Doppler radar. *J. Atmos. Oceanic Technol.*, **19 (7)**, 1019–1034, doi: 10.1175/1520-0426(2002)019. 21, 38, 80, 126

Tanelli, S., E. Im, S. L. Durden, L. Facheris, D. Giuli, and E. Smith, 2004: Rainfall Doppler velocity measurements from spaceborne radar: overcoming nonuniform beam filling effects. *J. Atmos. Oceanic Technol.*, **21 (1)**, 27–44, doi: 10.1175/1520-0426. 123, 126

Tanelli, S., E. Im, Facheris, and E. A. Smith, 2002b: DFT-based spectral moments estimators for spaceborne Doppler precipitation radars. *Proceedings of SPIE*, **4894 (50)**. 75

Tanelli, S., E. Im, S. R. Mascelloni, and L. Facheris, 2005: Spaceborne Doppler radar measurements of rainfall: correction of errors induced by pointing uncertainties. *J. Atmos. Oceanic Technol.*, **22 (11)**, 1676–1690, doi: 10.1175/JTECH1797.1. 21, 140

Tian, B. and V. Ramanathan, 2002: Role of tropical clouds in surface and atmospheric energy budget. *J. Clim.*, **15 (3)**, 296–305, doi: 10.1175/1520-0442. 7

Wilson, D. R. and S. P. Ballard, 1999: A microphysically based precipitation scheme for the UK Meteorological Office Unified Model. *Q. J. R. Meteorol. Soc.*, **125 (16071636)**. 12

Zhang, C., 1993: Large-Scale Variability of Atmospheric Deep Convection in Relation to Sea Surface Temperature in the Tropics. *J. Climate*, **6**, 18981913. 7

Zipser, E. J., D. J. Cecil, C. Liu, S. W. Nesbitt, and D. P. Yorty, 2006: Where are the most intense thunderstorms on Earth? *Bull. Amer. Meteor. Soc.*, **87**, 10571071. 7, 49

Zrnic, D., R. Doviak, G. Zhang, and A. Ryzhkov, 2010: Bias in differential reflectivity bias due to cross coupling through the radiation patterns of polarimetric weather radars. *J. Atmos. Ocean. Tech.*, **27**, 16241637. 151

Zrnic', D. S., 1975: Simulation of weatherlike doppler spectra and signals. *Journal of Applied Meteorology*, **14 (4)**, 619–620. 35, 75, 88, 89, 92, 151

Zrnic, D. S., 1977: Spectral moment estimates from correlated pulse pairs. *IEEE Trans. Aerosp. Electron. Syst.*, **AES-13**, 344354. 84, 97, 109, 160

Zrnic', D. S., 1979: Estimation of spectral moments for weather echoes. *IEEE Trans. On Geosc. Electr.*, **14 (4)**, 113–128. 84, 97